

Unterschrift des Betreuers



TECHNISCHE  
UNIVERSITÄT  
WIEN

Vienna University of Technology

## D I P L O M A R B E I T

# Mass movement modelling over Ciloto area based on integrated GNSS and TLS observations

Ausgeführt am

Department für Geodäsie und Geoinformation  
Forschungsgruppe Ingenieurgeodäsie  
der Technischen Universität Wien

unter der Anleitung von

A.o. Univ.Prof. Dipl.-Ing. Dr.techn. Robert Weber  
Univ.Ass. Dipl.-Ing. Dr.techn. Miriam Zamecnikova

durch

Martin Schuler, BSc  
MatrNr.: 0825990  
Quadratsch 30  
6551 Pians - Austria



Master thesis

# Mass movement modelling over Ciloto area based on integrated GNSS and TLS observations

performed at the  
*Department of Geodesy and Geoinformation* at the TU Vienna - Austria

supervised by  
A.o. Univ.Prof. Dipl.-Ing. Dr.techn. Robert Weber  
assisted by  
Univ.Ass. Dipl.-Ing. Dr.techn. Miriam Zamecnikova

in cooperation with the  
*Faculty of Earth Science and Technology* at the IT Bandung - Indonesia

externally supervised by  
Dr. Ir. Vera Sadarviana and Dr. Dudy Wijaya

realised by  
Martin Schuler, BSc  
MatrNr.: 0825990  
Quadratsch 30  
6551 Pians - Austria

Vienna, March 2015



## Abstract

The objective of this master thesis is the evaluation and modelling of a mass movement which occurs at the landslide area in Ciloto (West Java - Indonesia). The movement is mainly triggered by accumulated water from surrounding areas and moving in a south-easterly direction. The strong vegetated landslide zone, which includes rotational, translational and compounded slides, is located between the volcano Gunung Gede and the mountain Gunung Lemo.

For decades this sliding area serves as a residential zone, agricultural land as well as an important infrastructural region for the inhabitants of West Java. Detailed knowledge of the mass movement can help scientists in counselling government officials to provide effective prevention policies and support for inhabitants at risk.

Previous measurements by means of Global Positioning System (GPS) and Total Positioning Stations (total station - TPS) indicated regionally and sectorally different motions within the landslide. Based on these results the measurement campaign for this research was planned along an assumed border between a rotational and a translational movement. Within three observation periods the viewpoints are monitored by GPS and Terrestrial Laser Scanning (TLS). Statistical methods are used to obtain a precise estimation of the accuracy of the measurements. To ensure an exact linkage between the GPS and TLS scans a bundle block adjustment was carried out. Furthermore, by means of the covariance error propagation law, the accuracies of the measured, the registered as well as the georeferenced points plus the GPS accuracy, are taken into account to estimate the overall accuracy. Finally, the t-Student distribution was used to evaluate the significant displacements of observation points. For the analysis the TLS results are split in horizontal ( $X$  and  $Y$ ) and vertical ( $Z$ ) movements.

## Kurzfassung

Das Rutschgebiet in Ciloto liegt unterhalb der alten Hauptstraße zwischen Jakarta und Bandung (West Java - Indonesia). In der Schneise zwischen dem Vulkan Gunung Gede und dem Berg Gunung Lemo bewegt sich der von stark bewachsener Vegetation geprägte Hangrutsch in süd-östliche Richtung. Wasser, das sich aus den umgebenden Gebieten ansammelt, gilt als großer Einflussfaktor und Auslöser dieser Massenbewegung.

Das als 'sehr langsam' klassifizierte Rutschungsgebiet ist bewohnt, wird landwirtschaftlich genutzt und stellt seit Jahrzehnten eine Gefahr für Mensch und Infrastruktur dar. Detaillierte Kenntnis der Massenbewegung würde der Wissenschaft und auch der Regierung helfen, präventive Schutzmaßnahmen zu erarbeiten.

Vorausgegangene Messkampagnen mittels Globalem Positionierungs System (GPS) und terrestrischen Messungen (Totalstation - TPS) zeigten sektoriell unterschiedliche Bewegungsabläufe inmitten der Massenbewegung. Entlang einer vermuteten Grenze zwischen einer rotationalen und translationalen Bewegung wurde die Messkampagne für diese Ausarbeitung geplant. Zehn Standpunkte wurden mittels GPS und Terrestrischem Laser Scanner (TLS) in drei Messperioden beobachtet. Die Ausarbeitung des statischen Modells stimmte mit den Ergebnissen aus den vorausgegangenen Messkampagnen überein. Die GPS-Messungen waren auch für die Georeferenzierung der TLS-Messungen erforderlich. Die Verknüpfung der Einzelscans wurden mit der Bündelblockausgleichung umgesetzt. Unter der Annahme, dass ein Beobachtungspunkt fehlerfrei beobachtet worden ist, wurden mit dem Fehlerfortpflanzungsgesetz die Genauigkeiten der Verknüpfungspunkte und der anderen Standpunkte berechnet. Die Schätzung der Gesamtgenauigkeit beinhaltet die Genauigkeiten der gemessenen Einzelscans, der Registrierung der Scans und der Georeferenzierung samt GPS-Messgenauigkeiten. Die Signifikanz der Verschiebungen wurden mit der t-Student Verteilung untersucht. Die Ausarbeitung der TLS-Messungen wurden in horizontale ( $X$  und  $Y$ ) und vertikale ( $Z$ ) Verschiebungen aufgeteilt.



## Acknowledgement

On this page I want to extend my thanks to all the people who supported and helped me during my study at Vienna University of Technology and especially during the term abroad in Indonesia.

A.o. Univ.Prof. Dipl.-Ing. Dr.techn. Robert Weber supervised me through the complete thesis. He indicated the direction I should follow for this work, and gave me important hints about the content of my writing. He supported me in the aspect relating to the GPS measurements and examined the whole thesis.

Univ.Ass. Dipl.-Ing. Dr.techn. Miriam Zamecnikova supported me in Vienna in all questions about TLS. She gave me important hints for the elaboration of this thesis.

Univ.Prof. Dipl.-Ing. Dr.techn. Harald Schuh enabled me the possibility of the term abroad by his contacts to Dr. Dudy Wijaya at ITB.

Dr. Ir. Vera Sadarviana and Dr. Dudy Wijaya organised the project for me. They supervised and supported me in all necessary parts during my stay in Indonesia.

Thanks a lot to students and friends at ITB for the good collaboration and at Vienna University of Technology for the proofreading of this thesis.

At last, many thanks to my family and friends in Austria and Indonesia which supported me in good as well as in bad times during my study. They gave me all necessary power I needed, especially in bad times.





# Contents

<b>Abstract</b>	<b>III</b>
<b>Kurzfassung</b>	<b>III</b>
<b>Acknowledgement</b>	<b>V</b>
<b>List of Figures</b>	<b>X</b>
<b>List of Tables</b>	<b>X</b>
<b>List of Abbreviations</b>	<b>X</b>
<b>1 Introduction</b>	<b>1</b>
1.1 Motivation . . . . .	1
1.2 Research aims and purposes . . . . .	1
1.3 Structure of the thesis . . . . .	2
<b>2 Fundamental theory</b>	<b>3</b>
2.1 Review of physical and mathematical concepts of mass movements . . . . .	3
2.1.1 Physical fundamentals of denudative movements . . . . .	3
2.1.2 Reasons for mass movements . . . . .	4
2.1.3 Classification of mass movements . . . . .	5
2.2 Review of geological settings of the Ciloto area . . . . .	8
2.2.1 Morphology around Ciloto area . . . . .	8
2.2.2 Geological structure of Ciloto area . . . . .	9
2.3 Review of mass movement phenomena over Ciloto area . . . . .	12
2.3.1 Modelling of Ciloto area . . . . .	13
2.3.2 Results . . . . .	13
2.4 Basic principles of GNSS and TLS . . . . .	16
2.4.1 Global Navigation Satellite Systems (GNSS) . . . . .	16
2.4.2 Terrestrial Laser Scanning (TLS) . . . . .	20
2.5 Coordinate systems . . . . .	26
2.5.1 Earth-Centered, Earth-Fixed (ECEF) . . . . .	26
2.5.2 UTM-coordinates . . . . .	27
2.6 Monitoring . . . . .	27
2.6.1 Monitoring and modelling methods of mass movements . . . . .	28
2.6.2 Geodetic methods for mass movement monitoring . . . . .	30
2.6.3 Statistical significance test . . . . .	31
<b>3 GNSS and TLS observation and data processing</b>	<b>33</b>
3.1 Description of GNSS and TLS campaigns . . . . .	33
3.1.1 Measured points . . . . .	34
3.1.2 Measurement devices . . . . .	36
3.1.3 Measurements . . . . .	38
3.2 Data processing . . . . .	38
3.2.1 Data processing of GPS by Bernese . . . . .	39
3.2.2 Data processing of TLS by Cyclone and CloudCompare (CC) . . . . .	42
3.3 Results of data processing . . . . .	50
3.3.1 GPS results . . . . .	50
3.3.2 TLS results . . . . .	52
3.3.3 Overall accuracy of the measurements . . . . .	55

<b>4</b>	<b>Mass movement modelling</b>	<b>58</b>
4.1	Determination and validation of the static model . . . . .	58
4.2	Analysis of the results concerning TLS . . . . .	62
4.2.1	Accuracy of the results . . . . .	69
4.2.2	Meteorological effects . . . . .	69
4.2.3	Geophysical effects . . . . .	71
<b>5</b>	<b>Discussion and summary</b>	<b>72</b>
5.1	Discussion . . . . .	72
5.2	Future improvements . . . . .	73
5.2.1	GPS-measurements . . . . .	73
5.2.2	TLS-measurements . . . . .	73
5.3	Summary . . . . .	74
	<b>References</b>	<b>77</b>

## List of Figures

1	Gravity acceleration in a slope . . . . .	3
2	Angle of repose . . . . .	4
3	Processes and forms of mass movements . . . . .	5
4	Rotational movement . . . . .	6
5	Area prone of rock fall . . . . .	7
6	Influenced areas around Ciloto-Puncak . . . . .	8
7	Slope situation and Cijember river valley . . . . .	9
8	Cijember river valley . . . . .	9
9	Fish ponds . . . . .	10
10	Geology map of the mass movement . . . . .	10
11	Cracks in the sliding area . . . . .	10
12	Drilling logs . . . . .	11
13	Terrestrial measurements . . . . .	12
14	GPS measurements . . . . .	14
15	Positioning process of GNSS . . . . .	18
16	Improvement of the pseudo range . . . . .	19
17	Single differences, double differences and triple differences . . . . .	20
18	Range, vertical and horizontal rotations of panorama scanner . . . . .	20
19	Classification of TLS . . . . .	21
20	Principle of camera scanner . . . . .	22
21	Principle of hybrid scanner . . . . .	22
22	Georeferencing . . . . .	23
23	Geocentric coordinate system . . . . .	27
24	Monitoring methods . . . . .	28
25	Criteria of ground movements . . . . .	30
26	Observation points of the slope . . . . .	33
27	Part 1 of the observation points . . . . .	34
28	Part 2 of the observation points . . . . .	35
29	Topcon GR-3 . . . . .	36
30	Leica ScanStation C10 . . . . .	37
31	Reflectors . . . . .	38
32	Coordinate file . . . . .	39
33	Abbreviation file . . . . .	40
34	Station file . . . . .	41
35	GPS data processing of BASE station . . . . .	41
36	Targets of the TLS clouds . . . . .	43
37	Accuracy of the horizontal position of period 2 . . . . .	45
38	Accuracy of the vertical position of period 2 . . . . .	45
39	Vegetation by CT04 in south-west direction . . . . .	46
40	Different smooth factors situation 1 . . . . .	49
41	Different smooth factors situation 2 . . . . .	50
42	Horizontal misclosures between the GPS and TPS viewpoints . . . . .	54
43	Comparison of the displacements in vertical direction [m] . . . . .	55
44	Point accuracy of the single scan measurements in directions $X$ and $Y$ . . . . .	56
45	3D point position error of the single scan measurements . . . . .	56
46	3D point accuracy of the TLS results . . . . .	56
47	3D point accuracy of the whole measurements . . . . .	57
48	Absolute vertical movements of the GPS viewpoints . . . . .	59
49	Absolute horizontal movements of the GPS viewpoints . . . . .	60

50	Absolute horizontal movements of the TLS viewpoints . . . . .	60
51	Comparison of the displacements [m] in horizontal and vertical direction . . . . .	63
52	Displacements zone 1 . . . . .	64
53	Displacements zone 2 . . . . .	65
54	Displacements zone 3 . . . . .	66
55	Displacements zone 4 . . . . .	67
56	Displacements zone 5 . . . . .	68
57	Precipitation in the years 2010 to 2014 . . . . .	70
58	Precipitation in the measurement area . . . . .	70

## List of Tables

1	GNSS differences . . . . .	17
2	Application fields of TLS . . . . .	23
3	Construction of the design matrix A . . . . .	25
4	Classification of deformation models . . . . .	29
5	IGS stations . . . . .	40
6	Accuracies of the viewpoints and targets after the nexus of period 2 . . . . .	44
7	Viewpoints and their measured target marks for all periods . . . . .	44
8	Roughly georeferenced TLS coordinates . . . . .	46
9	Used tie points for the georeferencing . . . . .	47
10	Estimation of the parameters for the georeferencing and their accuracy . . . . .	48
11	Matrices composed of rotation matrix and translation vector . . . . .	48
12	Displacement of the BASE station between the measurement periods . . . . .	51
13	Estimated absolute GPS coordinates from measurement campaign . . . . .	52
14	Transformed and absolute TLS coordinates . . . . .	53
15	Misclosures between the GPS and TLS coordinates . . . . .	53
16	Displacements of GPS measurements between the periods and their significance . . . . .	59
17	Absolute movements of the GPS viewpoints . . . . .	61
18	Absolute movements of the TLS viewpoints . . . . .	61

## List of Abbreviations

### general:

BSc	Bachelor of Science
cm	centimetre
e.g.	exempli gratia
Fig.	Figure
GB	Giga Byte
h	hour
ha	hectare
IT	Institut Teknologi
kg	kilogram
km	kilometre
m	metre
mm	millimetre
MatrNr.	Matriculation Number
min	minute
no.	number

p.	page
ppm	parts per million
s	second
SSD	Solid-State-Drive
Tab.	Table
TU	Technical University
UCSD	University of California - San Diego
USB	Universal Serial Bus
vs.	versus

**technical:**

AIUB	Astronomical Institute of the University of Bern
BDS	BeiDou Navigation Satellite System
C/A-code	Coarse/Acquisition code
CC	CloudCompare
DD	Double Difference
DGPS	Differential Global Positioning System
ECEF	Earth-Centered, Earth-Fixed
EDM	Electronic Distance Measurement
EGNOS	European Geostationary Navigation Overlay Service
FoV	Field of View
GLONASS	GLOBAL NAVIGATION Satellite System
GNSS	Global Navigation Satellite Systems
GPS	Global Positioning System
GWL	Ground Water Level
IGS	International GNSS Service
ICP	Iterative Closest Point
IP	Dynamic Internet Protocol
ITB	Institut Teknologi Bandung
IMU	Inertial Measurement Unit
IRM	International Reference Meridian
IRP	International Reference Pole
ITRF08	International Terrestrial Reference Frame 2008
NS	Navigation Satellite
P(Y)-code	Precise code
PPP	Precise Point Positioning
RTK	Real Time Kinematic
QIF	Quasi-Ionosphere-Free
RINEX	Receiver Independent Exchange Format
SD	Single Difference
SNR	Signal Noise Ratio
TD	Triple Difference
TLS	Terrestrial Laser Scanning
TPS	Total Positioning Station
UTM	Universal Transverse Mercator
WAAS	Wide Area Augmentation System
WGS84	World Geodetic System 1984



# 1 Introduction

A complex mass movement of about 40ha in the south of Bogor (West Java - Indonesia) endangered the infrastructure and human life. To get an idea of the properties of the whole landslide, different measurement campaigns were performed. Due to results of previous measurements this research covers only a part of the landslide. This activity has been elaborated by *Global Navigation Satellite Systems (GNSS)* and *Terrestrial Laser Scanning (TLS)* measurements.

## 1.1 Motivation

The area of Ciloto is situated in the south of the Indonesian city Bogor, which is located at the old main road between Jakarta and Bandung (West Java). On a sea level of 1330m the Ciloto area is located between the volcano *Gunung Gede* and the mountain *Gunung Lemo*. Based on the morphology water accumulates between the levies and the only way to flow off is through the area of Ciloto (see section 2.2.1).

First evaluations of the sliding area were done in the years of 1986 to 2001. The *Faculty of Earth Science and Technology* at the *Institut Teknologi Bandung (ITB)* took some measurement campaigns by terrestrial observations (total station). They detected that different sliding behaviours affect the whole movement area. Evaluations about the geomorphology from the area in and around Ciloto allow the first insights about the sliding behaviour. Water is an important factor together with the increasing traffic on the road which influence the behaviour strongly. The road proceeds on the side and at the top of the sliding area.

The second evaluation was carried out by *Global Positioning System (GPS)* measurements in 2002 to 2005. Based on several measurement campaigns different models were created and a complex movement behaviour of the landslide was discernible. The whole area shows different sliding behaviours - rotational, translational and compound - which can happen independently. All in all, the west side of the movement includes mostly rotational displacements whereas the east side includes predominantly translational movement.

Terrestrial measurements and GPS measurements represent only selective points. The technical progress and the development of TLS allow further monitoring of the part around the observation points. This opens the possibility of detailed surface measurements. Point clouds represent the surface of the measurement object and a comparison of two or more scans at the same measurement points show differences between the periods.

## 1.2 Research aims and purposes

For this research a part of the whole sliding area is chosen. The measurement area is located in the northern part along a supposed border between different sliding behaviours, where on the west side rotational sliding and on the east side translational movement predominate. In this part ten viewpoints are observed by GPS and TLS. The observation points are chosen so as to meet the requirements of the TLS measurements. For the nexus of single scans 2D reflector marks are applied. The movement behaviours of the GPS measurements are used for the comparison with the previous campaign of 2002 to 2005 and for the georeferencing of the point clouds. Based on the GPS results a statistic as well as a kinematic model should be created and analysed. By comparison of the point clouds from the TLS measurements the behaviour of the displacement should be discussed. It should be answered whether cracks and movement directions of individual parts on the surface are visible. An analysis about

the accuracy should be helpful for the significance of displacements. If possible, a comparison between a similar movement in Austria and the movement area in Ciloto should be carried out.

### 1.3 Structure of the thesis

In this thesis the work with a TLS device in Indonesia is described. The chapters give information about the basics, the workings, the results and the conclusions. Finally a discussion is provided.

The second chapter is divided into two parts. The first part gives general information about the physical and mathematical concept concerning mass movements. The morphology and the geological settings of the area in Ciloto are discussed. An overview about previous measurement campaigns and their results is given. The second part informs about the basics of the measurement devices which are used for the practical work for this research. Different coordinate systems which are applied for the measurement procedures are explained. At the end of the chapter all possible monitoring systems for mass movements are listed and the basics of the statistical significance test is explained.

In chapter three the measurement campaigns and the data processing are described. All problems which occur during the measurements and the data processing are quoted in detail. It is explained which steps are done with which program and which attitudes are used. At last the results are listed. The accuracy analysis yielded the precision of the results.

Elaborations and analyses fill chapter four. The focus of the analyses are set by the TLS results with comparisons to the GPS solutions. Finally, equality and differences to previous measurement campaigns are explained.

The fifth chapter contains the discussion of this research. Advantages and disadvantages about the execution of the measurement campaign and also future improvement suggestions are listed. The summary at the end completes this thesis.



## 2 Fundamental theory

### 2.1 Review of physical and mathematical concepts of mass movements

Mass movements occur naturally and are based on geomorphological processes. This kind of geological danger is a natural consequence of changes concerning the topography, seismicity, stress changes, loss of strength, groundwater flows and process of weathering. Mass movements emboss the mountainous landscape mainly in up- and highlands [Bayerisches Landesamt für Umwelt, 2013, "Massenbewegungen", retrieved: 27.10.2013]; [Abramson et al., 1996, p. 3].

#### 2.1.1 Physical fundamentals of denudative movements

The kinetic energy  $E_k$  (2.1) is defined as the energy with respect to moving systems. The potential energy  $E_p$  (2.1) describes the energy of a physical system, which depends on the position and the gravity acceleration [Freie Universität Berlin, 2013, "Physikalische Grundlagen", retrieved: 29.10.2013].

$$E_k = \frac{m * v^2}{2} \qquad E_p = m * g * h \qquad (2.1)$$

with  $m$  = mass [kg],  $v$  = velocity [ $\frac{m}{s}$ ],  $g$  = gravity acceleration ( $= 9.81[\frac{m}{s^2}]$ ) and  $h$  = height [m].

The potential energy  $E_p$  (2.1) of a mass movement can be calculated before and after a motion. The difference of these two energies is the work, which is essential for the mass movement. The gravity force  $G$  (2.2) is orientated to the center of the earth.

$$G = m * g \qquad (2.2)$$

The effect of the gravity on the mass movement in a slope is a function of the hillslope  $\alpha$ . Visually the mass movement is orientated parallel to the hillslope. For that reason it is possible to split the vector  $E_p$  (2.1) into two vectors  $\sigma$  and  $\tau$  (see Fig. 1 and (2.3)) [Freie Universität Berlin, 2013, "Schwerebeschleunigung am Hang", retrieved: 29.10.2013].

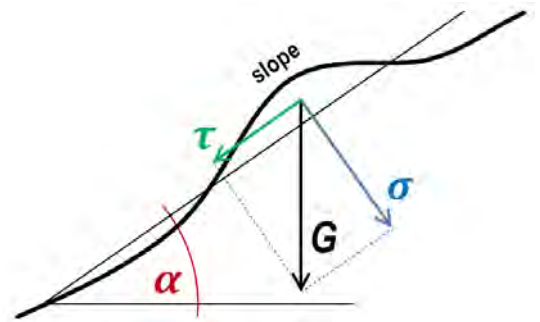


Figure 1: Gravity acceleration in a slope with  $\alpha$  = hillslope [ $^\circ$ ],  $\sigma$  = normal force [N],  $\tau$  = tensile force [N] and  $G$  = gravity force [N].

For that reason it is possible to split the vector  $E_p$  (2.1) into two vectors  $\sigma$  and  $\tau$  (see Fig. 1 and (2.3)) [Freie Universität Berlin, 2013, "Schwerebeschleunigung am Hang", retrieved: 29.10.2013].

$$\tau = G * \sin \alpha \qquad \sigma = G * \cos \alpha \qquad (2.3)$$

with  $\tau$  = shear stress [ $\frac{N}{m^2}$ ] and  $\sigma$  = compressive stress [ $\frac{N}{m^2}$ ]

From the equations in (2.3) it follows that the shear force and the normal force are given with  $K_S[N]$  and  $K_N[N]$ .

$$K_S = m * \tau = m * G * \sin \alpha \qquad K_N = m * \sigma = m * G * \cos \alpha \qquad (2.4)$$

When the shear stress  $\tau$  exceeds a boundary value  $s$  a mass movement will start. This value  $s$  is called *cross shear stress* which is described by two factors, the gravity acceleration  $g = 9.81 \frac{\text{m}}{\text{s}^2}$  and the inner friction. The inner friction depends on different factors:

- Cohesion
- Grain shape
- Kind of stratification (consolidated or unconsolidated)
- Mix of different grain sizes
- Hillslope  $\alpha$

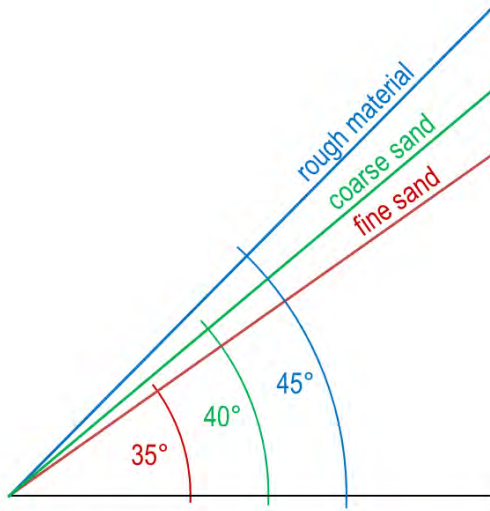


Figure 2: Angle of repose

The friction angle  $\phi$  or natural angle of repose (see Fig. 2) is defined as the angle, in which coherent material begins to move. The cross shear stress  $s$  is exceeded when the shear stress  $\tau$  is bigger than the inner friction. Fine sand can be regarded as rounded grains which are unconsolidated and not mixed with other grain sizes. The boundary value  $s$  for mass movements of fine sand is given by  $\phi = 35^\circ$ . Rough material, which is a consolidated mixture of grains different sizes, the value  $s$  is given by  $\phi = 45^\circ$  (see Fig. 2) [Freie Universität Berlin, 2013, "Grenzscherbspannung", retrieved: 01.11.2013].

In this case the cross shear stress  $s$  and the compressive stress  $\sigma$  for non-coherent materials are defined in equations (2.5).

$$s = g * \sin \phi \qquad \sigma = g * \cos \phi \qquad (2.5)$$

Water produces a kind of bond between the grains which is called cohesion. In the case of coherent materials a correction factor  $c$  will be included. From  $\frac{s}{\sigma} = \frac{g * \sin \phi}{g * \cos \phi} = \tan \phi$  (2.5) Coulomb's<sup>1</sup> law (2.6) follows [Freie Universität Berlin, 2013, "Coulombsches Gesetz", retrieved: 29.10.2013].

$$s = \sigma * \tan \phi + c \qquad (2.6)$$

### 2.1.2 Reasons for mass movements

The most common actuator of mass movements is water. Areas surrounding rivers, groundwater, heavy rainfalls and snow melt are kinds of actuators. In the case of heavy rainfalls or snow melt the absorption of water in latent soil is high. A high water content is the reason for a weaker friction force. Thus, the gravity is stronger than the friction force and pulls the mass downwards. In this case the mass movements are produced by gravity and are called gravity mass movements [Universität Freiburg, 2013, "Gravitative Massenbewegungen", retrieved: 27.10.2013]. In the following, other triggers for gravity mass movements are listed:

- Erosion by wind and frost.
- Land management.
- Deforestation (roots, which stabilise the soil, will die).
- Thawing of permafrost.

<sup>1</sup>Charles Augustin de Coulomb (\*1736 - †1806), French physicist

Not every mass movement depends on gravity. The second group of mass movements are tectonic mass movements which depends on two factors:

- Earthquakes
- Tectonic movements

This two types of mass movements also depend on physical factors:

- Water permeability of the soil.
- Water absorption of the soil.
- Slope of the surface.
- Structure of the soil building and their boundary (clay soil).

### 2.1.3 Classification of mass movements

Mass movements can be distinguished by a lot of factors, like the type of material, movement and the velocity of the motion [PAUX Technologies GmbH, 2013, "Klassifikation von Massenbewegungen", retrieved: 27.10.2013]. The velocity depends on the kind of soil material, physical attributes and the type of movement (see Fig. 3).

kind of soil materials	rock (dry)	regolith, soil, allivium, ion and water	water and sediment
physical properties	hard, brittle, solid	vivid substance	fluid
kind of movement	fall, roll, slide, creep	flow within the mass	flow
	low	water content	high
very slowly $\leq 1\text{cm/year}$			
1 - 5km/h	<ul style="list-style-type: none"> <li>landslide <ul style="list-style-type: none"> <li>slump</li> <li>rock slide</li> </ul> </li> </ul>	<ul style="list-style-type: none"> <li>earth flow</li> <li>debris flow</li> <li>mud flow</li> </ul>	<ul style="list-style-type: none"> <li>river transport</li> </ul>
very fast $\geq 5\text{km/h}$	<ul style="list-style-type: none"> <li>rock fall</li> </ul>	<ul style="list-style-type: none"> <li>debris avalanche</li> </ul>	<ul style="list-style-type: none"> <li>mudslide</li> <li>river transport</li> </ul>

Figure 3: Processes and forms of mass movements  
[Freie Universität Berlin, 2013, "Geomorphologie", retrieved: 28.10.2013]

#### Creep: speed of movement lower than 1cm/year

- Soil creep:  
The lowest downward movement of slopes is soil creep, which is barely visible. Soil creep depends on the season, water content and temperature [GeoDZ, 2013, "Bodenkriechen", retrieved: 29.10.2013].

- Debris creep:  
This is also known as creep denudation. It is a slow movement of unconsolidated rock which means that loosely bound masses or easy deformable materials move on. A distinction can be made between two categories, solifluction (see next point) and continuous creep. The deformability of the mass is a significant precondition for this kind of creep. Moreover, clay content, water content, thickness of bulk density of the material and the hillslope are also preconditions of this creep [GeoDZ, 2013, "Kriechdenudation", retrieved: 29.10.2013]; [Freie Universität Berlin, 2013, "kontinuierliches Kriechen", retrieved: 07.11.2013].
- Solifluction:  
At last it can be explained that solifluction is a type of debris flow. Water-saturated soil moves slowly down the slope. A frozen underground is not provided but the term solifluction is often used for mass movements in permafrost soil. It can further be subdivided into Gelifluction, Gelisolifluction and other types of solifluction [GeoDZ, 2013, "Solifluktion", retrieved: 29.10.2013].

### Slip: speed of movement between 1km/h and 5km/h

- Landslide:  
This type of movement is caused by disturbances regarding the strength of forces at slopes. In addition it should be mentioned that it is a natural process. Layers like sand and sandstone or limestone on clayey soil are often reasons for landslides. A change of inclination, height of the embankment or the border between solid rock and unconsolidated rock are typical reasons for fault zones. Water from rainfalls or snow melt induce a reduced shear strength in the soil. The ground water causes pressure and reduces the steadfastness of the slope, too. Natural vibrations like earthquakes or volcanic eruptions and human generated vibrations like blasting operations, construction works or traffic can trigger a landslide. The velocity of movements ranges between 1cm per year up to several metres per second. The size of the movement depends on the depth of the slip plane. A distinction can be made between surface slides (depth of slip plane < 1.5m), flat slides (5 – 10m), deep slides (10 – 20m) and very deep slides (> 20m). Furthermore, there are two kinds of movement mechanism, a rotational and translational (or compound) movements. The rotational displacement has a spoon-shaped shear surface and occurs only in loose sediments. The characteristics of this movement is shown in Fig. 4. Translational movements like debris flow appear on planar surfaces and move along weakness zones [GeoDZ, 2013, "Hangrutschung", "Rotationsrutschung", "Translationsrutschung", retrieved: 29.10.2013]; [Bayerisches Landesamt für Umwelt, 2013, retrieved: 29.10.2013].

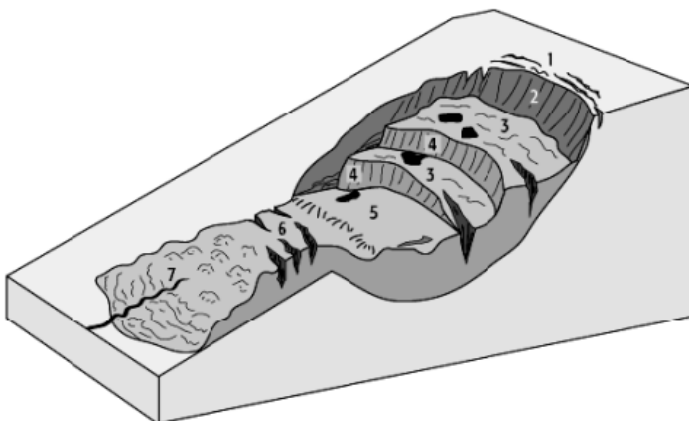


Figure 4: Rotational movement  
1) upper slope, 2) main demolition edge, 3) slid clod, 4) minor demolition edge, 5) main slide mass, 6) transverse tension cracks and 7) slide foot [GeoDZ, 2013, "Rotationsrutschung", retrieved: 28.10.2013].

- Earth flow:  
Earth flow can be seen as a mud flow and takes place at lower velocities. This movement includes a higher water content with fine-grained materials and looks like terraced steps. The tongue-shaped movement is complex.
- Debris flow:  
This type of slip is a translational landslide. Water and sediments form a viscous mixture which decreases the friction force. Rocks and debris, including trees and plants, slide by a tongue- or drop-shaped movement downwards. The velocity ranges from 1–5km/h [GeoDZ, 2013, "Schuttstrom", "Translationsrutschung", retrieved: 29.10.2013]; [PAUX Technologies GmbH, 2013, "Klassifikation von Massenbewegungen", retrieved: 27.10.2013].
- Mud flow:  
Mud flow can be counted to a field of debris flow. The amount of rocks and detrital is lower than for debris flows. More than 50% of this movement consists of clay and silt [GeoDZ, 2013, "Schuttstrom", retrieved: 29.10.2013]. This perception is also known in volcanology. An eruption of snow-covered volcano causes a rapid melting of snow and ice, which is consequently the main trigger of mud flows [Wissenswertes, 2013, "Schlammstrom", retrieved: 05.11.2013].

#### Fall: speed of movement faster than 5km/h

- Rock fall:  
The term rock fall includes also rock slide and rock slip. The differences are the size of the movements. With a volume up to  $10\text{m}^3$  the rock slip represent the smallest movement. Rock fall is termed as a fall with size of 10 to  $10^6\text{m}^3$ . If the volume exceeds the value of  $10^6\text{m}^3$  it is called rock slide. All of this movements can be counted to sudden mass movements. In most cases the actuator can be frost, temperature change, precipitation or vibrations by natural or human events. In these processes rocks can fall down and after a time period between seconds and few minutes the movement is finished. This type of mass movement leave clear marks after the mass movement. Fig. 5 describes the slump area from a rock fall [GeoDZ, 2013, "Bergsturz", retrieved: 31.10.2013]; [Bayerisches Landesamt für Umwelt, 2013, "Bergsturz, Felssturz, Steinschlag", retrieved: 31.10.2013] .

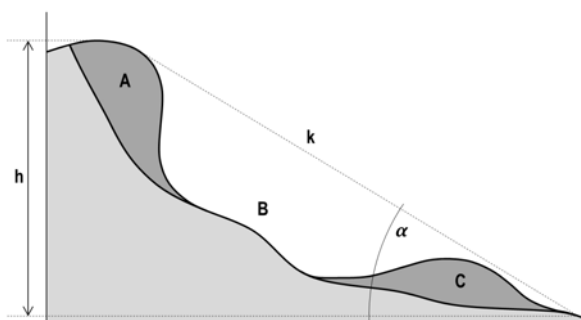


Figure 5: Area prone of rock fall  
A = demolition area, B = slump area,  
C = deposition area,  $\alpha$  = fall angle, h =  
drop height [m] and k = mean hillslope.

- Debris avalanche:  
This kind of fall is a type of volcanic eruption. In the case of a volcanic eruption it could happen that a part of a volcanic crater collapses. Big rocks mix with ash and detrital, which then slide down at a high velocity [Wissenswertes, 2013, "Schuttlawine", retrieved: 05.11.2013].

- **Mudslide:**

A mudslide is debris flow which occurs in high mountain regions. It is a mixture of detrital, sediment and water. The actuator is water, mostly after heavy rainfalls or snow melt [PAUX Technologies GmbH, 2013, "Schuttlawine", retrieved: 05.11.2013]; [Wissenswertes, 2013, "Schuttlawine", retrieved: 05.11.2013].

## 2.2 Review of geological settings of the Ciloto area

Indonesia has a rainy and a dry season. The average amount of precipitation is three times higher than in Austria. Water in the form of rain, groundwater as well as wet soil in the vicinity of rivers are the main actuators of mass movements. In Indonesia there are many mass movements which depend on water. One active movement is situated in the Ciloto area in West Java on the old main road between Jakarta (capital of Indonesia) and Bandung (provincial main city of West Java) on a kilometrage of 88.1km and on sea level of 1330m. This mass movement causes big problems in regard to the main road. The high density of the traffic is regarded as second most important actuator for this mass movement.

### 2.2.1 Morphology around Ciloto area

The area around the movement can be divided into five morphological parts (see Fig. 6).

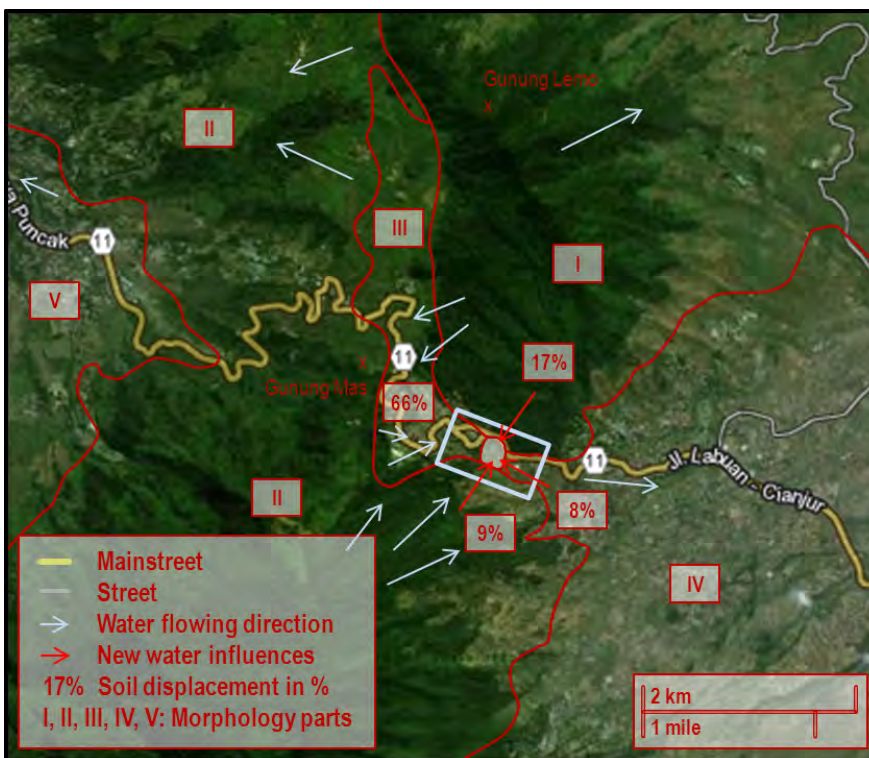


Figure 6: Influenced areas around Ciloto-Puncak  
 Part I: includes Gunung Lemo;  
 Part II: includes Pondok Cikoneng, Gunung Mas, Gunung Gedogan and Gunung Jongkok;  
 Part III: includes Puncak and Jember;  
 Part IV: includes Sindanglaya areas;  
 Part V: slope of Cempaka hillsides, Tugu and surrounding areas  
 [Sugalang, 1989, p. 6].

(© Google Inc. - www.maps.google.at) [Google Inc., 2013]

The morphology of Ciloto shows that the highest amount of precipitation appears in parts I and II (4000-5000mm per year). The pore water pressure increases and the groundwater, which accumulates in part III, penetrates the porous layer at the boundary to part IV. As soon as the groundwater passes part III, the pore water pressure increases in this area. The probability of a mass movement is given (see Fig. 6).

This is just one of several factors which cause the mass movement in Ciloto. Fig. 7 shows that the upper part of the movement has a higher slope angle ( $15^{\circ} - 20^{\circ}$ ) than the middle ( $7^{\circ} - 10^{\circ}$ ) and lower part ( $< 7^{\circ}$ ). The movement area ends in the the *Cijember river valley* (see Fig. 8).

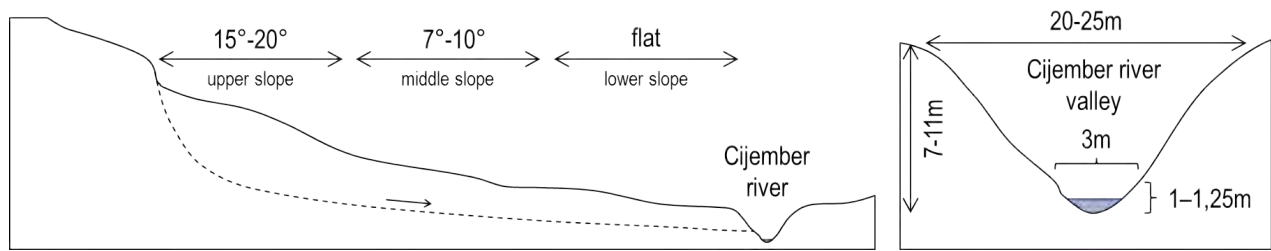


Figure 7: Slope situation and Cijember river valley  
[Sugalang, 1989, p. 5 and 13]



Figure 8: Cijember river valley

The Cijember river valley is very steep and the erosion on the lower slope of the valley is intense. The lateral support of the lower slope decreases with erosion. Also a vertical erosion is going on. Both erosions have negative influence on the slope stability. Several fish ponds (see Fig.9) and springs of water at different locations in the movement area are the reason for sufficient water saturation of the soil. The water penetrates into the soil.

### 2.2.2 Geological structure of Ciloto area

Two drilling cores (see Fig. 12) and a surface map of the slope cuttings helped to visualise the structure of the mass movement which is formed by several layers of soil and rock fragments. The river valley, the pore water pressure and the soil are reasons for complexity and irregularity of the movement. There is a translational major movement which includes an amount of small rotational movements (see Fig. 10).

The surface of the translational movement is spiked with cracks (see Fig. 11) from rotational movements. Water penetrates into the soil through these cracks easier. Thus, the pore water pressure ascends. Small rotational movements occur independently from other movements within the major movement. Also the major movement happens without any rotational movement in the slide. The movement directions are completely different, which makes the movement complex. The two drilling logs in Fig. 12 exhibit information about the structure of the movement and the sliding planes.



Figure 9: Fish ponds

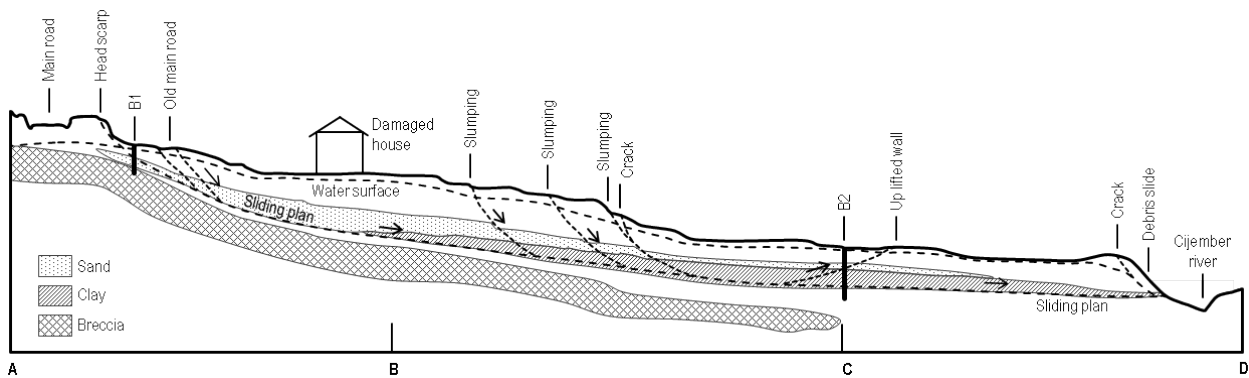
Figure 10: Geology map of the mass movement  
[Sugalang, 1989]

Figure 11: Cracks in the sliding area

**Clay and silt:**

Soil is the top layer of the subsurface, consists of clay and silt with high plasticity and is soft to solid. This layer reaches a depth of around 3 – 4m in both drillings (see Fig. 12).

**Silty sand and sandy clay:**

Sand is a permeable and unconsolidated layer which is loose, fine to coarse grained and includes water. This sandy clay conforms the sliding plane in drilling log no. 1 in a depth of 3 – 3.5m (Fig. 12) and is characterised by medium plasticity and soft consistency.

**Clay with a small amount of pebbles:**

This unconsolidated layer is a volcanic product, which is characterised by high plasticity



Drilling log no. B1						Drilling log no. B2					
Depth [m]	Classification		Water content	Consistence/Density	Lithologic description	Depth [m]	Classification		Water content	Consistence/Density	Lithologic description
1	CH	Clay	M	F	Soil	1					Soil
	ML	Silt	M	L							
2	GW	Gravels	W	S	Quarternary volcanic rock (tuff) Medium weathered	2	SC	Clayey sand	MW	L	Quarternary volcanic rock (tuff) Wet weathered Unconsolidated
	MH	Clayey silt	S	S					S	S	
3	↔		Loose sample			3	MH	Sandy silt	S	S	
4	CL	Sandy clay	S	M	Unconsolidated	4					Unconsolidated
5	SC	Clayey sand	S	M					S-W	F	
6	SM	Silty sand	S	L		6	GC	Clay with pebbles	S-W	F	
7						7					
8	CH	Clay	S	VSt	Clay	8		Sand			
9						9	↔		Loose sample		
10	BX	Breccia	S	VD	Quarternary volcanic rock Fresh	10		Silt			Lake sediment Unconsolidated
11						11		Gavels Sand			
						12		Silt			
						13					
						14	CH	Clay			
						15	↔	CH	Clay		
						16					Quarternary volcanic rock Unconsolidated
						17	ML	Silt			Lake sediment
						18		Silty clay			
						19					




<b>Notes:</b>		
	Undisturbed sample	
	Sliding plan	
	Groundwater	
<b>Classification:</b>		
C Clay	H High liquid limit	
M Silt	L Low liquid limit	
G Gravels	W Well graded	
S Sand	C Clayey	
	M Silty	
<b>Water content</b>	<b>Consistency</b>	<b>Relative Density</b>
D Dry	S Soft	L Loose
M Moist	F Firm	M Medium
W Wet	V Stiff	D Dense
S Saturated	VSt Very stiff	VD Very dense

Figure 12: Drilling logs  
[Sugalang, 1989, p. 11 and 12]

and lacking cohesion in dry conditions. This layer occurs at drilling log no. 1 at a depth of 8m (thickness around 1m) and at drilling log no. 2 at a depth of 4–7m (thickness around 3m).

### Breccia:

The bedrock of the subsurface is breccia, which is a hard and compact volcanic product. This is the deepest located layer in the upper and middle slope of the mass movement (see Fig. 7 and 10).

### Silt - clay:

At drilling log no. 2 at a depth between 9m and 16m a highly plastic layer of clay is situated. This 8m thick layer includes thin layers of sand with gravels and wood pieces. All layers (see drilling log no. 2 in Fig. 12) are located in the lower slope of the mass movement (see Fig. 7 and 10).

### 2.3 Review of mass movement phenomena over Ciloto area

This subsection focuses on the scientific work of Dr. Ir. Vera Sadarviana [Sadarviana, 2006]; [Sadarviana et al., 2009]; [Sadarviana et al., 2010].

In the time of 1986 to 2001 the sliding area was measured in nine periods by terrestrial measurements (total station). Two fixed observation points (*GD1* and *GD2*) were built solid in a stabilised area outside of the sliding area (see Fig. 13). The measurement points in the sliding area were measured by *Electronic Distance Measurement (EDM)* and theodolite measurements started from the fixed points. Horizontal and vertical displacements were calculated.

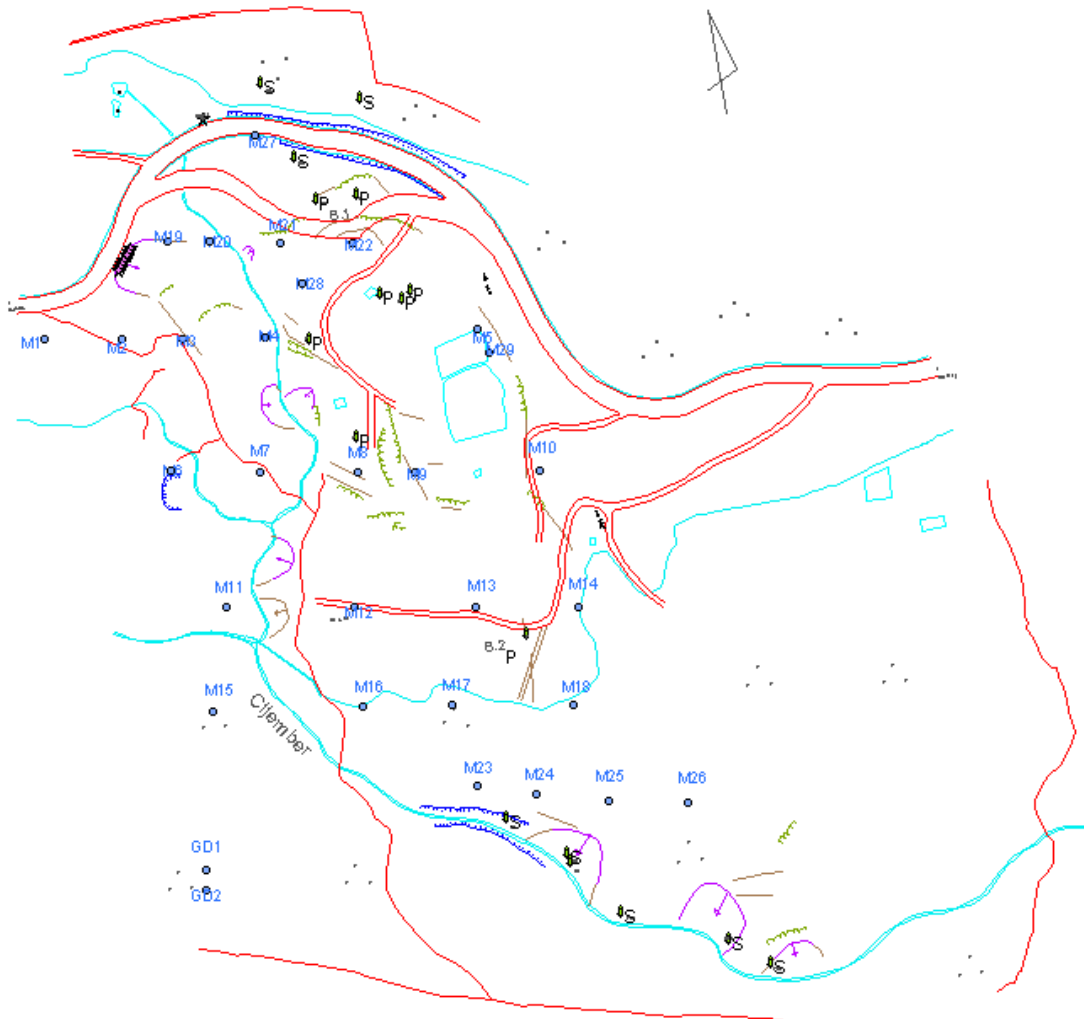


Figure 13: Terrestrial measurements  
[Sadarviana, 2006, p. 61]

Nearly every measurement point was observed in every period. The measurements were done in a local system so the points got local coordinates. *M10* was aligned to the WGS84, so it was possible to define all measurement points in the *Universal Transverse Mercator (UTM)* by using the *World Geodetic System 1984 (WGS84)* datum (see section 2.5).

The sliding area was split into three parts (see Fig. 7). The measurement points *M1 - M5*, *M19 - M22* and *M27 - M29* were located in the northern part in the slope. In the middle part point numbers *M6 - M15* were located. *M16 - M19* and *M23 - M26* were located in the southern part which is relatively flat.

The displacement vectors of the easting and northing directions, as well as the height differences were calculated from each point in a period to the same point in the following period. This information was used to calculate the horizontal and vertical displacements.

The evaluation of the nine periods during 1986 to 2001 showed the following results [Sadarviana, 2006, p. 66 - 76]:

- The horizontal displacements of the whole area occurred from north-west to south-east direction during the measurement periods.
- In the northern part the horizontal movements were smaller than in the middle and southern part.
- The vertical displacements were larger in the middle part than in the northern and southern part, which is contrary to the general tendency in a landslide area (one slope plane).
- Larger movements occurred in wet seasons (September to February) rather than in dry seasons (May to October).
- The sliding movement was categorised as 'very slow' with a velocity between  $5 * 10^{-5}$  and  $5 * 10^{-7} \frac{\text{mm}}{\text{s}}$ .

The precision of the measurement device type, which was used for the measurements, was unknown as well as the precision of the measurements of the terrestrial data. The resulting displacement were inconsistent and therefore the terrestrial measurements could not be used for additional researches [Sadarviana, 2006, p. 61 - 76].

### 2.3.1 Modelling of Ciloto area

In the years of 2002 to 2005 five measurement periods were carried out by GPS. Two reference stations (POS G and REF 2) were sited in stable locations around the sliding area and up to 15 points (GPS 1-14 and M010) were observed in the sliding area (see Fig. 14). These measurements were carried out to conduct the geometric models which are described in section 2.6.1.

### 2.3.2 Results

Based on the five measurement campaigns by GPS during 2002 to 2005 following models were created.

#### Static model

The results of the statistical significance test (described in section 2.6.3) showed that two points in the first and second measurement period between 2002 to 2005 were not significantly classified. But the alternative hypothesis of the significance test was accepted because both criteria in the criteria test (see Fig. 25) were true. This confirmed significant movements detected by the GPS measurements.

The solution of the static model showed the following:

- The points with the largest horizontal movement slid in south-east direction.
- Measurement points in the middle and southern slope (see Fig. 7) had a larger horizontal displacement than points in the northern slope.

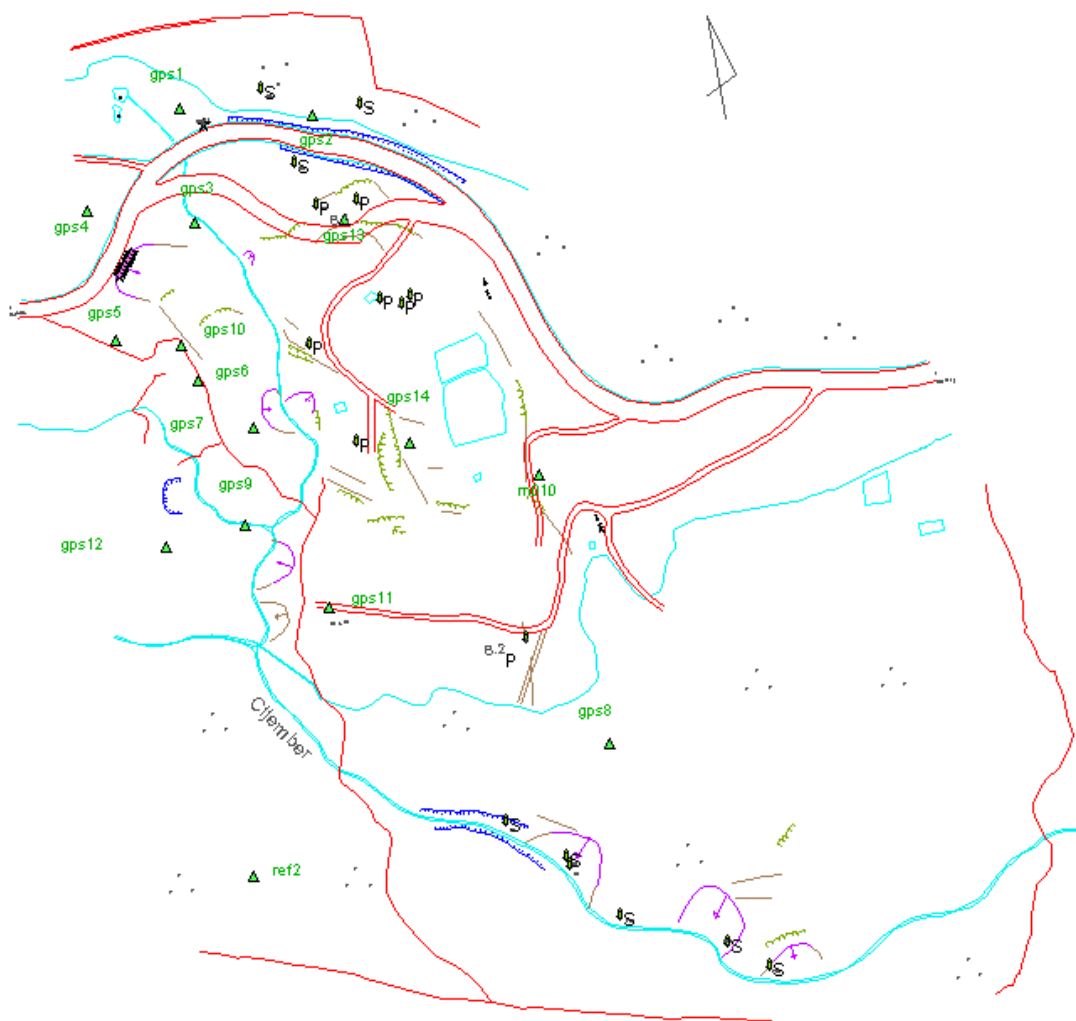


Figure 14: GPS measurements  
[Sadarviana, 2006, p. 79]

- Vertical displacements (positive and/or negative) occurred in all three parts.
- Positive vertical displacements, which were shown by half of the points, are typical for this kind of landslide because water flows had accumulated from the surrounding areas (see Fig. 6).
- The directions of the point displacements were not consistent. This irregularity occurred by the pressure of water infiltration in morphology unit I and II and seepage of water in morphology unit IV (see Fig. 6).

The Ciloto landslide may consist of two or more minor landslides, because movements happened in different strengths and forms (rotary, straight and compound). Concerning different directions movements occurred in different time and with different velocities. Especially the west side of the sliding area showed a wavy ground surface, which is an indication of a circular slip plane with more than one plane. The east side area showed a non-wavy surface which means that the slip plane is planar. The major scarp was observed at points GPS1, GPS2 and GPS4 (upper part - see Fig. 14). The slip is a complex and multiple rotational landslide with the main direction from north-west to south-east. This was also shown by the terrestrial measurements and the GPS observations in the statistic model [Sadarviana, 2006, p. 95 - 106].

### Kinematic model

Comparison of predicted data of a period  $k$  with results from observations of the same period showed that the predicted data pointed smaller values but the curves in the graphical view were similar. The predicted velocity and acceleration were longer than indicated by observations.

Kinematic model vs. static model:

- The statistical significance (see section 2.6.3) was checked by the *t-Student distribution* (hypotheses are seen in (2.18)). It is assumed that the null hypothesis follows a *t-Student distribution*. The results correspond to the results from the statistic model, where the null hypothesis was accepted for the same GPS points in the measurement period 1 and 2.
- The predicted results of the kinematic model for the cumulative horizontal displacement proved to be relatively similar to the static model. Only three points moved in a different direction.
- The most active vertical displacements of the kinematic model were similar to the statistic model. The vertical displacements spread evenly from the northern to the southern part whereas the middle part exhibits high horizontal movement.
- In the kinematic model some measurement points showed a larger vertical than horizontal displacement. This phenomenon could be interpreted because of the slope or the beginning of landslide fracture.

Displacement vs. displacement velocity of the kinematic model:

- The comparison of the horizontal displacements with their velocity proved the hypothesis that the maximum of the horizontal velocity is in the middle part of the landslide zone.
- The extent of displacement in north-east direction was larger than its velocity. The reason was the high water infiltration from the morphology unit I (see Fig. 6).
- On the northern and the southern part of the slide there is an intersection point of slip plane and ground surface. In this area big movements and velocities were identified in a vertical direction. In the middle part large displacements and velocities were detected in horizontal direction. There was a correlation between displacement and displacement velocity. It was also shown that a large horizontal movement had a large subsidence. Material with large subsidence tended to have a large displacement velocity until the intersection point of the slip plane and ground surface was reached. This result could be used to prove the hypothesis about the resultant of material velocity which reached the maximum value on the slip plane.

### Dynamic model

An additional physical parameter for the kinematic model was the change of *Ground Water Level (GWL)*. This parameter was represented by coefficients of rainfall, gravity, porosity and saturation. The *Kalman-filtering* (described in Niemeier [2008, p. 458-470] and Heunecke et al. [2013, p. 297-338]) was used to solve the problem. In addition to the kinematic model the change of GWL was calculated, too.

The results showed that the calculated position vector was similar to the measured position vector. The prediction of velocity and acceleration was different to the observed/calculated values. The GWL-coefficient had the same value in every period, but with different standard deviation each.

As with the kinematic model the statistical significance of the dynamic model was calculated by the t-Student distribution (see section 2.6.3). The used hypotheses are shown in (2.18). The result indicated a significant displacement concerning all points. So, the alternative hypothesis was set to be true. However it was not possible to find an indication of the existence of a slip in each period by the observation points.

The hypothesis about the maximum of the material displacement velocity on a slip plane was correlated with the predicted displacements and velocities from the dynamic model. But the material displacement under the surface showed smaller velocities than the displacement above the surface. The kinematic model had displayed a contrary solution.

The effect of changing GWL was detected by the prediction of the vector of the observation points when using the standard deviation of the observations. A correlation between the GWL and the geometric parameter was visible and showed by a high correlation ( $\pm 0.92\%$ ). The displacement of nearly all observed points correlated with the change of GWL.

The comparison between the kinematic model and the dynamic model displayed that the kinematic model gave the better results. The dynamic model had not given the maximum position vector status velocity and acceleration. The reason could be the GWL because a linear approximation was still used.

## 2.4 Basic principles of GNSS and TLS

### 2.4.1 Global Navigation Satellite Systems (GNSS)

*GNSS* is an acronym for satellite navigation systems. *Transit* was the first satellite navigation system in space, later replaced by the *Global Positioning System (GPS)*. Originally this GNSS was designed for military purposes. Today everybody can use GNSS for positioning, velocity and timing capabilities. All GNSS are similarly constructed and can be divided in three segments.

#### Space segment

A certain number of satellites of each satellite system circles the earth in a specific height and different orbits. Depending on their orbital heights they need approximately 12h to circumnavigate the earth. The realtime position of every satellite is known by an accuracy of 1m or even better. All satellites broadcast signals permanently and therefore users can check their position and/or velocity at any time.

#### Control segment

The main task of this segment is to monitor the position and clock behaviour of the satellites. *Tracking Stations* or *Monitor Stations* with known positions on earth observe the satellites permanently and a *Center Control* calculates the ephemerides. The orbit predictions are issued via the *Almanach* to the users and allow them to calculate their position on earth.

In summary, the control segment has following tasks:

- Checks the behaviour of the satellites.
- Performs control tasks.
- Monitors the behaviour of the satellite clocks.

Global monitor stations track the satellites permanently. The *Master Control Stations* process the data and perform the upload to the satellites.

### User segment

This segment includes all devices that can receive the corresponding satellite signals (receivers). Firm- and software are also part of it. As already mentioned the satellites broadcast the navigation signals permanently. GNSS receivers analyse this digital information to get their position on or near the earth's surface. It is referred to as a one-way process (downlink) because only satellites send information which is possible to receive.

More details about the GNSS configuration can be found in [Li, 2012, p. 12ff]; [Witte and Sparla, 2011, p. 410ff]; [Joeckel et al., 2008, p. 353ff]; [Kaplan and Hegarty, 2006, p. 67ff]; [Torge, 2003, p. 127ff].

Currently there are four GNSS in operation, the *Global Positioning System (GPS)*, the *GLOBAL NAVIGATION SATELLITE SYSTEM (GLONASS)*, *Galileo* and *BeiDou*. In Tab. 1 some key characteristics of the different systems are listed.

GNSS-system	GPS	GLONASS	Galileo <sup>2</sup>	BDS <sup>2</sup>
numbers of satellites	32	29	30	27
altitude	20.200km	19.100km	23.222km	21.528km
orbital planes	6	3	3	3
inclination	55°	64.8°	56°	55°
sidereal orbit period	11h 58min	11h 15min	~14h	~12h

Table 1: GNSS differences

[U.S.-Government, 2013, retrieved: 25.09.2013]; [Federal Space-Agency, 2013, retrieved: 25.09.2013]; [Sistemilaser, 2013, retrieved: 25.09.2013]; [European GNSS-Agency, 2013, retrieved: 25.09.2013]; [BeiDou, 2013, retrieved: 25.09.2013]

### Measurement principle

A GNSS receiver requires direct lines of sight to a minimum of four GNSS satellites to estimate its 3D position  $P$  (see Fig. 15). The satellites broadcast orbit and clock correction information to support local solutions of the receiver constantly. The ephemerides comprise of the actual satellite coordinates  $X^i$ ,  $Y^i$  and  $Z^i$  in a global reference system. The GPS reference system coincides with the *World Geodetic System 1984 (WGS84)* (see 2.5.1) and the origin of this system is in the center of mass of the earth.

---

<sup>2</sup>currently in construction

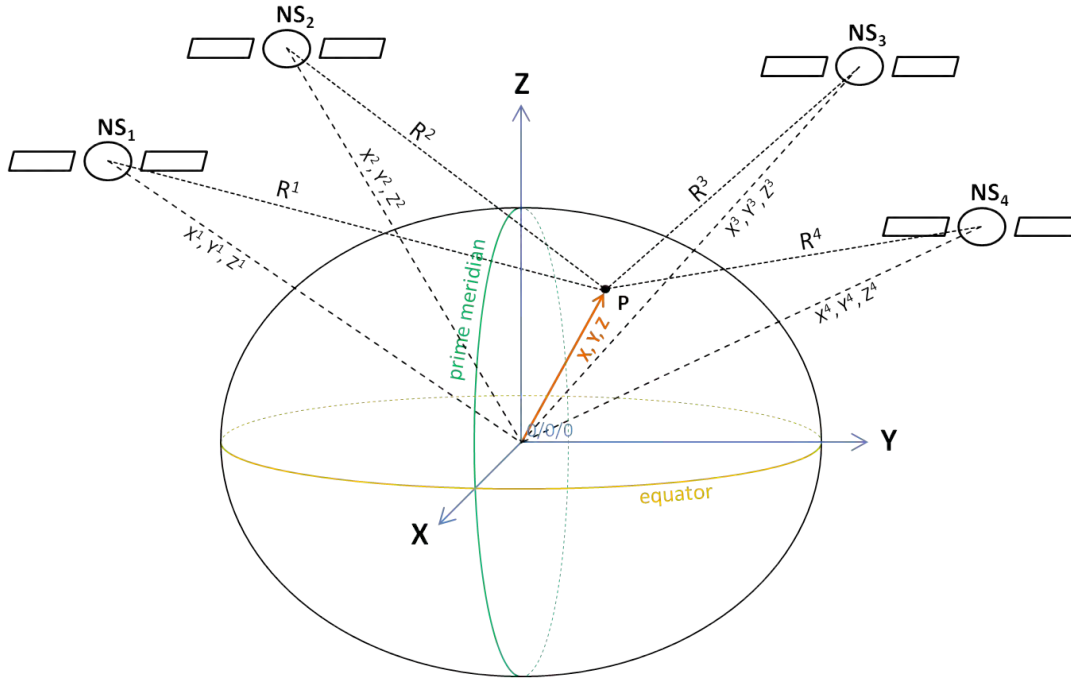


Figure 15: Positioning process of GNSS  
 [Joeckel et al., 2008, p. 355]; [Witte and Sparla, 2011, p. 412]

The distance  $R^i$  between a *Navigation Satellite (NS)* and the receiver  $P$  (see Fig. 15) is calculated from the *travel time measurement*. The calculation is based on the *Coarse/Acquisition code (C/A-code)* or the *Precise code (P(Y)-code)*. To get the geometrical position of point  $P$ , in theory it is sufficient to observe the geometrical distance (*pseudo range  $PR^i$*  - see (2.7) [Kaplan and Hegarty, 2006, p. 201]) between three NS and the receiver. [Joeckel et al., 2008, p. 354-357]

$$PR^i = c * [t_R - t_{t_{NS}}^i] \quad (2.7)$$

$c$  ... signal spreading rate [ $\frac{\text{m}}{\text{s}}$ ]  
 $t_R$  ... receiver time [s]  
 $t_{t_{NS}}^i$  ... transmitted satellite time [s]

As the receiver clock and the satellite clocks are not synchronised, it is necessary to observe a minimum of four NS. The accuracy is better than 10m (for devices which use the measurement by modulated carrier wave like navigation devices or smart phones) [Witte and Sparla, 2011, p. 412-413].

$$R^i = N^i * \lambda + \Delta\lambda + c * \Delta t \quad (2.8)$$

$R^i$  ... spatial distance between satellite  $i$  and receiver  
 $\lambda$  ... wavelength of the signal  
 $N^i$  ... ambiguity of the range  $R^i$   
 $c$  ... signal spreading rate of  $\lambda$   
 $\Delta t$  ... receiver clock error as related to the GNSS-system time

To increase the resolution of the distance measurement it is recommended to use phase-modulated carrier waves. Compared to code measurements the accuracy is improved by at



least a hundred times and more. The spatial distance  $R^i$  is composed of the integer ambiguity of the wavelength, rest of the phase-part and the receiver clock error (see (2.8) and Fig. 16).

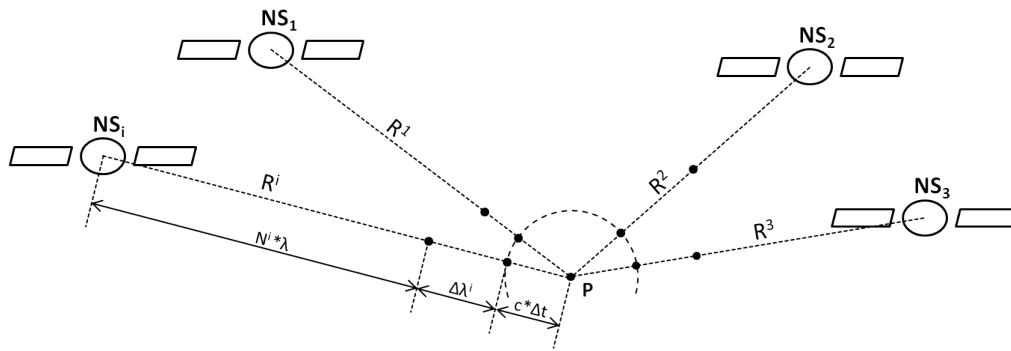


Figure 16: Improvement of the pseudo range  
[Joeckel et al., 2008, p. 356]

For Geodetic purposes the equation of (2.8) [Joeckel et al., 2008, p. 357] will be too inaccurate. GNSS receivers are dual-frequency receivers to correct for other influences. (2.9) [Joeckel et al., 2008, p. 400] represents the non-linear observation equation which includes all further relevant parameters.

$$PR^i = R^i - c * dt^i + c * dt - c * dt_{Iono} + c * dt_{Tropo} + c * dt_{Multi} + \lambda * N^i + \varepsilon^i \quad (2.9)$$

$R^i$	...	spatial distance between satellite $i$ and receiver
$c * dt^i$	...	satellite clock error
$c * dt$	...	receiver clock error
$c * dt_{Iono}$	...	influence of the ionosphere
$c * dt_{Tropo}$	...	influence of the troposphere
$c * dt_{Multi}$	...	influences of multipath, imaging and phase center
$\lambda * N^i$	...	ambiguity
$\varepsilon^i$	...	random error of measurements

The components are externally modelled values or estimated parameters. Another way is to eliminate the components by linear combination or to reduce them differential techniques.

### Evaluation process

A measurement accuracy of 1cm is accessible by observations with carrier phases. To reduce fault effects, there are two requirements [Joeckel et al., 2008, p. 409]:

- The usage of dual-frequency receivers reduce the ionospheric effect and estimate the ambiguities faster.
- Second, the usage of devices which evaluate carrier phases and code phases.

Fault effects can be eliminated (clock errors and satellite and receiver hardware errors) or minimised (like satellite orbit errors, ionospheric and tropospheric errors). In Fig. 17 three types of GNSS differences are depicted.

In case of Fig. 17a two receivers collect the data from one satellite. The equation of the *Single Difference (SD)* is a subtraction of the two observation equations (2.9) from  $P_1$  and  $P_2$ . Therefore the SD the satellite clock error ( $c * dt^i$ ) is eliminated. Fig. 17b shows the difference

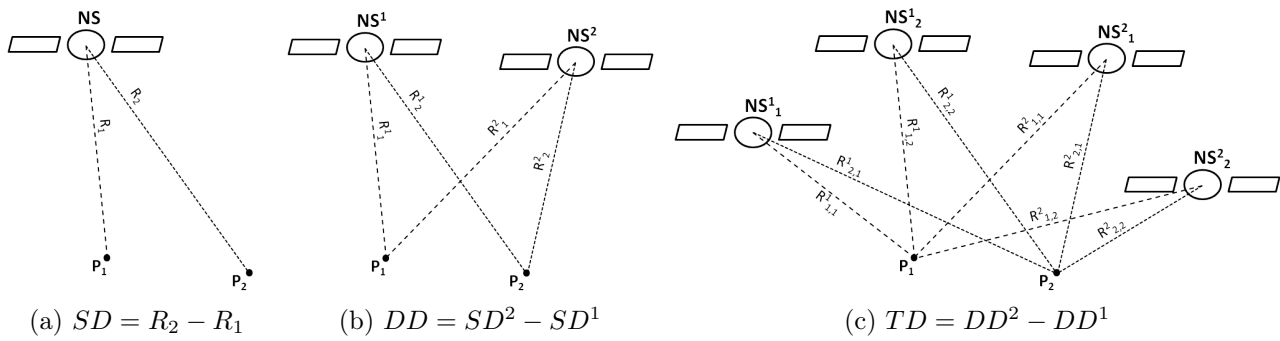


Figure 17: Single differences, double differences and triple differences  
[Joeckel et al., 2008, p. 411-415]

of two SD which is called *Double Difference (DD)*. In addition to the satellite clock error the receiver clock error ( $c * dt$ ) is eliminated, too. Case number three is shown in Fig. 17c there, subtraction of two DD (*Triple Difference (TD)*) enables an approximate determination of baselines without knowing the ambiguities ( $\lambda * N^i$ ) and removes cycle slips.

The commonly used method is the DD, because this observation equation is largely free of systematic errors [Joeckel et al., 2008, p. 411-415].

### 2.4.2 Terrestrial Laser Scanning (TLS)

TLS is a young and completely static measurement method. The measurement device ascertained the object extensively. In a short time and in a close grid the polar coordinates from the object is recorded without a reflector. The evaluation is done in post processing [Joeckel et al., 2008, p. 318ff].

#### Functionality of TLS

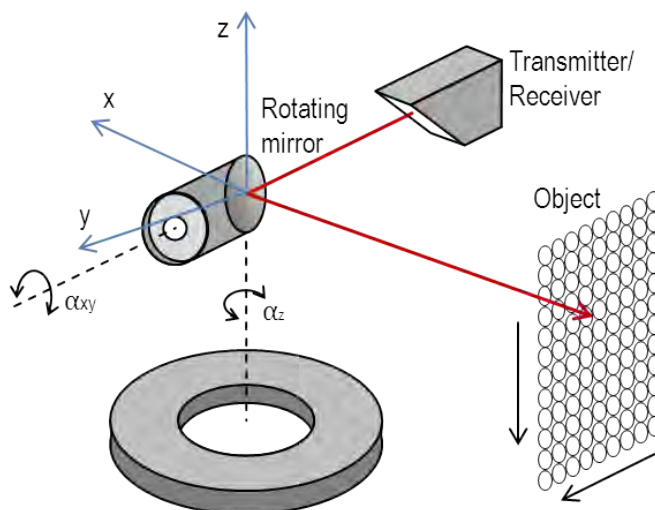


Figure 18: Range, vertical and horizontal rotations of panorama scanner

[Shan and Toth, 2009, p. 90]

Regarding the TLS a laser beam is sent out of the device and reflected by the object. The intensity of the laser beam, which arrives back at the device, depends on the surface characteristics (roughness, interference, reflectance), the material properties (absorption, reflection, refraction) and the geometry (multipath effect, distance to object, angle of incidence, divergence) of the measuring object [Witte and Sparla, 2011, p. 327ff]. The range of the measured point is measured by a laser rangefinder. To get a point cloud in a three dimensional area, the TLS has to move in two directions (horizontal and vertical). A mirror, which rotates around a horizontal axis, directs the laser beam in a vertical plane.

The device rotates also slowly around a vertical axis to get information about the horizontal plane (hybrid and panorama scanner - see Classification of TLS). Both axes pass through the center of the instrument. It depends on the

measuring device, but it is possible to measure more than 1.000.000 points per second. The device saves the distances, the information about the laser beam intensity, and the measured angles from the horizontal and vertical planes (polar coordinates - see Registration) (see Fig. 18).

### Classification of TLS

One kind of classification is the classification about surface characteristics, material properties and geometry (see Functionality of TLS). Other types of classification of TLS are the classifications about the accuracy or the classification about the distance measurement system (phase-ranging or pulse-ranging - see Properties of TLS instruments). But the most popular classification of scanning mechanisms is to classify the laser scanners into three types (see Fig. 19):

- Camera scanner: detects an object section similar to a photograph.
- Hybrid scanner: All-round scanner with limited height range.
- Panorama scanner: All-round scanner, which is also able measurements above the zenith.

The manner of deflection of the laser beam depends on the type of the laser scanner.

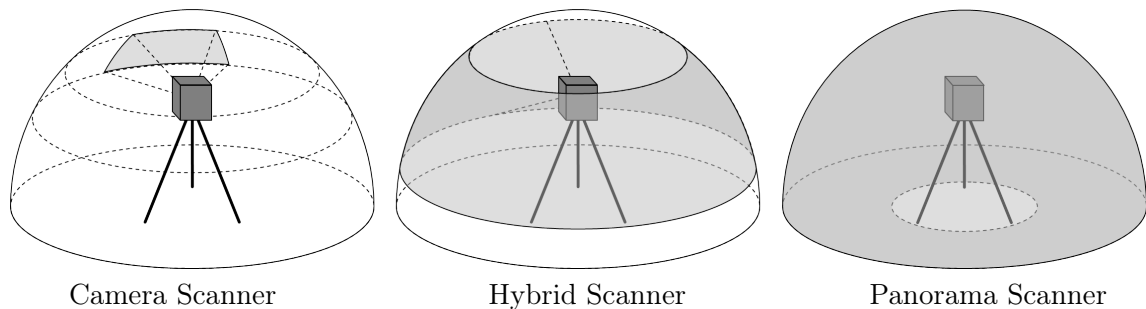


Figure 19: Classification of TLS  
[Joeckel et al., 2008, p. 325]

#### Camera scanner:

Camera scanners or TV-scanners are used for short-range and medium-range areas. The typical *Field of View (FoV)* is  $40^\circ$  horizontally and vertically each. The laser beam leaves the device through this small window and is distracted by two oscillating plane mirrors in  $x$ - and  $y$ -direction. The returning parts of the laser beam go back the same way to the transmitter, which is also the receiver. The device is permanently fixed for the duration of the measurements. Fig. 20 shows a variety of the function principle of the camera scanner. Another variety is when the  $y$ -rotate mirror rotates around the  $z$ -axis [Joeckel et al., 2008, p. 325-326]; [Shan and Toth, 2009, p. 91-92].

#### Hybride scanner:

This kind of laser scanner is similarly structured as a total station. It is possible to scan the complete horizon. The view is limited in vertical direction by  $50^\circ - 60^\circ$ . For some devices it is possible to tilt the head of the scanner. In this case the  $xy$ -plane is not the horizontal plane of the earth. The function principle of the hybrid scanner is different to that of camera scanner. One rotating polygon mirror in the  $xy$ -plane distracts the laser beam in vertical direction (see Fig. 21). The device rotates slowly around the  $z$ -axis. In this case the laser beam is distracted in horizontal direction by the full  $360^\circ$ . Hybrid scanners are constructed for the surveying market. The coverage of this device is for medium-range areas up to long-range areas. It is also possible to use them indoors [Joeckel et al., 2008, p. 327-328]; [Shan and Toth, 2009, p. 91].

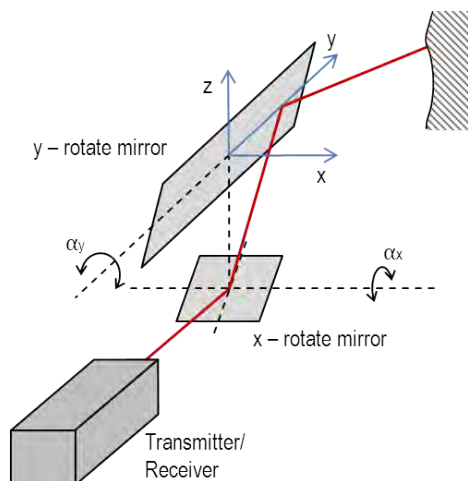


Figure 20: Principle of camera scanner

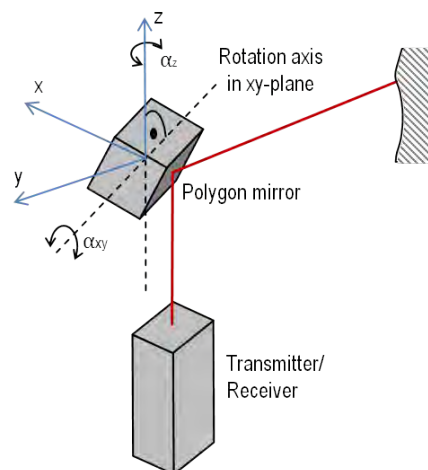


Figure 21: Principle of hybrid scanner

[Joeckel et al., 2008, p. 236]

### Panorama scanner:

In terms of the functionality of laser beam distraction in Fig. 18, it is noticeable that the laser beam describes a full  $360^\circ$  in both horizontal and vertical directions. The mirror rotates around the horizontal axis in the  $xy$ -plane passing the center of the instrument. The device rotates slowly around the vertical axis like the hybrid scanner. Theoretically it is possible to have a FoV like a sphere. However practically the FoV is limited in the vertical plane by  $320^\circ$ . The area under the device can not be scanned because of the device and their tripod. Panorama scanners are optimal for indoor scanning like large halls, churches or rooms but are also useful in the context of topographic mapping. This measuring device is used for medium-range areas [Joeckel et al., 2008, p. 328-330]; [Shan and Toth, 2009, p. 91].

### Properties of TLS instruments

The quality and the efficiency of the measurements do not only depend on the type of scanner (see Classification of TLS). The devices can also be differentiated by the kind of distance measurement. In contrast to pulse-ranging, some facts about phase-ranging should be taken into account:

- It is the faster procedure.
- Second, it uses a smaller angle of divergence.
- Third, it has a smaller diameter laser beam.
- Furthermore it attains the better accuracy.
- Last, it has a reduced *Signal Noise Ratio (SNR)*.

The less SNR limits the coverage of the measuring. The pulse-ranging is the better choice for long-range areas. The choice of the right instrument depends on the task (Tab. 2).

A combination of phase- and pulse-ranging is called *Pulse-Wave-Procedure*. The advantage of pulse-ranging is the long coverage, while that of the phase-ranging is the high accuracy.

device	Camera scanner	Hybrid scanner	Panorama scanner
possible for indoor measurements	•	•	•
short-range - up to 100m	•		
medium-range - up to 350m	•	•	•
long-range - more than 500m		•	
impulse-ranging	•	•	•
phase-ranging	•		

Table 2: Application fields of TLS

[Shan and Toth, 2009, p. 87ff]; [Witte and Sparla, 2011, p. 324ff]

## Registration

The registration process of point clouds includes two steps. One step is the nexus of the single scans, the other is the georeferencing of the point clouds. Both of them need a 3D transformation to calculate the transformed observation point coordinates  $X$ ,  $Y$  and  $Z$  (2.10) or to estimate the transformation parameters (more details in Niemeier [2008, p. 342ff], [Eling, 2009, p. 19-22] and Kraus [2004, p. 473-476]).

$$\begin{pmatrix} X \\ Y \\ Z \end{pmatrix} = \begin{pmatrix} X_0 \\ Y_0 \\ Z_0 \end{pmatrix} + R_{\omega\phi\kappa} \begin{pmatrix} x \\ y \\ z \end{pmatrix} \quad \text{with} \quad \begin{pmatrix} x \\ y \\ z \end{pmatrix} = \begin{pmatrix} s * \sin \xi * \cos \alpha \\ s * \sin \xi * \sin \alpha \\ s * \cos \xi \end{pmatrix} \quad (2.10)$$

$\xi$  = crown angle (direction of  $\xi = 0 = \kappa$ -axis)

$\alpha$  = horizontal angle in  $\omega\phi$ -plane starting by  $\alpha = 0$  (compare with Fig. 22)

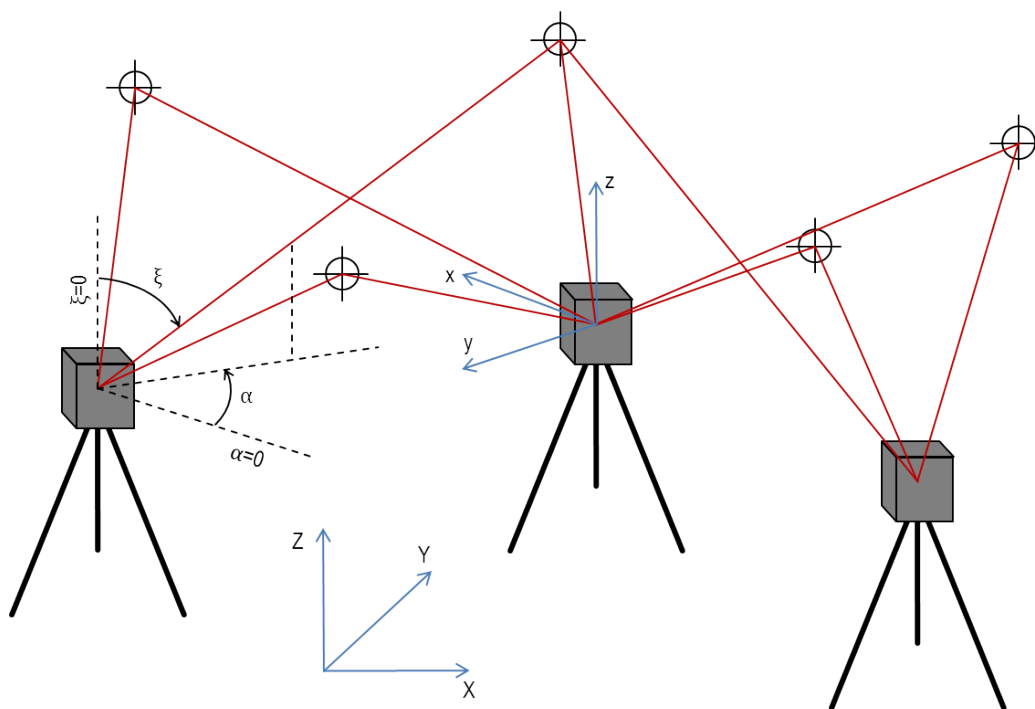


Figure 22: Georeferencing  
 $\xi$  = crown angle,  $\alpha$  = horizontal angle

**Nexus of single point clouds:**

This step is possible to do by different procedures which need minimum three identical points or planes in two systems. All of them have advantages and disadvantages [Kraus, 2004, p. 476-482]; [Eling, 2009, p. 22-25]:

- **Identical points:**  
Identical points (tie points) can be 3D objects like balls, cylinders or cones. 2D tie points are mostly target marks like retro-reflectors. 3D points can be seen and scanned from all sides, whereas 2D target marks are easier to install in the measurement area. 3D objects are mounted on tripods, the 2D tie points can be attached also on walls or other existing objects. A good accuracy and reliable estimation of the transformation parameters of the nexus result depends on the adequate number of identical points as well as the size of the target marks which are installed in the measurement area. The nexus of identical points provides an exact and reliable solution. The installation of target marks needs a lot of time as well as the fine-grained scans of the tie points. In the case of georeferencing it is also necessary to do measurements to the tie points.
- **Object geometry:**  
Objects can be 3D points like the identical points or planes in the measurement area. It is possible to link two point clouds by identification of minimum three equal planes of the 3D measurement object (streets, walls,...). In this case it is not necessary to install target marks. There are procedures to estimate the transformation parameters of the 3D transformation by the help of normals and distance parameters of the scanned planes. The quality of the solution depends on the identification of the planes. The results are similar to the results of the identical points.
- **Iterative Closest Point (ICP):**  
This kind of nexus connects pairs of points in two point clouds. It is an iterative process and stops when all pairs of points are found and the square sum of distances between the points is a minimum. For this type of nexus no target marks are necessary.

**Georeferencing:**

Georeferencing describes the transformation of point clouds, which are measured in a local coordinate system, into a superior coordinate system. A distinction is made between the two types (see Fig. 22) [Kraus, 2004, p. 473-476]:

- **Direct georeferencing:**  
In this case the coordinates of the viewpoints of the TLS devices are known, e.g. by GPS-measurements. By the estimation of the 3D transformation parameters it is possible to omit the translation parameter. The rotation parameters are necessary to orientate the point clouds to the target marks.
- **Indirect georeferencing:**  
It is also possible to use the coordinates for the target marks to georeference the point clouds. In this case it is necessary to calculate backwards to the viewpoint coordinates of the TLS device.

**Estimation of the accuracy**

The transformation parameters and their accuracies are calculated by a bundle block adjustment. The advantage is that all parameters and their accuracies are estimated in one iterative step [Eling, 2009, p. 66-69]; [Kraus, 2004, p. 299-304].

The basic formula for the adjustment is written in (2.10). Based on the *Gauß-Markov* model the equations (2.11) are formed:

$$\begin{aligned} X &= X_0 + r_{11} * x + r_{12} * y + r_{13} * z \\ Y &= Y_0 + r_{21} * x + r_{22} * y + r_{23} * z \\ Z &= Z_0 + r_{31} * x + r_{32} * y + r_{33} * z \end{aligned} \quad \text{with} \quad R_{\omega\phi\kappa} = \begin{pmatrix} r_{11} & r_{12} & r_{13} \\ r_{21} & r_{22} & r_{23} \\ r_{31} & r_{32} & r_{33} \end{pmatrix} \quad (2.11)$$

The design matrix  $A$  is formed by the derivations of the equations (2.11). For the orientation of the observation points, derivations to the variable for the translations ( $X_0, Y_0, Z_0$ ) and rotation angles ( $\omega, \phi, \kappa$ ) are to do (6 parameters). The derivation with respect to the variables  $x, y$  and  $z$  contribute to the estimation of the coordinates of the target marks. In the end the design matrix  $A$  get a form like in Tab. 3.

	orientation parameters of standing points										position of target marks									
	$X_{01}$	$Y_{01}$	$Z_{01}$	$\omega_1$	$\phi_1$	$\kappa_1$	$X_{02}$	$Y_{02}$	$Z_{02}$	$\omega_2$	$\phi_2$	$\kappa_2$	...	$x_1$	$y_1$	$z_1$	$x_2$	$y_2$	$z_2$	...
$X$	$a_1$	$a_2$	$a_3$	$a_4$	$a_5$	$a_6$								$a_7$	$a_8$	$a_9$				
$Y$	$b_1$	$b_2$	$b_3$	$b_4$	$b_5$	$b_6$								$a_7$	$a_8$	$a_9$				
$Z$	$c_1$	$c_2$	$c_3$	$c_4$	$c_5$	$c_6$								$a_7$	$a_8$	$a_9$				
$X$	$a_1$	$a_2$	$a_3$	$a_4$	$a_5$	$a_6$											$a_7$	$a_8$	$a_9$	
$Y$	$b_1$	$b_2$	$b_3$	$b_4$	$b_5$	$b_6$											$a_7$	$a_8$	$a_9$	
$Z$	$c_1$	$c_2$	$c_3$	$c_4$	$c_5$	$c_6$											$a_7$	$a_8$	$a_9$	
	depends on measured target marks at standing points												...							
$X$							$a_1$	$a_2$	$a_3$	$a_4$	$a_5$	$a_6$		$a_7$	$a_8$	$a_9$				
$Y$							$b_1$	$b_2$	$b_3$	$b_4$	$b_5$	$b_6$		$a_7$	$a_8$	$a_9$				
$Z$							$c_1$	$c_2$	$c_3$	$c_4$	$c_5$	$c_6$		$a_7$	$a_8$	$a_9$				

Table 3: Construction of the design matrix  $A$

The calculation of the wanted parameters in vector  $\mathbf{x}$ , orientation of the observation point ( $X_{0n}, Y_{0n}, Z_{0n}$  and  $\omega_n, \phi_n, \kappa_n$ ) and the positions of the reflectors ( $x_m, y_m, z_m$ ) is shown in (2.15). With this solution it is possible to compute the variances and covariances in the *covariance matrix*  $\Sigma_{ll}$  of the observations  $l$ . From  $\Sigma_{ll}$  it is feasible to calculate the *variance factor*  $\sigma_0^2$  and the *cofactor matrix*  $Q_{ll}$ . The *weight matrix*  $P$  is formed by the inverse of  $Q_{ll}$  (see (2.12)).

$$\Sigma_{ll} * \frac{1}{\sigma_0^2} = Q_{ll} \quad P = Q_{ll}^{-1} \quad (2.12)$$

The minimum of the differences of the *unit weight errors*  $\hat{\sigma}_0$  between the two last iterations is the breaking criterion for the iteration of the adjustment. The calculated cofactor matrix  $Q_{xx}$  is multiply with  $\hat{\sigma}_0$ . The square root of the values of the main diagonal from the resulting covariance matrix  $\Sigma_{xx}$  provides the accuracies  $\hat{\sigma}_{xk}$  of the estimated parameters  $\mathbf{x}$ .

$$\hat{\sigma}_0 = \sqrt{\frac{v^T * P * v}{n - u}} \quad Q_{xx} = (A^T * P * A)^{-1} \quad \Sigma_{xx} = \hat{\sigma}_0 * Q_{xx} \quad \hat{\sigma}_{xk} = \sqrt{s_{kk}} \quad (2.13)$$

With help of the law of the *covariance error propagation* it is possible to calculate the covariance matrix  $\Sigma_{yy}$  (2.14) from several errors [Niemeier, 2008, p. 50 - 56].

$$\Sigma_{yy} = A * \Sigma_{xx} * A^T \quad (2.14)$$

$$\mathbf{x} = A^T * P * A - A^T * P * l = \begin{pmatrix} X_{01} \\ Y_{01} \\ Z_{01} \\ \omega_1 \\ \phi_1 \\ \kappa_1 \\ \vdots \\ X_{0n} \\ Y_{0n} \\ Z_{0n} \\ \omega_n \\ \phi_n \\ \kappa_n \\ x_1 \\ y_1 \\ z_1 \\ \vdots \\ x_m \\ y_m \\ z_m \end{pmatrix} \quad (2.15)$$

$A$	...	Design matrix	$X_{0n}, Y_{0n}, Z_{0n}$	...	Correction of translations
$P$	...	Weight matrix	$\omega_n, \phi_n, \kappa_n$	...	Correction of rotations
$l$	...	Vector of observations	$x_m, y_m, z_m$	...	Correction of the target mark positions

## 2.5 Coordinate systems

A coordinate system is a framework. Spatial and time referenced points are described geometrically in this system. Starting linearly from the origin, independent vectors build the axes of the system. The most popular coordinate system is the *right-hand Cartesian coordinate system* with a 2D ( $X$  and  $Y$ ) or a 3D ( $X$ ,  $Y$  and  $Z$ ) square system [GeoDZ, 2013, retrieved: 16.07.2014].

### 2.5.1 Earth-Centered, Earth-Fixed (ECEF)

The ECEF represents positions in  $X$ ,  $Y$  and  $Z$  directions in a 3D Cartesian coordinate system. The origin is defined by the center of mass of the earth (Earth-Centered). The axes are orientated by the *International Reference Meridian (IRM)* and the *International Reference Pole (IRP)*. They are fixed to surface of the earth (Earth-Fixed).

The coordinate system is a right-hand-system. The  $XY$ -plane is in the equatorial plane. The direction of the  $X$ -axis points in direction through the prime meridian (Greenwich). The  $Y$ -axis is perpendicular to the  $X$ -axis. The positive  $Z$ -axis points to the north and represents the



central rotation axis of the earth (see Fig. 23). The *World Geodetic System 1984 (WGS84)* (see section 2.4.1) [Gruber and Joeckel, 2011, p. 31] is a well known representative of an ECEF.

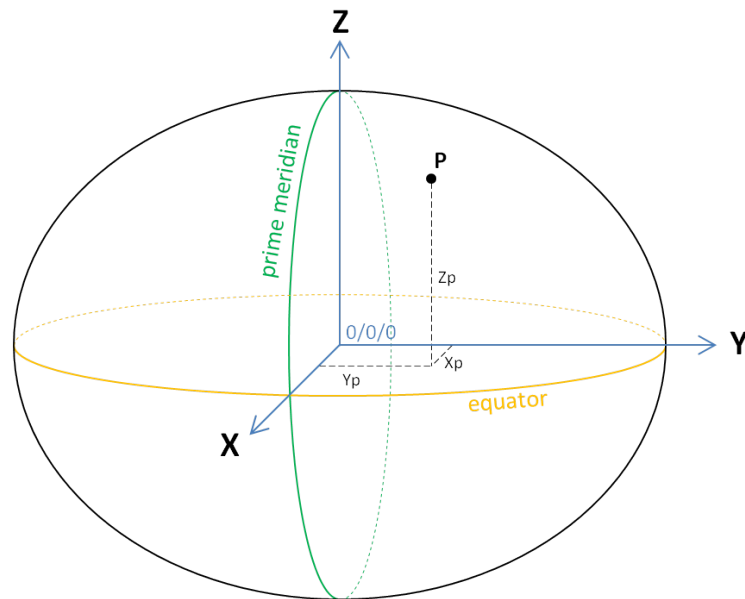


Figure 23: Geocentric coordinate system

### 2.5.2 UTM-coordinates

The *Universal Transverse Mercator (UTM) System* is a conformal mapping from points in a square coordinate system. The UTM defines 60 vertical zones with a width of  $6^\circ$  per zone. Equidistance is not given in the principal meridian, but two curved lines in a distance of 180km (90km left and right of the principal meridian) are equidistant. The area between the curved lines is clinched while outside the area the mapping is stretched [Witte and Sparla, 2011, p. 25ff].

The first UTM-zone starts at the principal meridian 177 west, the last zone number 60 ends at the principal meridian 177 east. With equation (2.16) the zone of a known principal meridian can be calculated.

$$Z = \frac{L_0 + 3^\circ}{6^\circ} + 30 \quad (2.16)$$

$Z$  = number of UTM-zone;  $L_0$  = principal meridian

For example Vienna is located close to the principal meridian of  $15^\circ$ . Therefore Vienna is located in the UTM zone number 33 [Gruber and Joeckel, 2011, p. 36].

## 2.6 Monitoring

The term *Monitoring* comprises capture, observation and surveillance of processes. Observation systems and technical tools are necessary. The recording of data from environmental influences and movements are helpful to create models of the movement behaviour of settlements, investigations, surveillances or slides. Especially movements of buildings or earth

surfaces are often in a close connection. Both of them are typical monitoring tasks of engineering geodesy.

### 2.6.1 Monitoring and modelling methods of mass movements

With respect to economies and physics it is difficult to observe a building or a sliding permanently and holistically. In this case the object is abstracted. This means that representative measurement points on the building or movement are chosen which represent the movement of the whole object. This discrete observation is split in a temporal and a spatial part.

- Spatial discretisation: deals with the holistic spatial movements of objects by measuring a few representative measurement points.
- Temporal discretisation: gives information about temporal changes of objects by repeated measurements (periods) of the observation points.

To create different models about the movement behaviour of an object, a reference measurement of the discrete measurement points is necessary. The path of motion depends on the rate of the measurements and the temporal distance between the measurement periods [Kuntsche, 2000, p. 228-289]; [Eling, 2009, p. 36-41]; [Rapp, 2011].

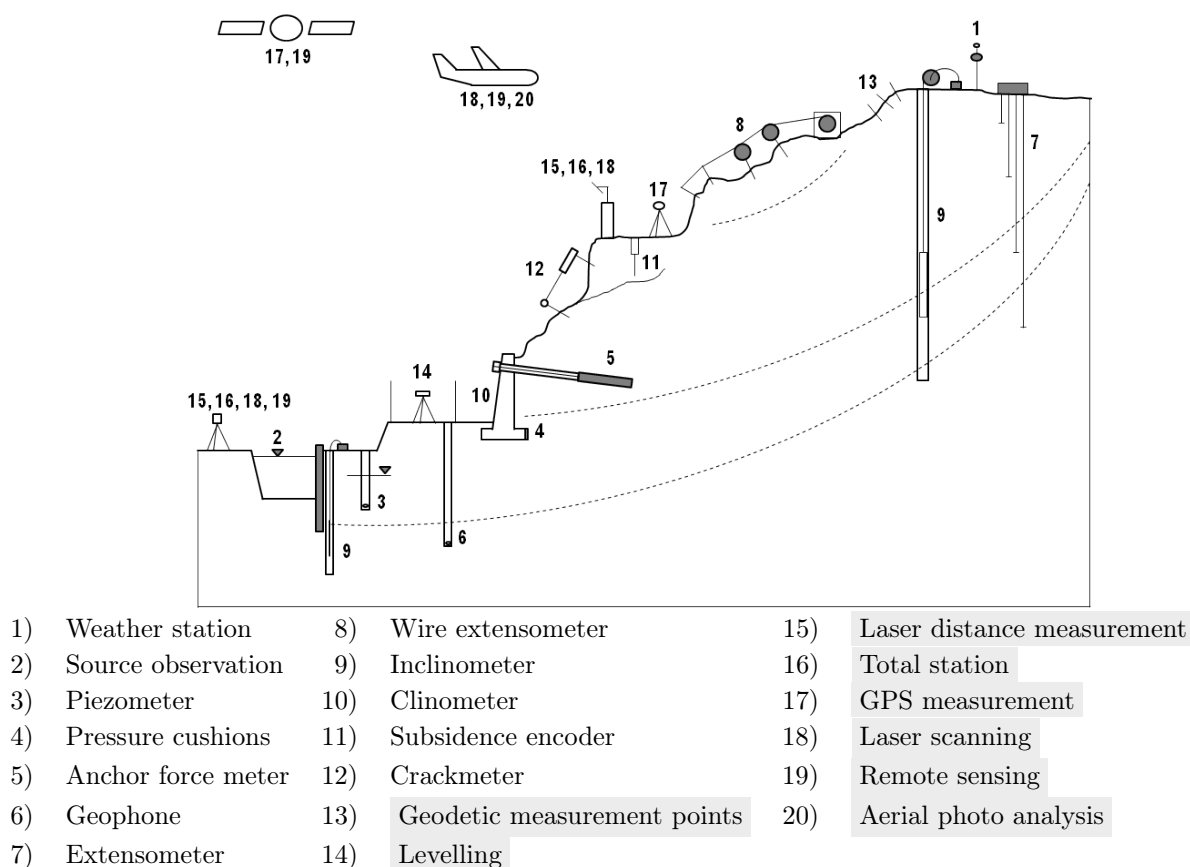


Figure 24: Monitoring methods  
 [Kuntsche, 2000, p. 228-289]; [Rapp, 2011, p. 22]  
 ... geodetic measurement methods

For monitoring, a variety of measurement systems can be used. Fig. 24 gives an overview of geodetic, geotechnical and physical monitoring methods for slips. With the collected discrete data from these systems, the geometric models in Tab. 4 can be created.

	time:	causal force:	status of the object:
Congruence model	no	no	in balance
Kinematic model	function of time	no	in motion
Static model	no	displacement as function of time	in balance
Dynamic model	movement as function of time and force		in motion

Table 4: Classification of deformation models

[Niemeier, 2008, p. 435]

The congruence model and the kinematic model are *descriptive models*. The congruence model informs about geometric changes. If the geometric changes are construed as functions of time they are called kinematic models (it works with regression analysis or Kalman-filtering).

The static model and the dynamic model are denoted as *causal models*. Basically, the acting force is a part of these models. Especially for the dynamic model, the time-varying force is considered [Niemeier, 2008, p. 435].

### Congruence model:

Neither the time nor the effect of deformation is reproduced in this model. The equation of the geometric conditions between two or more measured periods gives information whether a deformation has occurred. For the evaluation of deformations physical parameters are included which are not modelled. To check the significance of the deformation, e.g. the *t-Student distribution* can be used (see section 2.6.3).

### Static model:

In this model the acting forces and their resulting deformations are placed in a functional relationship. The time is not modelled. For a geometrical comparison the deformations are based on the differences of the coordinates (2.17).

$$d_j = x_j^{(k-1)} - x_j^{(k)} \quad (2.17)$$

$$\begin{array}{ll} d_j & \dots \text{ changes of the coordinate vectors} \\ x_j^{(k-1)}, x_j^{(k)} & \dots \text{ point coordinates from period } (k-1) \text{ and } k \end{array}$$

With the statistical t-Student distribution it is possible to find the significance of the displacements of the observed points. The used null hypothesis and the alternative hypothesis are seen in (2.18). A positive null hypothesis informs about no movement. Information about significant displacements are given by a positive alternative hypothesis (confirms a negative null hypothesis).

$$H_0 : d_j = x_j^{(k-1)} - x_j^{(k)} = 0 \quad H_1 : d_j \neq 0 \quad (2.18)$$

Null hypothesis

Alternative hypothesis

To control the t-Student distribution another check for significant displacements can be done. For this test two criteria must be true (see Fig. 25).

- The ground movement occurs when the distance  $D \neq D'$  between an observed point and the reference point from one to another period is different.
- The moving direction ( $\alpha$ ) changes between two periods in comparison to the previous periods if the first criterion is wrong.

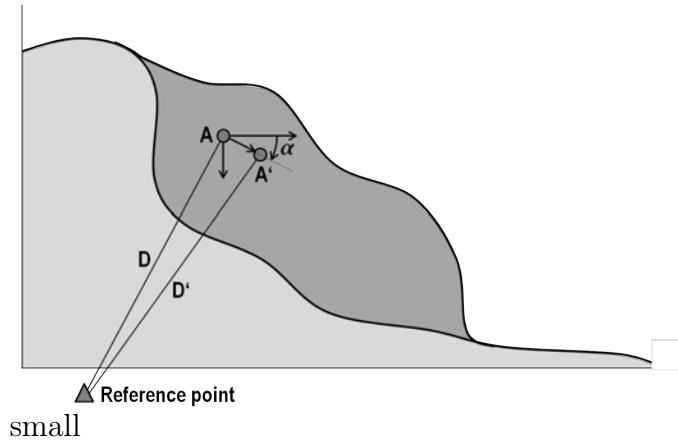


Figure 25: Criteria of ground movements  
[Sadarviana, 2006, p. 99]

### Kinematic model:

The kinematic model is considered as the deformation based on the velocity of movement. The equation for this model is formed by Taylor series (2.19). The input values are the coordinates of the observed points, the calculated velocity and the acceleration from the period  $(k - 1)$ . To get a prediction of coordinates, velocities and accelerations, also the standard deviations of these parameters for period  $k$ , the Kalman-filtering is a useful instrument. The precision of the prediction can be determined by the difference between the predicted and observed period  $k$ .

$$\mathbf{x}(t_k) = \mathbf{x}(t_{k-1}) + \Delta t * \dot{\mathbf{x}}(t_{k-1}) + \frac{1}{2} * \Delta t^2 * \ddot{\mathbf{x}}(t_{k-1}) + \dots \quad \text{with} \quad \Delta t = t_k - t_{k-1} \quad (2.19)$$

### Dynamic model:

The combination of geometric and physical parameters in respect to the time results in the dynamic model. The parameters are represented by coefficients like rainfall, gravity, porosity or saturation. The Kalman-filtering is used to solve this problem. In addition to the kinematic model it is possible to calculate the change of physical parameters.

## 2.6.2 Geodetic methods for mass movement monitoring

In Fig. 24 a lot of monitoring systems are listed. Number 13 to 20 (gray background) are geodetic methods for movement monitoring. These systems will be explained briefly.

### Satellite based systems

- GPS-measurements:  
To get 3D coordinates of a point  $P$ , a satellite receiver has to be installed at this point. The antenna has to observe signals of at least of four GPS satellites. The satellite data contain their ephemerides (actual satellite coordinates) with which it is possible to estimate the coordinates of point  $P$  (see section 2.4.1).
- Remote Sensing:  
This measurement system registers objects without any physical contact. Data capturing of the earth's surface is done by using electromagnetic sensors. The geometric features are not in the foreground of this measurement system [Kraus, 2004, p. 2].

## Airborne systems

- Airborne laser scanning:  
The laser beams leave the laser scanner perpendicular to the direction of flight and measure local polar coordinates of the surface. To get Cartesian coordinates it is important to know the position of the laser scanner and the angles in which the laser beams leave the laser scanner. Permanent GPS measurements and an *Inertial Measurement Unit (IMU)* are synchronised with the scanning process and save the position and scanning information in a time domain of microseconds during the flight [Kraus, 2004, p. 450].
- Remote Sensing:  
Remote Sensing (see satellite based systems) can be done by satellites, planes or terrestrial measurement devices (examples see in [Wieser, 2014, p. 205 - 206 and p. 257 - 267]).
- Aerial photo analysis:  
Photogrammetry measure geometric features of objects. The main tasks are to produce topographic and orthophoto maps [Kraus, 2004, p. 2].

## Terrestrial systems

- Levelling:  
Levelling is a measurement technique to determine height differences between two measuring points. The difference of two height values, which are readable on the measurement staffs, indicates the height difference of these two measurement points [Kahmen, 2006, p. 393].
- Laser distance measurement:  
Using measurement devices with EDM open the possibility to observe distances and relative movements without direct contact of an object. It depends on the accuracy, but it can be chosen between fixedly installed devices (higher accuracy) or mobile devices (mostly for non-reflector measurements) [Rapp, 2011, p. 393].
- Total station:  
With this terrestrial measurement method it is possible to measure absolute positions of measurement points (triangulation). The device observes distances with EDM and angles from a known position to an unknown point or the other way around [Kuntsche, 2000, p. 292].
- Terrestrial Laser Scanning (TLS):  
TLS is a young technology which does distance measurements without reflectors and two angle measurements. In contrast to the total station the TLS does not measure discrete points. The surrounding area is scanned in a fine grid and high velocity. The measurements are solved in a point cloud (see section 2.4.2).

### 2.6.3 Statistical significance test

Geometrical displacements are significant if the probability of a random movement is lower than a specific boundary value. There are several possibilities to prove significant movements. One of them would be the *t-Student distribution*. For this test it is necessary to calculate the coordinate differences ( $dE$ ,  $dN$ ,  $dh$ ) and their standard deviations ( $\sigma dE$ ,  $\sigma dN$ ,  $\sigma dh$ ) between two periods first (2.20).

$$\begin{aligned}
dE &= E_k - E_{k-1} & \sigma dE &= \sqrt{\sigma dE_k + \sigma dE_{k-1}} \\
dN &= N_k - N_{k-1} & \sigma dN &= \sqrt{\sigma dN_k + \sigma dN_{k-1}} \\
dh &= h_k - h_{k-1} & \sigma dh &= \sqrt{\sigma dh_k + \sigma dh_{k-1}}
\end{aligned} \tag{2.20}$$

Coordinate differences and their standard deviations

$$\delta d = \sqrt{dE^2 + dN^2 + dh^2} \quad \sigma \delta d = \sqrt{\frac{(dE * \sigma dE)^2 + (dN * \sigma dN)^2 + (dh * \sigma dh)^2}{\delta d}} \tag{2.21}$$

$\delta d$  ... movement distance  
 $\sigma \delta d$  ... standard deviation of the movement distance  $\delta d$

$$T = \frac{\delta d}{\sigma \delta d} \tag{2.22}$$

The t-Student distribution is necessary to check the null hypothesis (2.18). Therefore the test statistic  $T$  ((2.20) - (2.22)) is to compare with the appropriate realisation value  $t_{f,\alpha/2}$  (2.23). These quantiles of the t-Student distribution are listed in tables e.g. [Niemeier, 2008, p. 473]; [Gruber and Joeckel, 2011, p. 177].

$$|T| > t_{f,\alpha/2} \tag{2.23}$$

If true the geometrically displacement is significant.

$f$  ... variability  
 $\alpha/2$  ... significance level double sided

### 3 GNSS and TLS observation and data processing

For this research three measurement periods are implemented. The first period is done at the end of the rain season at 2-3 April 2013. Five months later in the dry season at 11-12 September 2013 the second period is made. The third and final period completes the measurements of this research at 13-14 December 2013. Every measurement period is realised by *Global Positioning System (GPS)* and *Terrestrial Laser Scanning (TLS)*.

#### 3.1 Description of GNSS and TLS campaigns

Ten measured points are chosen in the sliding area (N:  $-6^{\circ}43'00''$  to  $-6^{\circ}42'50''$ ; E:  $107^{\circ}00'00''$  to  $107^{\circ}00'10''$ ) in April during the first period. Beginning near the main street *Jalan Labuan - Cianjur* the points are located in north-south direction on the half way to the Cijember river valley (see Fig. 26). The measurement area is situated in the northern and middle part of the whole movement area (see Fig. 7 and 14).



(© Google Inc. - www.maps.google.at)

Figure 26: Observation points of the slope  
 BASE = reference station; CT01 - CT10 = observation points

### 3.1.1 Measured points

The aim of this master thesis is to get information about movements of the moving area by TLS. Movements detected by GPS only show local displacements of the mass movement. Pure measurements by GPS are done in other researches before, e.g. [Sadarviana, 2006]. In this research the GPS measurements are required to locate the TLS stations (see section 2.4.2 - Registration) and the modelling (see section 4). The movements which are established by GPS should correspond to the movement detected by the TLS stations. In this case the GPS measurements serve as a control of the TLS measurements. The absolute coordinates from GPS fix the TLS measurements on the earth's surface.

Concerning the sliding area the measurement points are chosen by good positioning of the TLS measurements (see Fig. 27b to Fig. 28h). This means that the positioning is chosen in such a way as to get as much information about the surface as possible, by as few positions of the TLS station as possible. Not every measured point is a good position for GPS measurements like CT04, CT06 and CT07 (nearby or under a tree, see Fig. 28b, 28e and 28f). Seven points are marked by metal tubes (see Fig. 28i) and wood sticks which are struck in soil. The point of the BASE station is a fixed cement block in soil, also points CT07 and CT09 (see Fig. 27a, 28e and 28g). CT01 (Fig. 27b) is chosen on a concrete wall.



Figure 27: Part 1 of the observation points

The sliding area serves as agricultural land and for inhabitants in the south of Bogor. This may be the reason why the points CT03, CT05 and CT10 are missing in the second measurement period (blue and orange points in Fig. 26). The BASE station is used for the GPS measurements (reference station) and the backside (orientated target mark) for the TLS measurements.





(a) CT03



(b) CT04



(c) CT05



(d) CT06



(e) CT07



(f) CT08



(g) CT09



(h) CT10



(i) Metal tube

Figure 28: Part 2 of the observation points

The points CT01, CT02 and CT03 (purple and orange points in Fig. 26) are lost between the second and third period. The construction works from the main road, which broke down after a heavy rainfall after the first period, goes on and the area around CT01 (see Fig. 27d) is renovated. The terrain at CT02 (see Fig. 27f) serves as a mound area for the construction works (see Fig. 27e – 27f). CT03 is missing again, perhaps due to farming.

### 3.1.2 Measurement devices

#### GPS-device: Topcon GR-3



Figure 29: Topcon GR-3

The GPS measurements are done with the *Topcon GR-3* GNSS device. This device is one of the first tools which observes all GNSS signals from GPS, GLONASS as well as Galileo. The receiver is a robust device in a compact body. It connects the functional system design with performance and accuracy [Topcon GR-3, 2007, retrieved: 14.07.2014].

Some technical facts:

- Tracking:**
- 72 universal channels
  - receive all signals from the 3 GNSS-technologies
  - using for WAAS and EGNOS possible
- Accuracy:**
- Post-Processing/static: - H:  $\pm 3\text{mm} + 0.5\text{ppm}$   
 - V:  $\pm 5\text{mm} + 0.5\text{ppm}$
- Communication:**
- radiocommunication
  - mobile radiocommunication (optional)
  - wireless
- Data and memory:**
- SD card up to 2 GB
  - sundry RTK-formats
  - optional, external array processor
- Environment:**
- body: aluminium housing
  - class of fall: survive being dropped from 2m without damage
  - duration: basic station 11h, rover 13h

### TLS-device: Leica ScanStation C10

The *Leica ScanStation C10* is an all-in-one scanner. It is a compact, surveyor-friendly device which gives users the advantage of long-range scanning, fast and full-dome interior scanning with high accuracy. The scan station can be used for built-, topographic- and mapping surveys [Leica ScanStation C10, 2011, retrieved: 14.07.2014].



Figure 30: Leica ScanStation C10

#### Benefits:

Lower cost  
Faster  
Safer  
Less intrusive  
More informative  
More accurate & complete

#### Applications:

Design & engineering  
Construction & fabrication QA  
Asset management & archive  
Forensics & security planning  
Marketing proposals  
Research & education

Some technical facts:

#### General:

Instrument type: Compact, pulsed, very high speed laser scanner, with survey-grade accuracy, range, and Field of View (FoV)  
User interface: Onboard control  
Camera: Digital camera with zoom video

#### System Performance:

Accuracy: - Position (1m – 50m range): 6mm (one sigma)  
- Distance (1m – 50m range): 4mm (one sigma)  
- Angle (horizontal/vertical):  $60\mu\text{rad}/60\mu\text{rad}$  (12"/12")  
- Target acquisition: 2mm standard deviation

#### Laser Scanning System:

Range: 300m (minimum range 0.1m)  
Scan rate: Up to 50.000 points/s  
Scan resolution: Point size: 4.5mm (from 0 – 50m)  
FoV: - Horizontal: 360° (maximum)  
- Vertical: 270° (maximum)  
- Aiming/Sighting: Parallax-free, integrated zoom video  
Scanning optics: Vertically rotating mirror on horizontally rotating base  
Data storage: - 80GB SSD  
- external USB device  
Communication: - Dynamic Internet Protocol (IP) Address  
- Ethernet or wireless LAN

**Electrical:**

Battery type: Internal: 2x Li-Ion, External: Li-Ion  
 Duration: Internal: > 3.5h (2 batteries), External: > 6h (room temp.)

**Control Options:**

Full color touch screen  
 Remote controller

**3.1.3 Measurements**

In each period every viewpoint in which the TLS scanned the surroundings is measured by GPS. The GPS technique is performed by *Precise DGPS* (see section 2.4.1 - Evaluation process) using three to four Topcon GR-3 GNSS receivers. One Leica ScanStation C10 (TLS-station) is used for scanning.

**GPS-measurements**

One of the GPS receivers is installed as the reference station called *BASE* (see Fig. 27a). This station observes all signals from the visible GPS satellites during the period. The other GPS receivers are located at each measured point. The observation time for each point is between 1h and 4h. The measurement time depends on the visibility of the GPS satellites. The coordinates are calculated in baseline-mode from the IGS stations to the BASE station and subsequently with fixed BASE station coordinates from the BASE station to the measured points (see 3.2.1).

**TLS-measurements**

The TLS device is positioned at every measured point. In a temporal resolution of about half an hour the TLS scans the surrounding area in a fine-grained mode. The device takes pictures around the area which make the data post-processing easier. To nexus each separate scanned terrain it is necessary to work with target marks (see Fig. 31). For the scans, at least three reflectors are necessary which are also used by other scans (see 2.4.2 - Registration).



Figure 31: Reflectors

**3.2 Data processing**

The data processing was carried out in post processing. It is independent of the type of measurement. The software *Bernese GNSS Software V5.0* established by the *Astronomical*

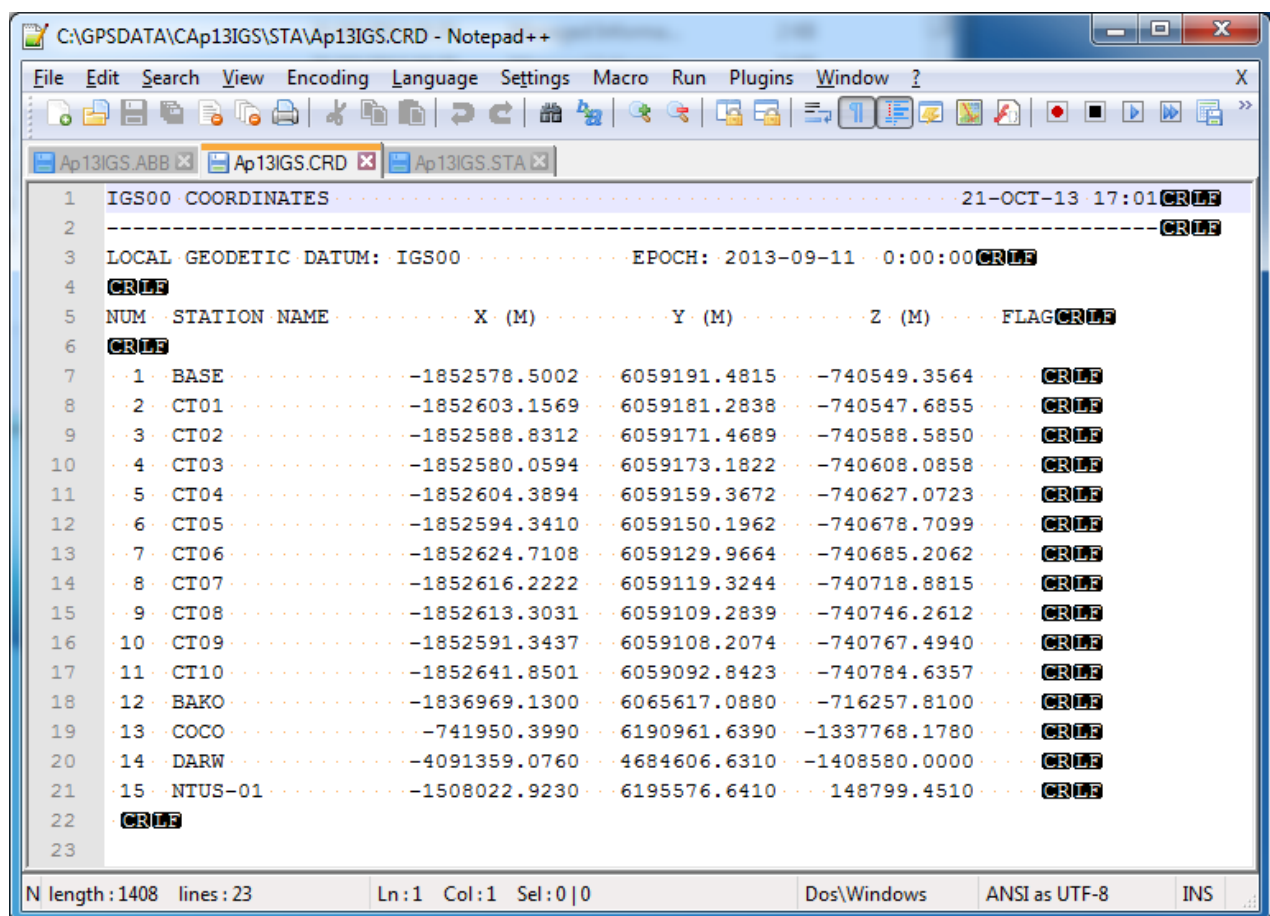
Institute of the University of Bern (AIUB) has to utilised. For the TLS data processing the program *Cyclone 8.0*, a software of the company of *Leica Geosystems*, and the freeware *CloudCompare (CC)*<sup>3</sup> were used.

### 3.2.1 Data processing of GPS by Bernese

The Bernese GPS Software is a scientific, high-precision, GNSS data processing software [AIUB, 2013, retrieved: 26.11.2013]. Before the data processing is started, some files have to be created manually:

- A priori point coordinates (.CRD-file, Fig. 32).
- Abbreviation file (.ABB-file, Fig. 33).
- Station name file (.STA-file, Fig. 34).

The necessary information to fill the files can be found in the *Receiver Independent Exchange Format (RINEX)* files from the GPS data. For the estimation of the coordinates in Bernese it is advisable to use *Precise Point Positioning (PPP)* coordinates as a priori information in the coordinate file (see Fig. 32) instead of the coordinates from the raw data (RINEX files). PPP coordinates can be requested for example from the *Geodetic Reference Systems by the Natural Resources Canada*<sup>4</sup> PPP server.



```

1 IGS00 COORDINATES ..... 21-OCT-13 17:01 CRLE
2 ..... CRLE
3 LOCAL GEODETIC DATUM: IGS00 ..... EPOCH: 2013-09-11 0:00:00 CRLE
4 CRLE
5 NUM STATION NAME ..... X (M) ..... Y (M) ..... Z (M) ..... FLAG CRLE
6 CRLE
7 1 BASE .....-1852578.5002 ..... 6059191.4815 .....-740549.3564 ..... CRLE
8 2 CT01 .....-1852603.1569 ..... 6059181.2838 .....-740547.6855 ..... CRLE
9 3 CT02 .....-1852588.8312 ..... 6059171.4689 .....-740588.5850 ..... CRLE
10 4 CT03 .....-1852580.0594 ..... 6059173.1822 .....-740608.0858 ..... CRLE
11 5 CT04 .....-1852604.3894 ..... 6059159.3672 .....-740627.0723 ..... CRLE
12 6 CT05 .....-1852594.3410 ..... 6059150.1962 .....-740678.7099 ..... CRLE
13 7 CT06 .....-1852624.7108 ..... 6059129.9664 .....-740685.2062 ..... CRLE
14 8 CT07 .....-1852616.2222 ..... 6059119.3244 .....-740718.8815 ..... CRLE
15 9 CT08 .....-1852613.3031 ..... 6059109.2839 .....-740746.2612 ..... CRLE
16 10 CT09 .....-1852591.3437 ..... 6059108.2074 .....-740767.4940 ..... CRLE
17 11 CT10 .....-1852641.8501 ..... 6059092.8423 .....-740784.6357 ..... CRLE
18 12 BAKO .....-1836969.1300 ..... 6065617.0880 .....-716257.8100 ..... CRLE
19 13 COCO .....-741950.3990 ..... 6190961.6390 .....-1337768.1780 ..... CRLE
20 14 DARW .....-4091359.0760 ..... 4684606.6310 .....-1408580.0000 ..... CRLE
21 15 NTUS-01 .....-1508022.9230 ..... 6195576.6410 ..... 148799.4510 ..... CRLE
22 CRLE
23

```

N length: 1408 lines: 23 Ln: 1 Col: 1 Sel: 0|0 Dos\Windows ANSI as UTF-8 INS

Figure 32: Coordinate file

<sup>3</sup><http://www.danielgm.net/cc/>

<sup>4</sup><http://webapp.geod.nrcan.gc.ca/geod/>

For data processing the station coordinates from the stations *Cibinong (BAKO)*, *Cocos Island (COCO)*, *Darwin (DARW)* and *Singapore (NTUS)* (see Tab. 5) were constrained to their official ITRF08 values. The RINEX data of these stations is available for download, for example at the homepage of the *University of California - San Diego (UCSD)*<sup>5</sup>.

station	name (country)	distance from BASE	located in
BAKO	Cibinong (Indonesia)	~ 30km	north-west
COCO	Coco Islands (Costa Rica)	~ 1.250km	south-west
DARW	Darwin (Australia)	~ 2.700km	south-east
NTUS	Singapore (Singapore)	~ 950km	north-west

Table 5: IGS stations  
compare with Fig. 35

The coordinates which are used for the data processing (see Fig. 32) are geocentric coordinates (see section 2.5.1). Fig. 32 to Fig. 34 show the text files of the coordinates, stations and abbreviations of the first measurement period in April 2013.

```

1 PPP_021440 ..... 21-OCT-13 17:50 CRLE
2 ----- CRLE
3 CRLE
4 Station name ..... 4-ID ..... 2-ID ..... Remark ..... CRLE
5 ***** **** ** ***** CRLE
6 BASE ..... BASE ..... BA ..... Added by SR updabb ..... CRLE
7 CT01C ..... CT01 ..... CT ..... Added by SR updabb ..... CRLE
8 CT02C ..... CT02 ..... CT ..... Added by SR updabb ..... CRLE
9 CT03C ..... CT03 ..... CT ..... Added by SR updabb ..... CRLE
10 CT04C ..... CT04 ..... CT ..... Added by SR updabb ..... CRLE
11 CT05C ..... CT05 ..... CT ..... Added by SR updabb ..... CRLE
12 CT06C ..... CT06 ..... CT ..... Added by SR updabb ..... CRLE
13 CT07C ..... CT07 ..... CT ..... Added by SR updabb ..... CRLE
14 CT08C ..... CT08 ..... CT ..... Added by SR updabb ..... CRLE
15 CT09C ..... CT09 ..... CT ..... Added by SR updabb ..... CRLE
16 CT10C ..... CT10 ..... CT ..... Added by SR updabb ..... CRLE
17 BAKO ..... BAKO ..... BA ..... Added by SR updabb ..... CRLE
18 COCO ..... COCO ..... CO ..... Added by SR updabb ..... CRLE
19 DARW ..... DARW ..... DA ..... Added by SR updabb ..... CRLE
20 NTUS-01 ..... NTUS ..... NT ..... Added by SR updabb ..... CRLE
21

```

Figure 33: Abbreviation file

The ephemerides and ionosphere models for the respective periods can be downloaded from the IGS-homepage<sup>6</sup> or the AIUB-homepage<sup>7</sup>.

<sup>5</sup><http://garner.ucsd.edu/>

<sup>6</sup><http://igsceb.jpl.nasa.gov/>

<sup>7</sup><http://www.bernese.unibe.ch/>

STATION NAME	FLG	FROM	TO	RECEIVER TYPE	ANTENNA TYPE	ARC #	ANT #	NORTH	EAST	UP	DESCRIPTION	REMARKS
BASE	***	YYYY MM DD HH MM SS	YYYY MM DD HH MM SS	*****	*****	*****	*****	*****	*****	*****	*****	*****
CT01C	001	1980 01 06 00 00 00	2099 12 31 00 00 00	TOPCON	TFS_GR3	NONE	000000	000000	0.0000	0.0000	1.8290	
CT02C	001	1980 01 06 00 00 00	2099 12 31 00 00 00	TOPCON	TFS_GR3	NONE	000000	000000	0.0000	0.0000	1.6460	
CT03C	001	1980 01 06 00 00 00	2099 12 31 00 00 00	TOPCON	TFS_GR3	NONE	000000	000000	0.0000	0.0000	1.4670	
CT04C	001	1980 01 06 00 00 00	2099 12 31 00 00 00	TOPCON	TFS_GR3	NONE	000000	000000	0.0000	0.0000	1.6180	
CT05C	001	1980 01 06 00 00 00	2099 12 31 00 00 00	TOPCON	TFS_GR3	NONE	000000	000000	0.0000	0.0000	1.3340	
CT06C	001	1980 01 06 00 00 00	2099 12 31 00 00 00	TOPCON	TFS_GR3	NONE	000000	000000	0.0000	0.0000	1.5742	
CT07C	001	1980 01 06 00 00 00	2099 12 31 00 00 00	TOPCON	TFS_GR3	NONE	000000	000000	0.0000	0.0000	1.7690	
CT08C	001	1980 01 06 00 00 00	2099 12 31 00 00 00	TOPCON	TFS_GR3	NONE	000000	000000	0.0000	0.0000	1.4170	
CT09C	001	1980 01 06 00 00 00	2099 12 31 00 00 00	TOPCON	TFS_GR3	NONE	000000	000000	0.0000	0.0000	1.3230	
CT10C	001	1980 01 06 00 00 00	2099 12 31 00 00 00	TOPCON	TFS_GR3	NONE	000000	000000	0.0000	0.0000	1.8760	
BAKO	001	1980 01 06 00 00 00	2099 12 31 00 00 00	LEICA GRX12000PRO	LEIAT50400	LEI5	351638	200046	0.0000	0.0000	1.6980	
COCO	001	1980 01 06 00 00 00	2099 12 31 00 00 00	TRIMBLE NETRS	ACAD/R_T	NONE	000000	000002	0.0000	0.0000	0.0040	
DAMM	001	1980 01 06 00 00 00	2099 12 31 00 00 00	LEICA GRX12000PRO	ASPT00934ED_M	NONE	355503	000000	0.0000	0.0000	0.0025	
NTUS-01	001	1980 01 06 00 00 00	2099 12 31 00 00 00	LEICA GRX12000PRO	LEIAT50400	NONE	352729	200240	0.0000	0.0000	0.0776	

Figure 34: Station file

The data processing in Bernese is performed in two steps for each period. The first step is to estimate the reference station (BASE) coordinates. To find the best result, different IGS stations and their combinations are used (see Tab. 5 and Fig. 35). The best results with the smallest  $\sigma$ -errors are achieved by using the IGS station BAKO (see section 3.3.1).



(© Google Inc. - www.maps.google.at)

Figure 35: GPS data processing of BASE station  
 BASE = reference station; CT01 - CT10 = observation points

With the fixed coordinates from the BASE station it is possible to estimate the coordinates of the measurement points CT01 to CT10 with respect to the BASE station(see Fig. 35).

### GNSS data processing in Bernese

At first, it is necessary to import the RINEX observation files and transform them into a Bernese (binary) format. With information about the measurement time, the ionosphere and the ephemerides, it is possible to generate the following files:

- *Pole Information*-files.
- *Tabular Orbit*-files.
- *Bernese Standard Orbit*-files.

The data processing part I includes three steps:

- *Receiver Clock Synchronisation*.
- Form *Baselines*.
- Preprocessing of the *Phase Baseline*-files (against cycle-slips).

In step two, the baselines from the fixed BASE-station to each measurement point are formed.

The data processing part II in Bernese includes the following steps:

- *Least-Square Adjustment* for the *First Solution*.
- And last, the *Ambiguity Resolution QIF*.

In the first solution step, a ionosphere-free solution is created with unresolved ambiguities. In the last step, the ambiguities are resolved using the *Quasi-Ionosphere-Free (QIF)* strategy. The coordinates in this file are the final geocentric coordinates (see section 2.5.1) in the first step for the BASE station and in the second step for the measurement points CT01 to CT10. For a detailed description of data processing see the Bernese manual [Dach et al., 2007].

For a better illustration, the geocentric coordinates are transformed into UTM-coordinates (see 2.5.2). The sliding area is located on the west side of UTM zone 48S, around 6°42' south of the equator.

#### 3.2.2 Data processing of TLS by Cyclone and CloudCompare (CC)

Different steps are done to get a solution of the TLS data. The first steps are done using the program *Cyclone 8.0* (nexus of single clouds and filtering), for the latter part *CloudCompare V2* (georeferencing and cloud compare) is used.



## Steps in Cyclone

### Nexus of single scans:

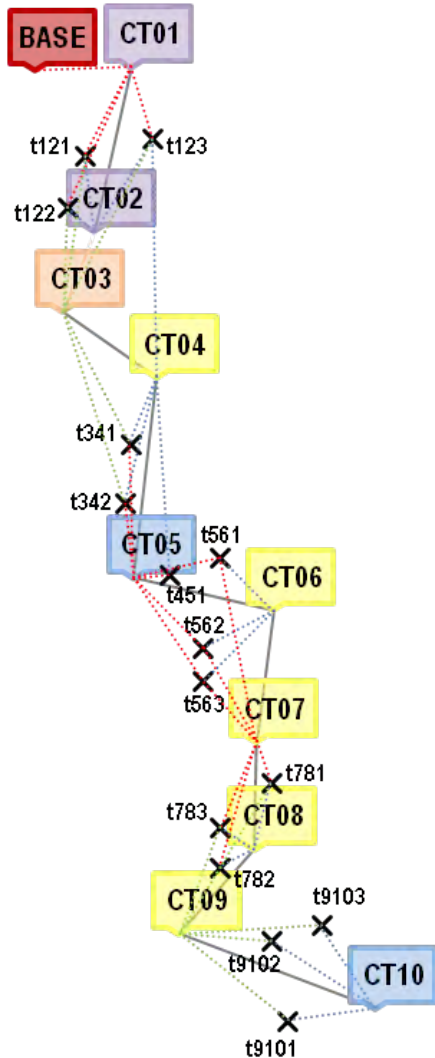


Figure 36: Targets of the TLS clouds

The raw data of the Leica ScanStation C10 of each period is imported into the program Cyclone 8.0. Ten scans are done for every period. These scans have to be combined. All stations from one measurement period are selected and merged by the target marks (tie points - see section 2.4.2 - Registration). The program calculates the accuracy for the nexus and marks bad tie points which can be excluded. The averaged accuracy of each used target mark is calculated by

- April: 0.002m,
- September: 0.002m and
- December: 0.003m

and corresponds to the declaration of the manufacturer. To get this result some single scans have to be excluded in each period:

- April: CT10 is missing
- September: CT01 is missing
- December: CT01, CT02 are missing

For each cloud three tie points are measured to link these clouds. CT10 (April) and CT02 (December) are missing because of bad target measurements. The scan of CT01 (September and December) do not include information about the scan (point cloud), but it is possible to merge all view-points including the backside reflector. This special reflector is constructed to the known coordinate position of the GPS reference station (BASE) and is scanned by the first single scan on position CT01. As the height of this reflector is measured, 3D coordinates from that reflector are known. This is important to know because the comparison of the point clouds will occur by this reference or backside point.

The non-existent measurement information of some single scans do not present problems for the research, because the examined area is located between the stations CT01 and CT10. The missing cloud of CT02 in the December data do not create problems, too, because the single scan of CT03 is linked to the tie points of station CT01.

### Accuracy of the nexus:

The nexus of point clouds is made on different procedures. The target-to-target procedure (nexus of point clouds by 2D target marks) is carried out by the program Cyclone. In the following, an accuracy estimation by means of the error propagation in the course of the *bundle block adjustment* is made (see section 2.4.2 - Estimation of the accuracy).

An self-created MATLAB file calculates the accuracy of the target marks and the observation points in detail. Input variables are the measured values of the tie points. Starting with orientated observation and fixed coordinates of point CT01, together with the information of the measurement accuracy, the bundle block adjustment calculates the orientation and coordinates of the other observation points with their accuracies. The accuracies about the second period (September) are listed in Tab. 6 and visualised in Fig. 37, 38 and 46.

Targets	x[m]	y[m]	z[m]	xyz[m]	POS	X[m]	Y[m]	Z[m]	XYZ[m]
T01	0.0005	0.0007	0.0001	0.0009	CT01	0.0000	0.0000	0.0000	0.0000
T02	0.0003	0.0007	0.0002	0.0008	CT02	0.0006	0.0007	0.0008	0.0012
T03	0.0004	0.0007	0.0003	0.0008	CT03	0.0011	0.0009	0.0018	0.0022
T04	0.0024	0.0010	0.0051	0.0057	CT04	0.0017	0.0009	0.0038	0.0043
T05	0.0029	0.0012	0.0061	0.0069	CT05	0.0033	0.0013	0.0069	0.0078
T06	0.0031	0.0020	0.0092	0.0100	CT06	0.0038	0.0028	0.0115	0.0125
T07	0.0033	0.0016	0.0076	0.0084	CT07	0.0049	0.0029	0.0133	0.0145
T08	0.0040	0.0022	0.0104	0.0113	CT08	0.0061	0.0034	0.0153	0.0168
T09	0.0046	0.0026	0.0115	0.0127	CT09	0.0071	0.0032	0.0144	0.0164
T10	0.0056	0.0038	0.0162	0.0175	CT10	0.0082	0.0056	0.0239	0.0259
T11	0.0059	0.0031	0.0142	0.0157					
T12	0.0064	0.0031	0.0145	0.0161					
T13	0.0070	0.0047	0.0205	0.0222					
T14	0.0073	0.0038	0.0181	0.0199					
T15	0.0085	0.0039	0.0199	0.0220					

Table 6: Accuracies of the viewpoints and targets after the nexus of period 2

Targets	CT01	CT02	CT03	CT04	CT05	CT06	CT07	CT08	CT09	CT10
T01	1	2	3	4						
T02	1	2	3							
T03	1	2	3							
T04			3	4	5					
T05			3	4	5					
T06					5	6	7			
T07				4	5					
T08					5	6	7			
T09					5	6	7			
T10							7	8	9	
T11							7	8	9	
T12							7	8	9	
T13									9	10
T14									9	10
T15									9	10

Table 7: Viewpoints and their measured target marks for all periods

Based on the measurement accuracy of the target marks, a 3D point position error of  $< 2.6\text{cm}$  at the last viewpoint CT10 is achievable. The accuracies between the observation points are irregular because the observation points not always measured target marks of the previous observation points. In Tab. 7 it is shown which viewpoints (CT01 - CT10) are linked to which target marks (T01 -T15).

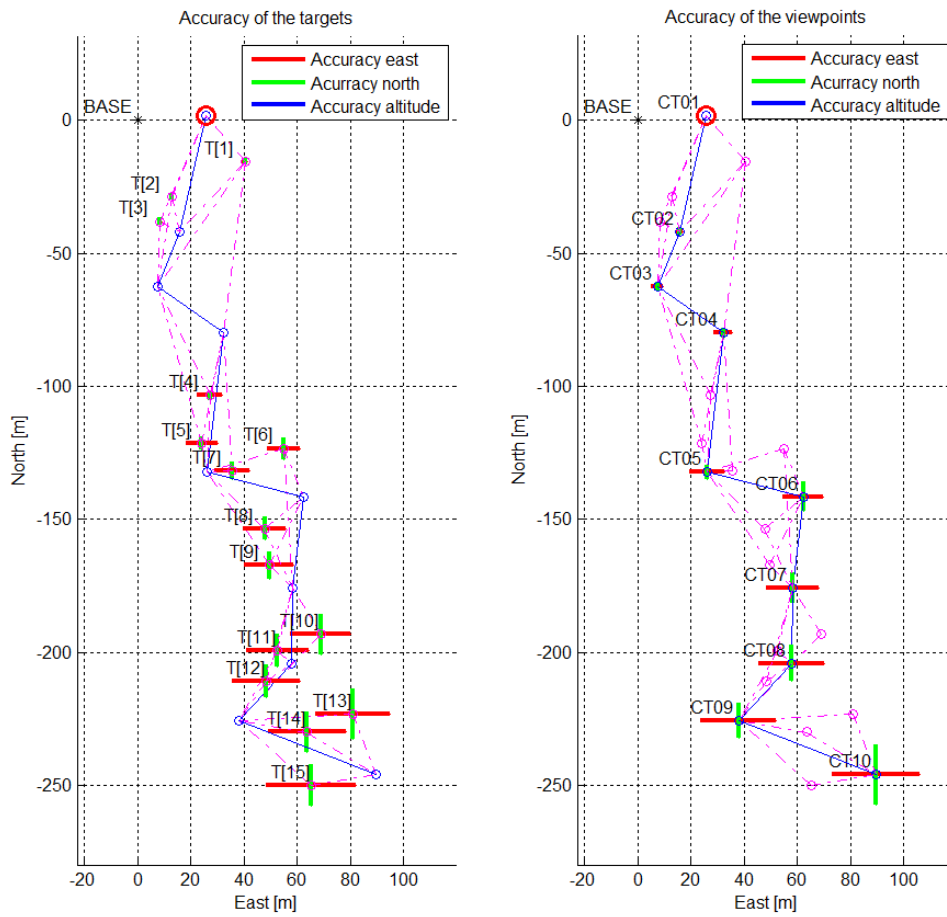


Figure 37: Accuracy of the horizontal position of period 2

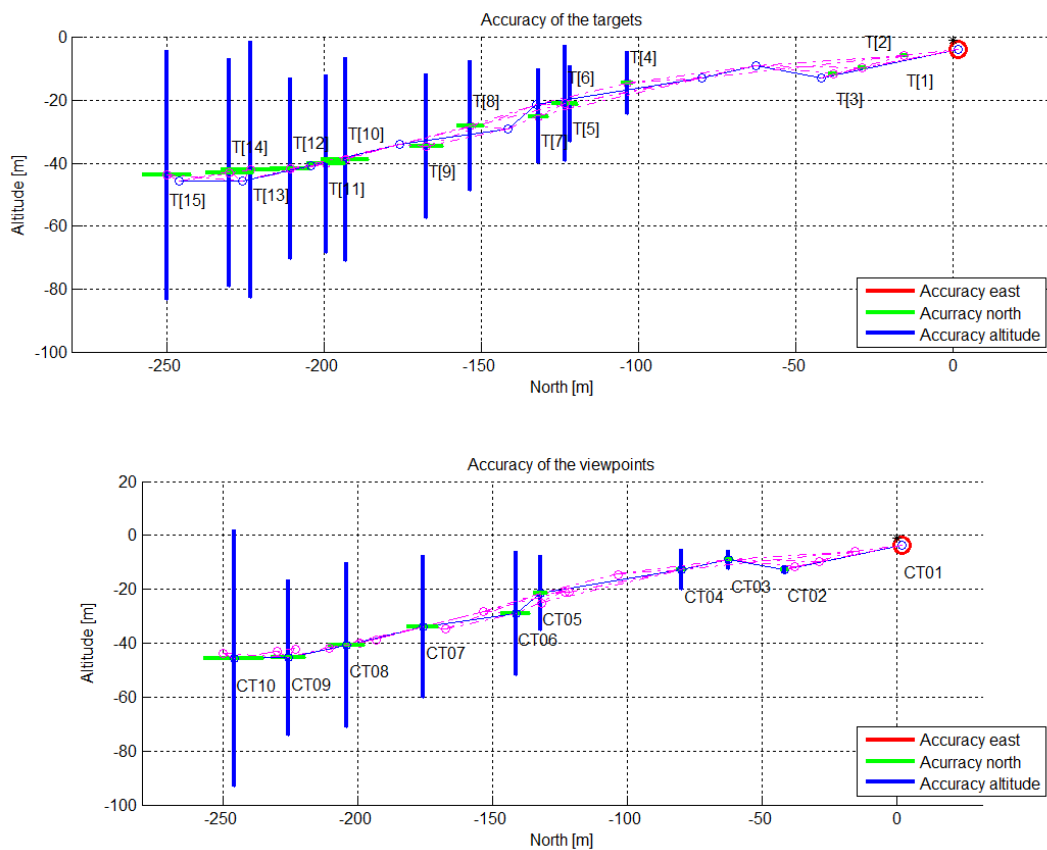


Figure 38: Accuracy of the vertical position of period 2

The graphics in Fig. 37 and 38 show the accuracy of the target marks and the observation points in the three directions  $X$ ,  $Y$  and  $Z$  of the measurement period in September. The values of the directions and the 3D point position errors are listed in Tab. 6. It is striking that the accuracy in the altitude is three to five times more inexact than in horizontal direction. It was only possible to distribute the target marks in the horizontal plane. The bad distribution of the tie points in the vertical plane is the reason for the worse accuracy in vertical direction.

### Filtering:

Greater time was needed in post-processing to filter the scan data. Trees, grass and buildings are not part of the surface and have to be deleted. The filtering is done manually. Therefore pictures (see Fig. 39) made by the scanner are helpful.

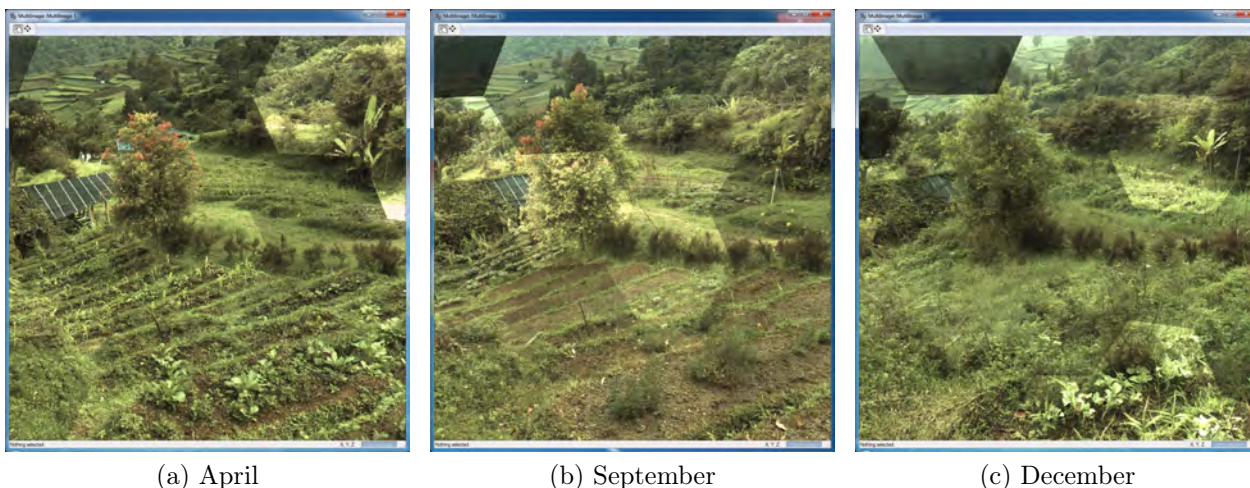


Figure 39: Vegetation by CT04 in south-west direction

The main problem within the filtering is to detect the surface. In the pictures of Fig. 39 it is obvious that the vegetation is abundant. The surface looks hilly and edged. It is difficult and needs a long time to delete the unnecessary information above the surface in the point clouds.

### Alignment of the point clouds:

POS	Period 1			Period 2			Period 3		
	X[m]	Y[m]	Z[m]	X[m]	Y[m]	Z[m]	X[m]	Y[m]	Z[m]
Backside	0.000	0.000	0.000	0.000	0.000	0.000	0.000	0.000	0.000
CT01	25.597	1.616	-3.612	25.595	1.613	-3.605	26.651	5.228	-3.504
CT02	15.792	-41.783	-12.590	15.812	-41.797	-12.570	—	—	—
CT03	7.431	-62.547	-8.644	7.451	-62.578	-8.850	7.939	-62.810	-8.883
CT04	32.013	-79.891	-12.597	32.082	-79.916	-12.632	32.110	-79.932	-12.628
CT05	26.128	-132.355	-21.151	26.120	-132.350	-21.216	26.125	-132.348	-21.209
CT06	62.216	-141.378	-28.888	62.203	-141.550	-28.804	62.204	-141.606	-28.801
CT07	58.112	-175.638	-33.784	58.161	-175.828	-33.697	58.185	-175.876	-33.705
CT08	57.819	-203.985	-40.635	57.791	-204.136	-40.567	57.795	-204.173	-40.580
CT09	37.952	-225.756	-45.414	37.895	-225.779	-45.284	37.890	-225.771	-45.289
CT10	—	—	—	89.596	-245.986	-45.533	89.586	-246.003	-45.532

Table 8: Roughly georeferenced TLS coordinates

The next step is to orientate the clouds of each period closely to the GPS coordinates. The transformation of the point clouds into the GPS coordinate system runs easier after a rough before-orientation. The clouds are measured in a local coordinate system. The backside (position of the reflector on the GPS reference station) has the coordinates  $X = 0$ ,  $Y = 0$  and  $Z = 0$  in all three periods. As the TLS software has problems orientating the point clouds to the absolute GPS coordinates (software error), reduced GPS coordinates are used (see Tab. 13). Now it is only necessary to rotate the clouds into a close position to the GPS coordinates. The current results are roughly georeferenced point clouds (see Tab. 8). The fine alignment (georeferencing) is done in the following steps.

### Steps in CloudCompare (CC)

CC is an application which can map and compare 3D point clouds. It is used for the fine alignment of the roughly georeferenced clouds and the comparison of the point clouds of the three periods.

#### Subsampling:

*Subsampling* is a method to reduce the amount of data points in the point clouds. The Leica ScanStation C10 (see section 3.1.2) scanned the areas around their viewpoints in a fine-grained way (distances between the measurement points are submillimetre). The high resolution was necessary to collect as much as possible information about the surface because the terrain was densely vegetated. A lot of points were deleted by the filtering. For the modelling of the surface a resolution of 5cm between the measurement points in the point clouds is sufficient. The subsampling reduces the density of data points by about 96%.

#### Georeferencing:

In this step the point clouds are aligned as well as possible to the GPS solution. The coordinates of the roughly georeferenced TLS (see Tab. 8) are georeferenced to the reduced GPS coordinate system (see Tab. 13) which confirmed the superior coordinate system (see section 2.4.2 - Georeferencing).

POS	Period 1	Period 2	Period 3
BASE	ok	ok	ok
CT01	ok	ok	ok
CT02	not used	ok	not used
CT03	ok	ok	ok
CT04	not used	ok	ok
CT05	ok	ok	ok
CT06	not used	ok	ok
CT07	ok	ok	ok
CT08	ok	ok	ok
CT09	ok	ok	ok
CT10	not used	ok	ok

Table 9: Used tie points for the georeferencing

The 3D *Helmert*<sup>8</sup>-*Transformation*, based on the *Gauß-Helmert* model (see in [Niemeier, 2008, p. 346-350]), is the instrument used for georeferencing. The scale was not considered here and fixed to scale  $s = 1$ . The translational and the rotational parameters remain to be estimated

<sup>8</sup>Friedrich Robert Helmert (\*1843 - †1917), German geodesist and mathematician

(see in [Niemeier, 2008, p. 351-360]).

Each period covers eleven viewpoints of TLS (including the backside measurement of the GPS reference station) and GPS (including the BASE station). The latter are used as tie for the georeferencing (see list in Tab. 9).

Without using the points CT02, CT04, CT06 and CT10 in period 1 (April), and point CT02 in period 3 (December) for the parameter estimation in each period, the transformation delivers the best possible solution (smallest misclosures after the transformation - see Tab. 15) for the April-data. A second MATLAB-file prepared for the transformation calculates the following information for each period.

- The three rotational and translational parameters and their accuracy (see Tab. 10).
- The 3x3 rotation matrix.
- The 4x4 matrix (see Tab. 11) for the transformation in CC.
- The covariance matrix  $\Sigma_{xx}$  for the *covariance error propagation*.

	Period 1		Period 2		Period 3	
	Parameters	Accuracy $\sigma$	Parameters	Accuracy $\sigma$	Parameters	Accuracy $\sigma$
$X_0$ [m]	0.019	0.018	-0.011	0.008	0.002	0.006
$Y_0$ [m]	-0.013	0.012	-0.004	0.005	-0.002	0.004
$Z_0$ [m]	-0.064	0.020	-0.197	0.008	-0.254	0.006
$\omega$ [°]	0.037	0.012	0.004	0.005	0.008	0.004
$\phi$ [°]	-0.090	0.048	-0.011	0.018	-0.006	0.012
$\kappa$ [°]	-0.005	0.012	-0.002	0.004	-0.002	0.003

Table 10: Estimation of the parameters for the georeferencing and their accuracy

In Tab. 10 it is discernible that the parameters for the georeferencing are small but the values in direction  $Z$  are significant.

4x4 R-matrix period 1				4x4 R-matrix period 2			
3x3 R-matrix [rad]			T [m]	3x3 R-matrix [rad]			T [m]
0.999998	-0.000087	0.001576	0.0188	0.999999	-0.000029	0.000197	-0.0107
0.000086	0.999999	0.000642	-0.0133	0.000029	0.999999	0.000065	-0.0035
-0.001576	-0.000642	0.999998	-0.0644	-0.000197	-0.000065	0.999999	-0.1969
0.000000	0.000000	0.000000	1.0000	0.000000	0.000000	0.000000	1.0000

4x4 R-matrix period 3			
3x3 R-matrix [rad]			T [m]
0.999999	-0.000031	0.000101	0.0016
0.000031	0.999999	0.000138	-0.0015
-0.000101	-0.000138	0.999999	-0.2545
0.000000	0.000000	0.000000	1.0000

Table 11: Matrices composed of rotation matrix and translation vector

**Triangulation:**

It is more easy to compare gridded information instead of point clouds because the mesh is a plane which represents the surface. The point clouds are given in 3D coordinates. The function *axis aligned plain* in CC calculates a mesh on a 2.5-dimensional plane. Therefore CC estimates that the altitudes are carried by the principal  $Z$ -axis [Girardeau-Montaut, 2012, p. 27]. On the  $XY$ -plane the points are projected.

**Smoothing:**

On small test areas the results of the triangulations are seen (white planes in Fig. 40b and 41b). The surface looks like a rough and edged plane. The filtering of the raw data was a difficult task and not all points, not belonging to the surface, were deleted (red dots in this two pictures). This is the reason why the triangulation generates a rougher surface.

In CC the mesh can be smoothed by the *Laplace*<sup>9</sup>-filter. For the filtering different properties are tested. It is possible to choose the values for iterations and the smoothing factors. Fig. 40c to 40f and 41c to 41f show different equalisation by a fixed smoothing factor of 0.2 and different values of iterations.

On one side distinctive things like the stairs on the right side in Fig. 41a are discernible in the smoothed pictures at a lower value of iterations. An increasing value of iterations blur the stairs more and more. Otherwise the peaks which are generated by the triangulation with non-filtered points from the point clouds are smoothed more and more by a higher value of iterations.

We now need to assess the values that give the best approximation of the surface. In comparison of additional testing areas the best value of iteration is 30 by a smoothing factor of 0.2.

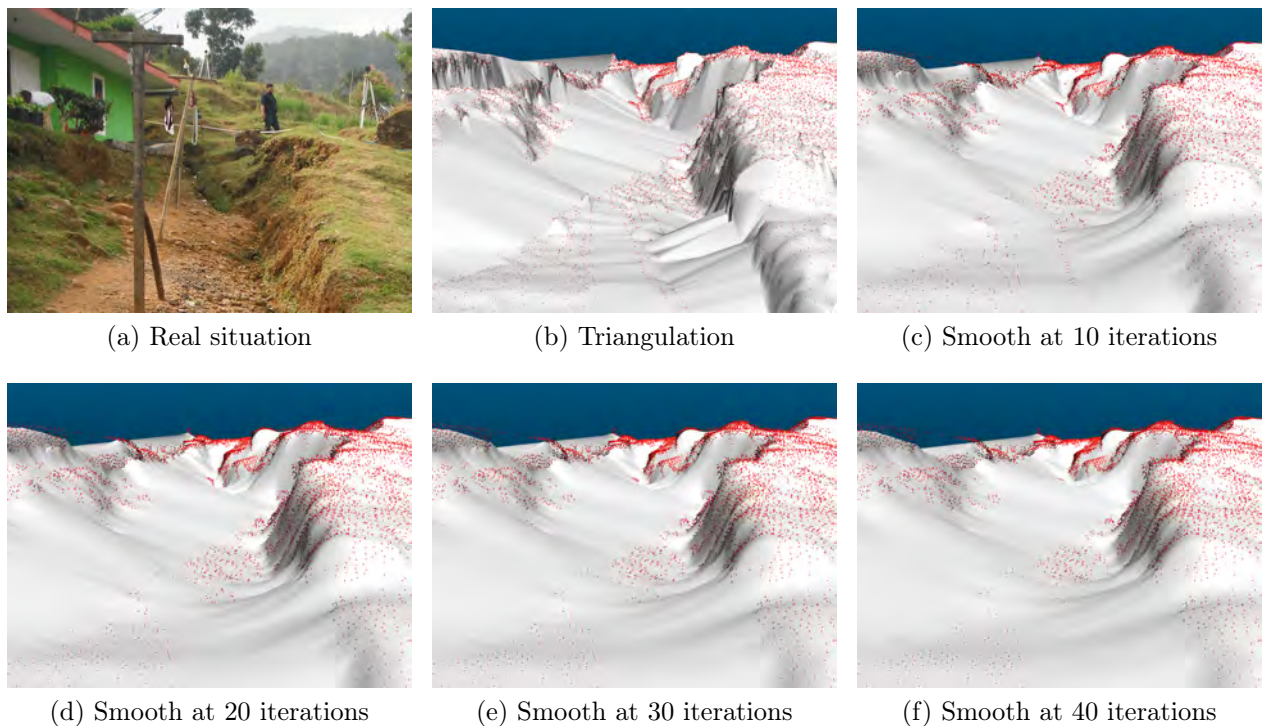


Figure 40: Different smooth factors situation 1

<sup>9</sup>Pierre-Simon Laplace, \*1749 - †1827, French mathematician, physicist and astronomer

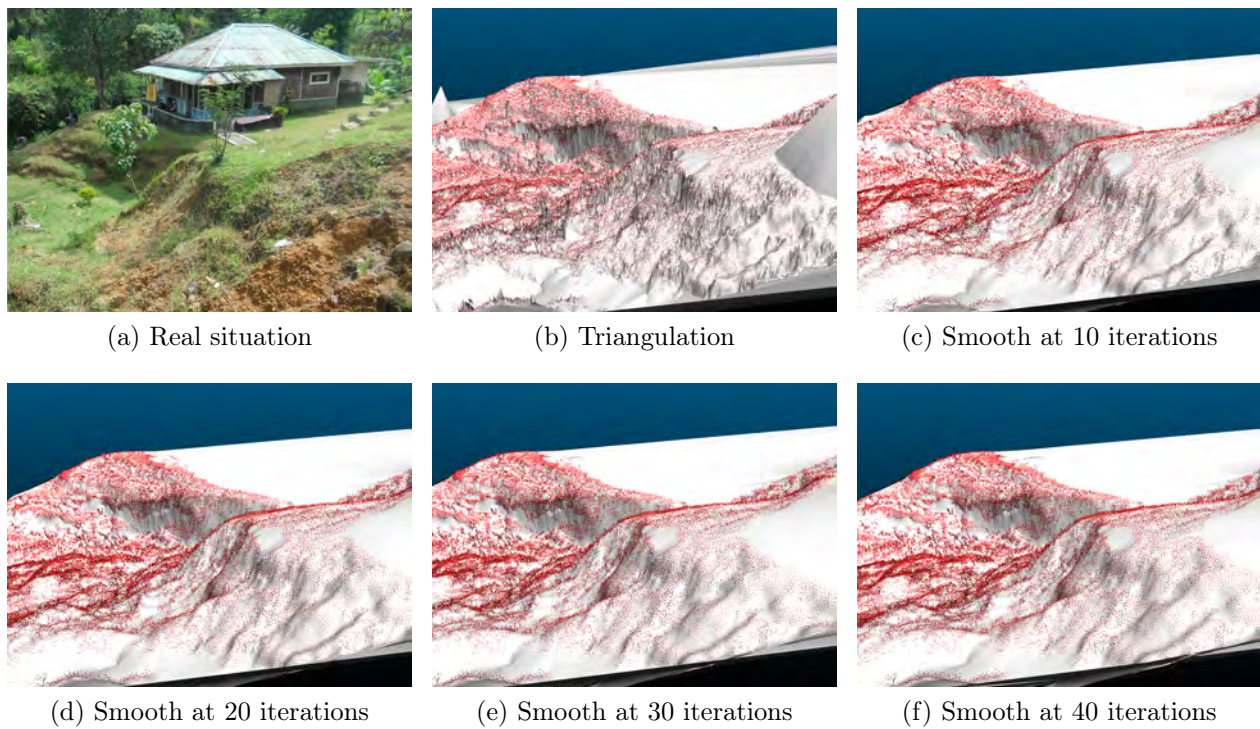


Figure 41: Different smooth factors situation 2

### Cloud compare:

In CC the *Plugin M3C2*<sup>10</sup> is a helpful tool for comparing the point clouds of each measurement period. With this tool it is easy to compare point clouds in different directions e.g. the directions of the three axes  $X$ ,  $Y$  and  $Z$ . The solution is a new scalar field where the differences of the two clouds are displayed in signed distances (see the description of the Plugin<sup>10</sup>).

## 3.3 Results of data processing

In section 3.2.1 and 3.2.2 the data processing of GPS and TLS was described. The data processing of TLS is based on the results of GPS. In the following steps the solutions of GPS and TPS are discussed.

### 3.3.1 GPS results

As already mentioned at the end of section 3.2.1, for a better visualisation the results of the GPS data processing are transformed into UTM coordinates. It became obvious that the reference station (BASE) moved between the measurement periods (see Tab. 12).

<sup>10</sup><http://www.cloudcompare.org/doc/wiki/index.php5?title=PluginM3C2>



BASE	absolute coordinates			reduced coordinates			$\sigma$ [mm]		
	E[m]	N[m]	h[m]	E[m]	N[m]	h[m]	E	N	h
period 1 (Apr 13)	721172.175	9257760.957	1355.829	0.000	0.000	0.000	0.4	0.3	0.8
period 2 (Sept 13)	721172.170	9257760.962	1355.623	-0.005	0.005	-0.207	0.7	0.4	1.1
period 3 (Dec 13)	721172.188	9257760.951	1355.579	0.013	-0.006	-0.251	0.3	0.2	0.6

Table 12: Displacement of the BASE station between the measurement periods

The reduced coordinates show the coordinate differences with respect to the BASE station coordinates of the initial period. The quoted accuracies  $\sigma$  denote the formal errors from the data processing in Bernese.

Afterwards the reduced measurement coordinates (CT01 - CT10) of each period are calculated. A listing of the GPS coordinates and their standard deviation  $\sigma$  is shown in Tab. 13. The colours indicate whether the measurement point got lost between the measurement periods.

**Period 1 (April 2013)**

POS	absolute GPS coordinates			reduced GPS coordinates			$\sigma$ [mm]		
	E[m]	N[m]	h[m]	E[m]	N[m]	h[m]	E	N	h
BASE	721172.175	9257760.957	1355.829	0.000	0.000	0.000	0.4	0.3	0.8
CT01	721197.771	9257762.563	1352.079	25.596	1.606	-3.751	0.2	0.2	0.4
CT02	721187.971	9257719.161	1343.138	15.796	-41.796	-12.691	0.4	0.3	0.6
CT03	721179.629	9257698.395	1347.101	7.454	-62.562	-8.728	0.2	0.2	0.4
CT04	721204.182	9257681.063	1343.153	32.007	-79.894	-12.676	0.8	0.5	1.4
CT05	721198.346	9257628.579	1334.656	26.171	-132.378	-21.174	0.2	0.2	0.4
CT06	721234.416	9257619.520	1326.615	62.241	-141.437	-29.215	0.3	0.2	0.6
CT07	721230.273	9257585.264	1322.031	58.098	-175.693	-33.798	0.4	0.2	0.7
CT08	721229.946	9257556.928	1315.171	57.771	-204.029	-40.659	0.6	0.4	1.0
CT09	721210.085	9257535.176	1310.424	37.910	-225.781	-45.406	0.7	0.4	1.1
CT10	721261.824	9257515.449	1309.895	89.648	-245.508	-45.935	0.3	0.2	0.4

**Period 2 (September 2013)**

POS	absolute GPS coordinates			reduced GPS coordinates			$\sigma$ [mm]		
	E[m]	N[m]	h[m]	E[m]	N[m]	h[m]	E	N	h
BASE	721172.170	9257760.962	1355.623	-0.005	0.005	-0.207	0.7	0.4	1.1
CT01	721197.758	9257762.565	1352.023	25.583	1.608	-3.806	0.4	0.3	0.7
CT02	721187.982	9257719.135	1343.099	15.806	-41.822	-12.730	0.8	0.5	1.5
CT03	721179.623	9257698.374	1346.776	7.447	-62.583	-9.054	0.4	0.2	0.8
CT04	721204.215	9257681.048	1342.986	32.040	-79.909	-12.843	1.6	1.0	2.9
CT05	721198.290	9257628.613	1334.417	26.115	-132.344	-21.413	0.4	0.3	0.6
CT06	721234.374	9257619.393	1326.832	62.199	-141.565	-28.998	0.3	0.3	0.5
CT07	721230.320	9257585.142	1321.931	58.145	-175.815	-33.899	1.0	0.6	1.4
CT08	721229.943	9257556.807	1315.034	57.768	-204.151	-40.796	0.5	0.3	0.8
CT09	721210.075	9257535.176	1310.379	37.900	-225.781	-45.450	1.0	0.5	1.4
CT10	721261.755	9257514.963	1310.108	89.580	-245.994	-45.722	0.4	0.2	0.7

**Period 3 (December 2013)**

POS	absolute coordinates			reduced coordinates			$\sigma$ [mm]		
	E[m]	N[m]	h[m]	E[m]	N[m]	h[m]	E	N	h
BASE	721172.188	9257760.951	1355.579	0.013	-0.006	-0.251	0.3	0.2	0.6
CT01	721198.835	9257766.184	1352.073	26.660	5.227	-3.757	0.8	0.5	1.3
CT02	721195.918	9257727.559	1344.612	23.743	-33.398	-11.217	0.9	0.7	1.7
CT03	721180.121	9257698.145	1346.700	7.946	-62.812	-9.129	0.6	0.4	1.0
CT04	721204.252	9257681.029	1342.940	32.076	-79.928	-12.890	9.3	3.5	8.7
CT05	721198.309	9257628.617	1334.383	26.134	-132.340	-21.447	0.8	0.6	1.3
CT06	721234.377	9257619.347	1326.784	62.202	-141.610	-29.045	0.8	0.6	1.3
CT07	721230.360	9257585.080	1321.887	58.185	-175.877	-33.943	1.1	0.7	1.8
CT08	721229.984	9257556.771	1315.032	57.809	-204.186	-40.797	4.0	1.6	3.9
CT09	721210.078	9257535.177	1310.311	37.903	-225.781	-45.519	1.1	0.7	1.7
CT10	721261.765	9257514.944	1310.063	89.591	-246.013	-45.766	0.7	0.5	1.2

Table 13: Estimated absolute GPS coordinates from measurement campaign

	... same measurement points in every period
	... points got lost between period 1 and 2
	... points got lost between period 2 and 3
	... points got lost between every period

**3.3.2 TLS results****Georeferencing of the TLS data**

The results of the georeferencing are listed in Tab. 14. The georeferencing is realised by the transformation from the roughly transformed TLS coordinates (see Tab. 8) to the reduced GPS coordinates (see Tab. 13). The estimated parameters are listed in Tab. 10. The matrices in Tab. 11 are used for the transformation in CC.

Based on the transformed TLS coordinates the absolute TLS coordinates are calculated by an addition of the coordinates of the reference station of GPS period 1 (reference values of the coordinate reduction - see Tab. 12 in section 3.3.1).

**Period 1 (April 2013)**

POS	transformed TLS coordinates			absolute TLS coordinates		
	X[m]	Y[m]	Z[m]	X[m]	Y[m]	Z[m]
BASE	0.019	-0.013	-0.064	721172.194	9257760.944	1355.765
CT01	25.610	1.603	-3.718	721197.785	9257762.560	1352.111
CT02	15.795	-41.803	-12.653	721187.970	9257719.154	1343.178
CT03	7.442	-62.565	-8.680	721179.617	9257698.392	1347.150
CT04	32.019	-79.910	-12.661	721204.194	9257681.047	1343.169
CT05	26.125	-132.379	-21.172	721198.300	9257628.578	1334.658
CT06	62.201	-141.405	-28.960	721234.376	9257619.552	1326.869
CT07	58.093	-175.668	-33.828	721230.268	9257585.290	1322.002
CT08	57.791	-204.019	-40.660	721229.967	9257556.938	1315.170
CT09	37.919	-225.795	-45.394	721210.094	9257535.162	1310.436
CT10	—	—	—	—	—	—

**Period 2 (September 2013)**

POS	transformed TLS coordinates			absolute TLS coordinates		
	X[m]	Y[m]	Z[m]	X[m]	Y[m]	Z[m]
BASE	-0.011	-0.004	-0.197	721172.165	9257760.954	1355.633
CT01	25.584	1.610	-3.807	721197.759	9257762.567	1352.023
CT02	15.800	-41.801	-12.767	721187.975	9257719.157	1343.062
CT03	7.441	-62.582	-9.044	721179.616	9257698.375	1346.785
CT04	32.071	-79.920	-12.830	721204.246	9257681.037	1343.000
CT05	26.109	-132.354	-21.409	721198.284	9257628.603	1334.421
CT06	62.191	-141.554	-29.004	721234.366	9257619.403	1326.826
CT07	58.149	-175.832	-33.894	721230.324	9257585.125	1321.936
CT08	57.778	-204.140	-40.762	721229.953	9257556.817	1315.068
CT09	37.882	-225.785	-45.473	721210.057	9257535.172	1310.356
CT10	89.584	-245.990	-45.731	721261.759	9257514.967	1310.098

**Period 3 (December 2013)**

POS	X[m]	Y[m]	Z[m]	X[m]	Y[m]	Z[m]
BASE	0.002	-0.002	-0.254	721172.177	9257760.956	1355.575
CT01	26.652	5.227	-3.762	721198.828	9257766.184	1352.067
CT02	—	—	—	—	—	—
CT03	7.942	-62.813	-9.130	721180.117	9257698.144	1346.700
CT04	32.113	-79.935	-12.875	721204.288	9257681.022	1342.954
CT05	26.129	-132.351	-21.448	721198.304	9257628.606	1334.383
CT06	62.207	-141.610	-29.043	721234.382	9257619.347	1326.787
CT07	58.189	-175.880	-33.941	721230.364	9257585.077	1321.888
CT08	57.799	-204.178	-40.812	721229.974	9257556.779	1315.017
CT09	37.894	-225.777	-45.516	721210.069	9257535.180	1310.313
CT10	89.591	-246.008	-45.762	721261.766	9257514.949	1310.068

Table 14: Transformed and absolute TLS coordinates

POS	Period 1 (April)			Period 2 (September)			Period 3 (December)		
	$dX$ [m]	$dY$ [m]	$dZ$ [m]	$dX$ [m]	$dY$ [m]	$dZ$ [m]	$dX$ [m]	$dY$ [m]	$dZ$ [m]
BASE	0.019	-0.013	-0.064	-0.006	-0.009	0.010	-0.011	0.005	-0.004
CT01	0.014	-0.003	0.033	0.001	0.001	-0.001	-0.007	0.001	-0.005
CT02	-0.001	-0.007	0.038	-0.006	0.022	-0.037	—	—	—
CT03	-0.012	-0.003	0.048	-0.007	0.001	0.010	-0.004	-0.001	-0.001
CT04	0.012	-0.016	0.016	0.031	-0.010	0.014	0.037	-0.006	0.015
CT05	-0.046	-0.002	0.002	-0.006	-0.010	0.004	-0.006	-0.011	-0.001
CT06	-0.040	0.032	0.255	-0.008	0.011	-0.006	0.005	0.001	0.003
CT07	-0.005	0.026	-0.029	0.004	-0.017	0.005	0.004	-0.003	0.001
CT08	0.021	0.010	-0.001	0.011	0.010	0.034	-0.010	0.008	-0.015
CT09	0.010	-0.014	0.012	-0.019	-0.004	-0.023	-0.009	0.003	0.002
CT10	—	—	—	0.005	0.004	-0.010	0.001	0.005	0.004

Table 15: Misclosures between the GPS and TLS coordinates

... misclosures between  $\pm 1.5\text{cm}$  and  $\pm 3.0\text{cm}$   
 ... misclosures  $> \pm 3.0\text{cm}$

In Tab. 15 the misclosures between the reduced GPS coordinates and the transformed TLS coordinates (the difference between the absolute coordinates of GPS and TLS also conforms) are listed.

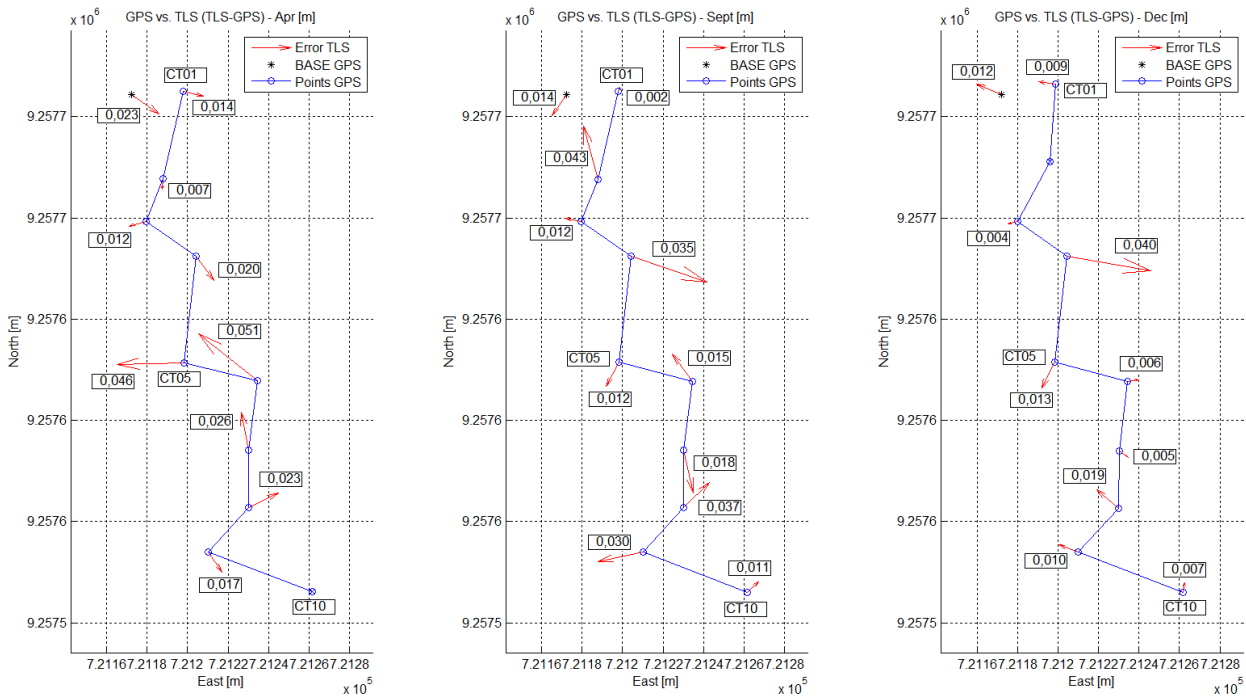


Figure 42: Horizontal misclosures between the GPS and TPS viewpoints

In Tab. 15 and Fig. 42 no systematic differences between the GPS values and transformed TLS values are discernible. The differences of the values are small and the offset between the TLS positions and GPS shows in different directions.

Between the TLS and the GPS viewpoints higher misclosures are discernible in period 1 than in period 2 and 3. Due to an erroneous measurement to a target mark the point cloud of period 1 was split up in two parts which were georeferenced separately. After the nexus of these separated parts a new georeferencing was necessary. These are the reasons why the viewpoints in Tab. 15 of period 1 show high values of misclosures ( $> \pm 3.0\text{cm}$ ). CT06 in period 1 indicates an outlier.

### Comparison of the periods

In section 3.2.2 the data preparation is explained. It can be made clear how the desired solution is created. Beginning with the georeferenced point clouds in CC the three clouds of April, September and December are generated using following steps:

- Triangulation by the *Delaunay*<sup>11</sup> function.
- Second, smooth by the *Laplace*-operator with 30 iterations and a smooth factor of 0.2.
- Third, comparison of the smoothed meshes in different directions ( $X$ ,  $Y$  and  $Z$ ) and assigned distances by the Plugin M3C2-tool in CC.

The comparison of the data between the periods in opposing directions is especially important for the analysis and the comparison with the GPS solution (see section 4.2.3). In Fig. 43 the comparison between the periods in vertical direction is displayed.

<sup>11</sup>Delaunay triangulation: for more details see [Eling, 2009, p. 26-27] 2D (XY-plane)

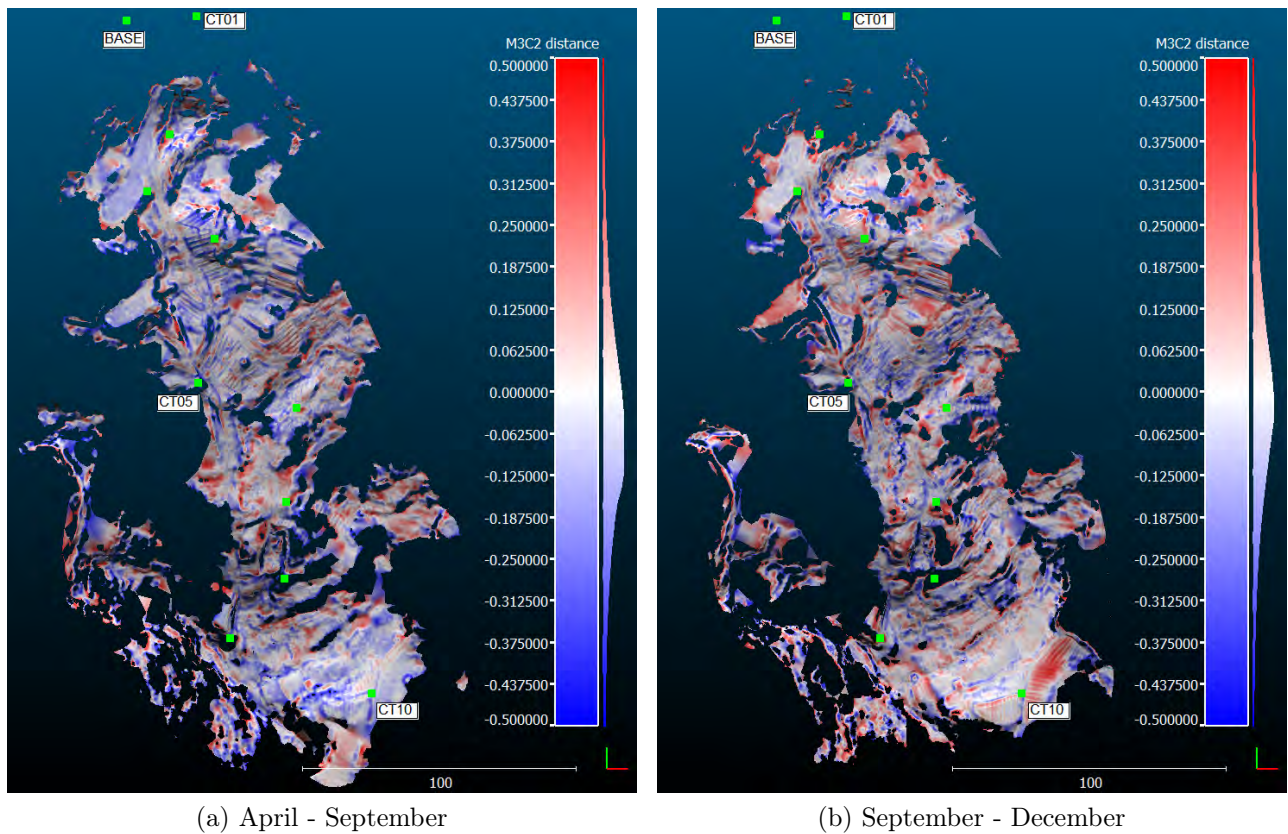


Figure 43: Comparison of the displacements in vertical direction [m]

### 3.3.3 Overall accuracy of the measurements

In equation (2.10) the transformation of the measured TLS values of  $s$ ,  $\xi$  and  $\alpha$  (distance, crown and horizontal angle - see Fig. 22) to  $x$ ,  $y$  and  $z$  are displayed. This formula derived by the measured variables and applied by the covariance error propagation (2.14) together with the information of the measurement accuracy of the device given by the manufacturer ( $s = 4\text{mm}$  and  $\xi = \alpha = 12''$  - see section 3.1.2) calculates the accuracy of single scans. Fig. 44 shows the horizontal measurement accuracy from individual viewpoints up to a measurement distance of 50m by three different elevation angles  $\xi$  ( $60^\circ$ ,  $90^\circ$  and  $150^\circ$ ). The three pictures in the first line represent the point accuracy in direction  $X$  and the second line in direction  $Y$ . In vertical direction no distinction is made concerning  $X$  and  $Y$ . The worst case of the 3D point position error (between 4 and 5.7mm independent of the three elevation angles) of single scans are shown in Fig. 45.

Every viewpoint is defective. Based on the assumption that the observation point of CT01 is free of errors, the accuracies of the measured target marks (for the nexus of the viewpoints and single scans) and the following viewpoints are calculated by a bundle block adjustment (see section 3.2.2 - Accuracy of the registration). The used measurement accuracies of the target marks are the accuracies according to manufacturer information (2mm - see section 3.1.2). A second covariance error propagation (2.14) estimates the accuracy of the TLS results with allowance for the accuracies of the single scans (see Fig. 45) and the accuracies of the viewpoints after the nexus (see Tab. 6) which were estimated by the bundle block adjustment. The results are shown in Fig. 46 by the 3D point position error. In the worst case, the error analysis of the TLS results gives a measurement accuracy up to 27mm (3D point position error) at the scanned points around standing point CT10.

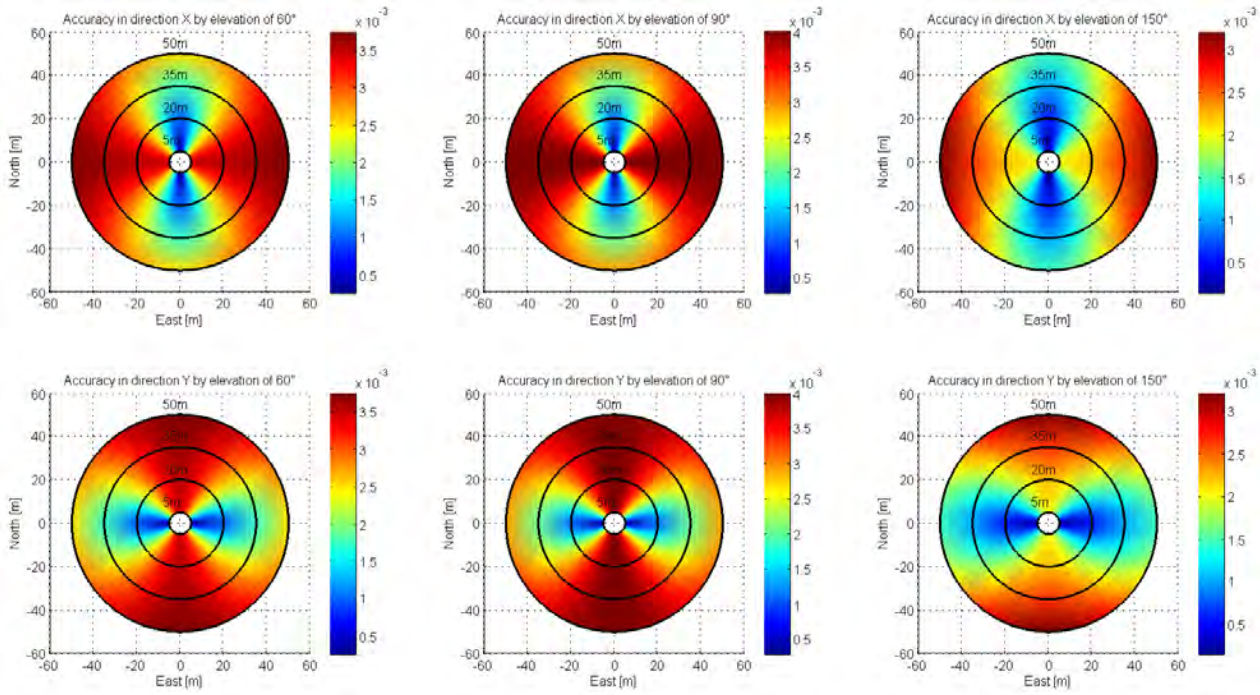


Figure 44: Point accuracy of the single scan measurements in directions X and Y

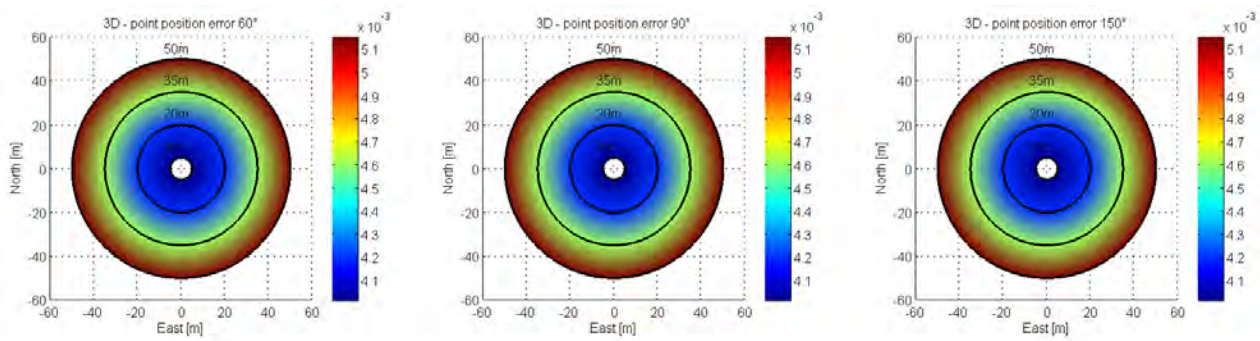


Figure 45: 3D point position error of the single scan measurements

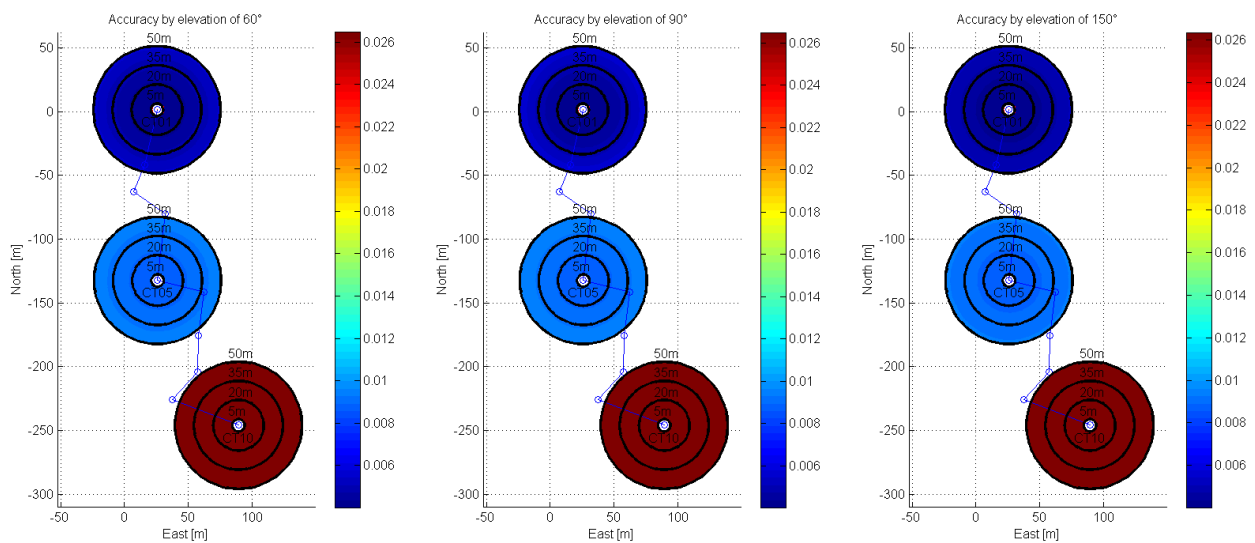


Figure 46: 3D point accuracy of the TLS results

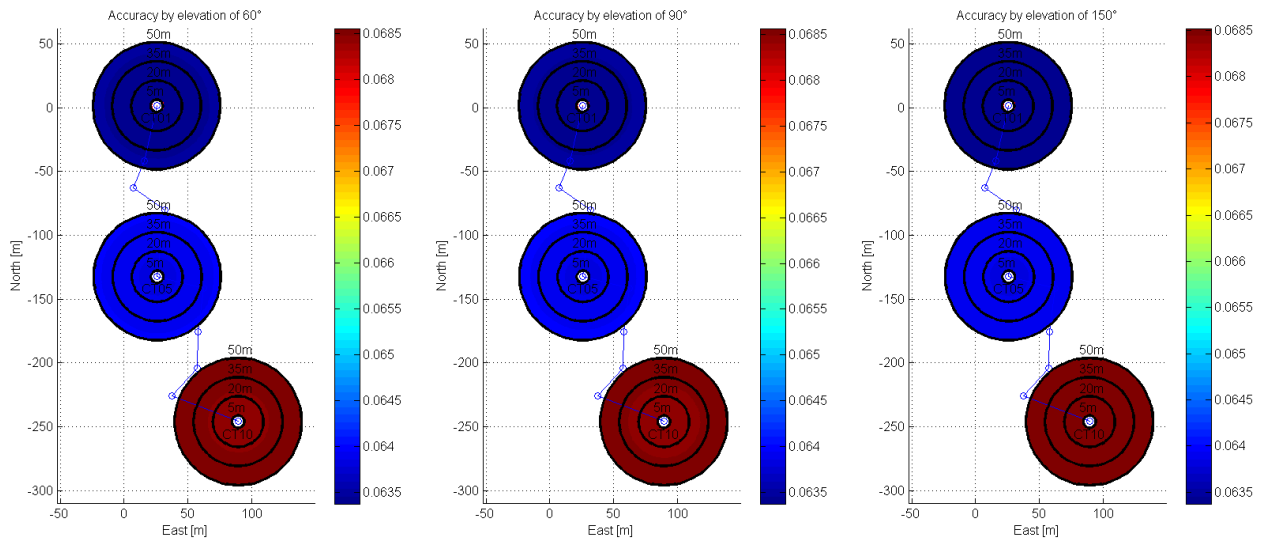


Figure 47: 3D point accuracy of the whole measurements

In a third part the overall accuracy of the measurements is calculated. The calculation of the transformation parameters by the *Gauß-Helmert* model (see section 3.2.2 - Georeferencing) takes into account the accuracies of the GPS measurements. Together with the accuracy of the transformation parameters (georeferencing - see Tab. 10) a covariance matrix for the last covariance error propagation was created. The ongoing accuracy of the TLS solution (single scans and their nexus - solutions of the previous covariance error propagations), which is predicted and displayed in Fig. 46, is estimated by this covariance matrix. As shown in Fig. 47 the 3D point position error for CT01 is calculated between 63.4 – 63.5mm, for CT05 is estimated between 63.9 – 64.0mm and CT10 is calculated between 68.5 – 68.7mm. These results follows from the estimated accuracies in directions  $X$ ,  $Y$  and  $Z$ . In the worst case at viewpoint CT10 it is  $\sigma_X = 36\text{mm}$ ,  $\sigma_Y = 21\text{mm}$  and  $\sigma_Z = 55\text{mm}$ .

The used accuracies for this analysis are calculated by Bernese (GPS viewpoints) and by the transformation via the Gauß-Helmert model (georeferencing). The precision data of the measured points in the point clouds by TLS got lost. Therefore theoretical measurement points and the measurement accuracy, which is declared by the manufacturer of the TLS device (see section 2.6.3 - TLS-device: Leica ScanStation C10), are used. The loss of the accuracies from the real TLS data impeded a calculation of significant movements out of the real point clouds. It makes no sense to check significant displacements by equations (2.20) - (2.23) because in the movement area no identical points are measured. The sliding area is relatively flat. Thus, a control about significant movements in vertical direction would be most sensible. It is possible to use the same equations but only with coordinates and accuracies in  $Z$  direction and selected areas which include measurement points out of two periods. The calculated overall accuracy in this analysis is only an assumption.

In the following, the statistical significance test is done by the measured GPS viewpoints. These are the only identical points of the measurements. The comparison of the point clouds is done without a significance test.

## 4 Mass movement modelling

As described in section 2.3.2 the mass movement in Ciloto consists of several independent movements (rotational, translational and compound). The types of sliding planes can be triggered by the following factors:

- High pressure of interstitial water (main trigger in Ciloto).
- High load of the surface.
- Shaking or vibrations by natural or human generated phenomena.

The mass movement in Ciloto includes two or more minor movements. The west side has a tendency for a rotational movement, the east side to a planar slip plane. The measurements for this research are done in the northern part along an assumed border between a rotational and a translational plane. In the following steps the evaluations of the observations are discussed. The basics about the geometric model are described in section 2.3.1.

### 4.1 Determination and validation of the static model

The GPS coordinates obtained within the three periods are listed in Tab. 13. Tab. 16 shows the displacements of the measurement points. The statistical significance test (see section 2.6.3) checks the actual point movements by the t-Student distribution. All GPS measurement points with exception CT04 and CT08 between period 2 and 3 are marked as significant displacements. For the two non-significant movements the criteria check in Fig. 25 is conducted positively. In this case, all measurement points moved significantly. It should be noted that the accuracies  $\sigma$  of the estimated GPS coordinates in Tab. 13 are deteriorated by a factor 10. These are the precisions which are free of functional errors and can occur in the worst case (see e.g. Dach et al. [2007]). The GPS displacements during the periods listed in Tab. 16 are graphically depicted in Fig. 48 and 49.

The left graphic in Fig. 49 shows the horizontal displacements between the first and second GPS measurement period (April - September 2013). The movements in the middle graphic happened during the second and third period (September - December 2013). On the right side the displacements between the first and last observations are depicted.

**Displacement during period 1 and 2**

POS	difference of period 2-1			$\sigma$ [mm]			t-Student test ( $f = \infty; \alpha = 99\%; t_{f,\alpha/2} = 2.58$ )			
	$dE$ [m]	$dN$ [m]	$dh$ [m]	$dE$	$dN$	$dh$	$d_{2-1}$	$\sigma d_{2-1}$	$T$	$ T  > t_{f,\alpha/2}$
BASE	-0.0049	0.0050	-0.2069	8.1	5.0	13.6	0.2070	0.0136	15.23	true
CT01	-0.0130	0.0020	-0.0552	4.5	3.6	8.1	0.0567	0.0079	7.17	true
CT02	0.0109	-0.0265	-0.0394	8.9	5.8	16.2	0.0487	0.0136	3.58	true
CT03	-0.0062	-0.0214	-0.3254	4.5	2.8	8.9	0.3262	0.0089	36.54	true
CT04	0.0331	-0.0157	-0.1672	17.9	11.2	32.2	0.1712	0.0317	5.41	true
CT05	-0.0559	0.0336	-0.2392	4.5	3.6	7.2	0.2479	0.0070	35.18	true
CT06	-0.0422	-0.1279	0.2171	4.2	3.6	7.8	0.2555	0.0069	36.95	true
CT07	0.0473	-0.1217	-0.1008	10.8	6.3	15.7	0.1650	0.0111	14.89	true
CT08	-0.0034	-0.1218	-0.1371	7.8	5.0	12.8	0.1834	0.0101	18.10	true
CT09	-0.0094	0.0002	-0.0445	12.2	6.4	17.8	0.0455	0.0176	2.58	true
CT10	-0.0687	-0.4867	0.2134	5.0	2.8	8.1	0.5359	0.0042	128.76	true



**Displacement during period 2 and 3**

POS	$dE$ [m]	$dN$ [m]	$dh$ [m]	$dE$	$dN$	$dh$	$d_{2-1}$	$\sigma d_{2-1}$	$T$	$ T  > t_{f,\alpha/2}$
BASE	0.0174	-0.0110	-0.0438	7.6	4.5	12.5	0.0484	0.0117	4.13	true
CT01	1.0768	3.6182	0.0492	8.9	5.8	14.8	3.7754	0.0061	614.28	true
CT02	7.9362	8.4238	1.5131	12.0	8.6	22.7	11.6719	0.0107	1092.12	true
CT03	0.4987	-0.2288	-0.0755	7.2	4.5	12.8	0.5539	0.0070	79.43	true
CT04	0.0363	-0.0190	-0.0463	94.4	36.4	91.7	0.0618	0.0889	0.70	false
CT05	0.0195	0.0039	-0.0340	8.9	6.7	14.3	0.0394	0.0131	3.00	true
CT06	0.0029	-0.0457	-0.0477	8.5	6.7	13.9	0.0661	0.0111	5.97	true
CT07	0.0400	-0.0620	-0.0438	14.9	9.2	22.8	0.0858	0.0151	5.68	true
CT08	0.0409	-0.0351	-0.0017	40.3	16.3	39.8	0.0539	0.0324	1.67	false
CT09	0.0028	0.0002	-0.0684	14.9	8.6	22.0	0.0685	0.0220	3.11	true
CT10	0.0101	-0.0185	-0.0449	8.1	5.4	13.9	0.0496	0.0128	3.86	true

**Displacement during period 1 and 3**

POS	$dE$ [m]	$dN$ [m]	$dh$ [m]	$dE$	$dN$	$dh$	$d_{2-1}$	$\sigma d_{2-1}$	$T$	$ T  > t_{f,\alpha/2}$
BASE	0.0125	-0.0060	-0.2507	5.0	3.6	10.0	0.2511	0.0100	25.14	true
CT01	1.0638	3.6202	-0.0060	8.2	5.4	13.6	3.7733	0.0057	665.98	true
CT02	7.9471	8.3973	1.4737	9.8	7.6	18.0	11.6552	0.0090	1299.84	true
CT03	0.4925	-0.2502	-0.4009	6.3	4.5	10.8	0.6826	0.0080	85.63	true
CT04	0.0694	-0.0347	-0.2135	93.3	35.4	88.1	0.2272	0.0878	2.59	true
CT05	-0.0364	0.0375	-0.2732	8.2	6.3	13.6	0.2782	0.0134	20.71	true
CT06	-0.0393	-0.1736	0.1694	8.5	6.3	14.3	0.2457	0.0109	22.50	true
CT07	0.0873	-0.1837	-0.1446	11.7	7.3	19.3	0.2496	0.0131	19.10	true
CT08	0.0375	-0.1569	-0.1388	40.4	16.5	40.3	0.2128	0.0298	7.14	true
CT09	-0.0066	0.0004	-0.1129	13.0	8.1	20.2	0.1131	0.0202	5.59	true
CT10	-0.0586	-0.5052	0.1685	7.6	5.4	12.6	0.5358	0.0065	82.37	true

Table 16: Displacements of GPS measurements between the periods and their significance  
 ... points got lost during the periods (details in Tab. 13)

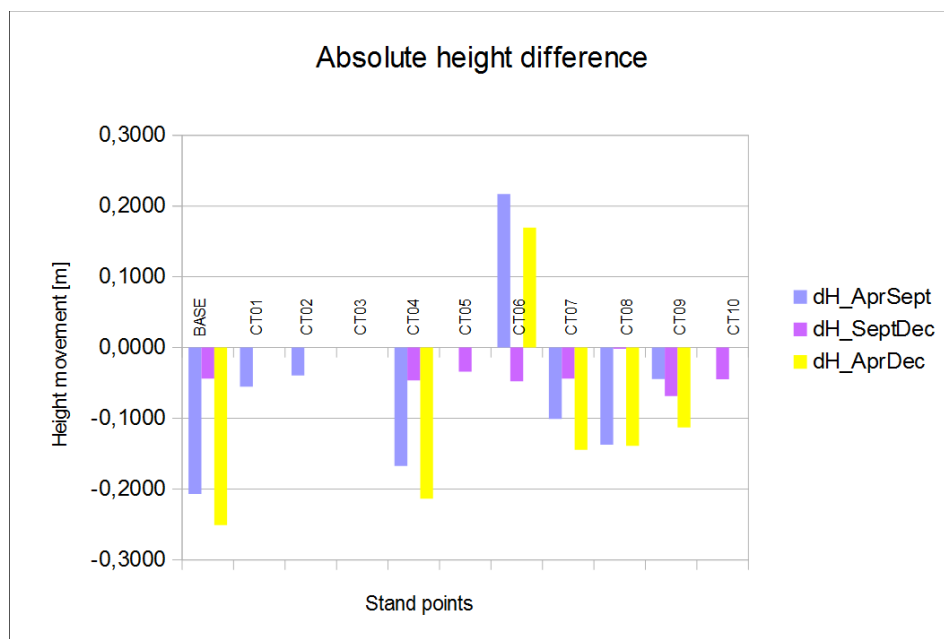


Figure 48: Absolute vertical movements of the GPS viewpoints

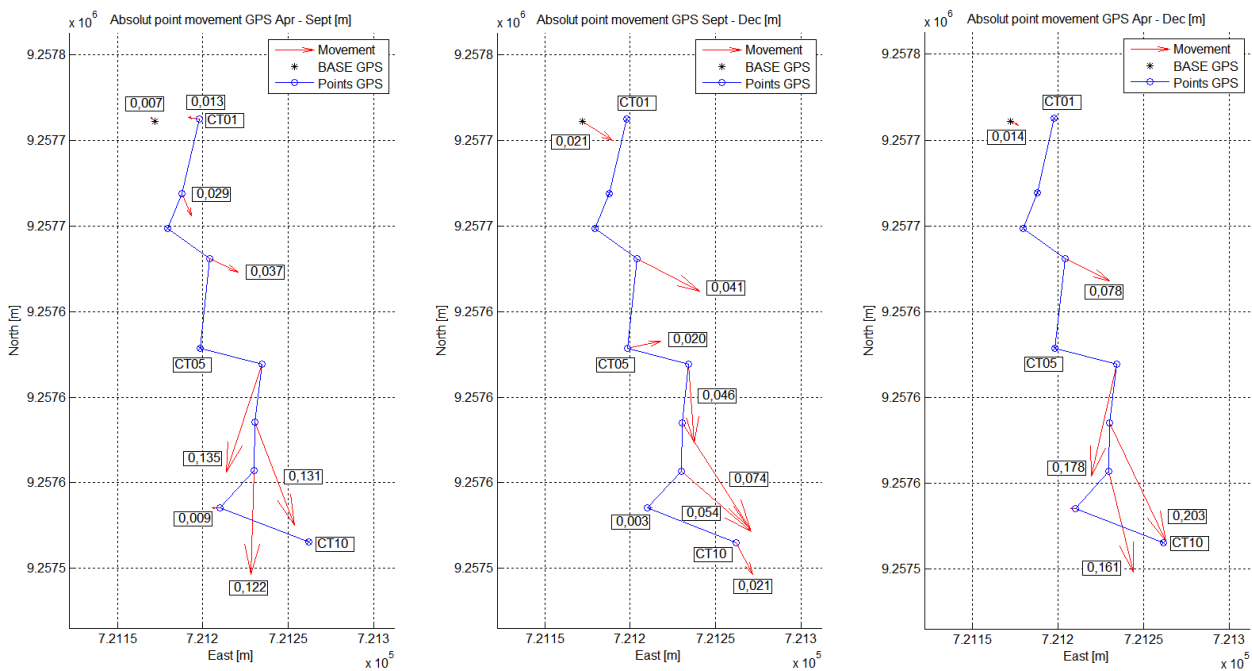


Figure 49: Absolute horizontal movements of the GPS viewpoints

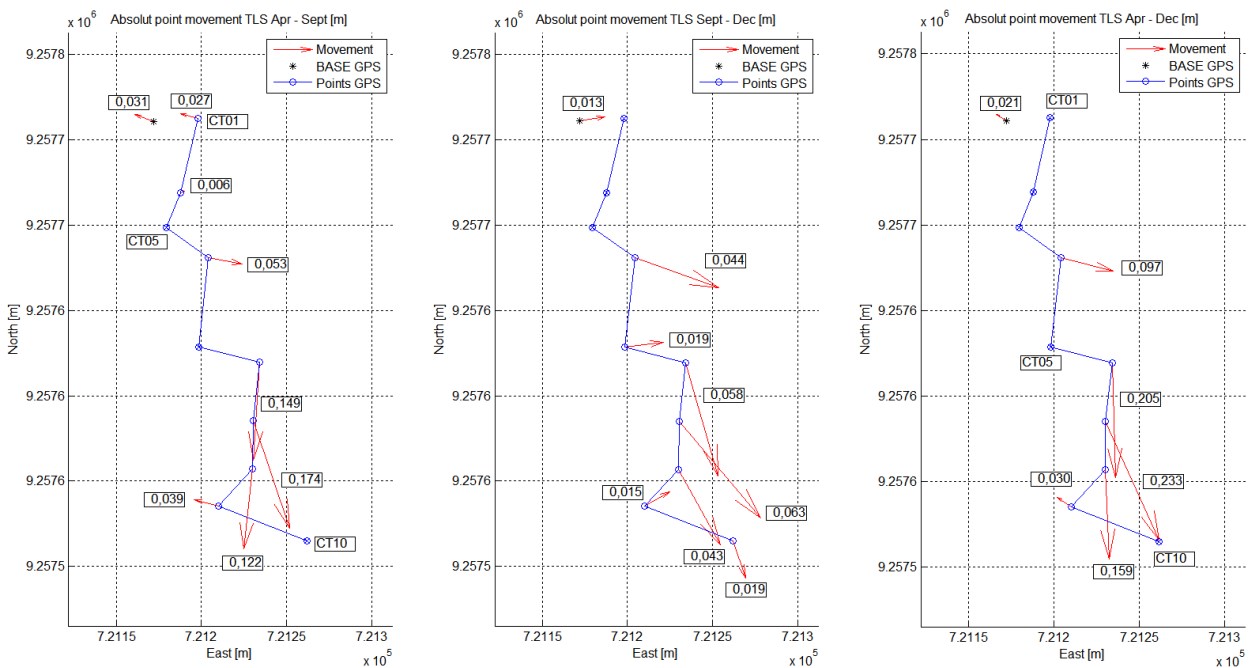


Figure 50: Absolute horizontal movements of the TLS viewpoints

A comparison of the displacements between the analysis of the GPS and TLS viewpoints are visible in Fig. 49 and 50. In Tab. 17 and 18 the movements are listed in direction  $X$ ,  $Y$  and  $Z$ . The misclosures between the GPS and TLS viewpoints are in a range of few centimetres (see Tab. 15). The differences of the movements between the GPS and TLS viewpoints are in a similar range. In Fig. 49 and 50 it is discernible that the displacements show in similar directions. One reason for the not exact similar depicted displacements between the GPS and TLS solutions are the inaccuracy of the nexus of the point clouds (was done before the georeferencing). Another reason is that the measurements of GPS and TLS were done without forced centering.

POS	Period 2-1			Period 3-2			Period 3-1		
	$dX[m]$	$dY[m]$	$dZ[m]$	$dX[m]$	$dY[m]$	$dZ[m]$	$dX[m]$	$dY[m]$	$dZ[m]$
BASE	-0.005	0.005	-0.207	0.017	-0.011	-0.044	0.012	-0.006	-0.251
CT01	-0.013	0.002	-0.055	—	—	—	—	—	—
CT02	0.011	-0.027	-0.039	—	—	—	—	—	—
CT03	—	—	—	—	—	—	—	—	—
CT04	0.033	-0.016	-0.167	0.036	-0.019	-0.046	0.069	-0.035	-0.214
CT05	—	—	—	0.020	0.004	-0.034	—	—	—
CT06	-0.042	-0.128	0.217	0.003	-0.046	-0.048	-0.039	-0.174	0.169
CT07	0.047	-0.122	-0.101	0.040	-0.062	-0.044	0.087	-0.184	-0.145
CT08	-0.003	-0.122	-0.137	0.041	-0.035	-0.002	0.037	-0.157	-0.139
CT09	-0.009	0.000	-0.044	0.003	0.000	-0.068	-0.007	0.000	-0.113
CT10	—	—	—	0.010	-0.018	-0.045	—	—	—

Table 17: Absolute movements of the GPS viewpoints

POS	Period 2-1			Period 3-2			Period 3-1		
	$dX[m]$	$dY[m]$	$dZ[m]$	$dX[m]$	$dY[m]$	$dZ[m]$	$dX[m]$	$dY[m]$	$dZ[m]$
BASE	-0.030	0.010	-0.132	0.012	0.002	-0.058	-0.017	0.012	-0.190
CT01	-0.026	0.007	-0.088	—	—	—	—	—	—
CT02	0.005	0.002	-0.115	—	—	—	—	—	—
CT03	—	—	—	—	—	—	—	—	—
CT04	0.052	-0.010	-0.169	0.042	-0.015	-0.045	0.094	-0.025	-0.214
CT05	—	—	—	0.019	0.002	-0.039	—	—	—
CT06	-0.010	-0.149	-0.044	0.016	-0.056	-0.039	0.006	-0.205	-0.082
CT07	0.056	-0.164	-0.066	0.040	-0.048	-0.048	0.096	-0.212	-0.114
CT08	-0.013	-0.121	-0.102	0.021	-0.038	-0.051	0.007	-0.159	-0.153
CT09	-0.037	0.010	-0.080	0.013	0.007	-0.043	-0.025	0.017	-0.123
CT10	—	—	—	0.007	-0.018	-0.031	—	—	—

Table 18: Absolute movements of the TLS viewpoints

Fig. 49 and 50 display that the horizontal movements are larger in the southern (up to 20cm) than in the northern part (up to 7cm) and the movements show different directions. The tendency of the northern part movement is to the east and south-east direction, the southern part moves to the south direction. It looks like a clockwise rotating movement. A big crack in the soil, which is located east of the points CT06, CT07 and CT08, is shown in Fig. 35 and in the right picture in Fig. 11. This crack starts between points CT05 and CT06 and indicates that the southern part in the west side of the crack is moving independently towards the northern part. It is also discernible that the movement direction of the southern part changes during the April-September movements (dry season) and the September-December movements (beginning of the wet season). This might be an evidence of changing pore water pressure between the dry and wet period. More information about wet and dry periods is provided in section 4.2.2.

Vertical movements (see Fig. 48) are detected in all points which signalise subsidences (without number CT06). The largest deviations (around 20cm) are found at the top of the movement area during the first and second measurement period. Fig. 35 displays that the reference station is positioned above the street at the top of the movement. The main scarp of the sliding plane is located in this area (see section 2.3.2 - Static model). After the first mea-

surement campaign, beginning of April 2013, a heavy rainfall occurred. Around 50m west of the reference station the street broke down. Construction works started and heavy machines reconstructed the street. Vibrations and wet soil around the reference station are reasons for significant settlements.

Water infiltration from surface, along with seepage, causes that some material structures in the soil construction turn into a slip plane. Clay is the essential element of the soil structure and occurs most frequently in the middle and southern part of the whole landslide (see Fig. 10 and 12). In conjunction with water, clay swells up. This can be a reason why the subsidence is stronger in the northern part because the swelling clay reduces the subsidence in the southern part. Wet clay is also more slippery in conjunction with water and acts as a slip plane. This phenomenon can be justified because the horizontal displacements in the southern area are higher than in the northern area.

Point number CT06 shows an extremely high positive vertical displacement between the first and second period ( $> 21\text{cm}$  - see Fig. 48). In comparison with the adjacent points it looks like an outlier, which is maybe due to a wrongly noted instrument height in April. The vertical displacements between the second and third period are constantly negative for all observed viewpoints.

## 4.2 Analysis of the results concerning TLS

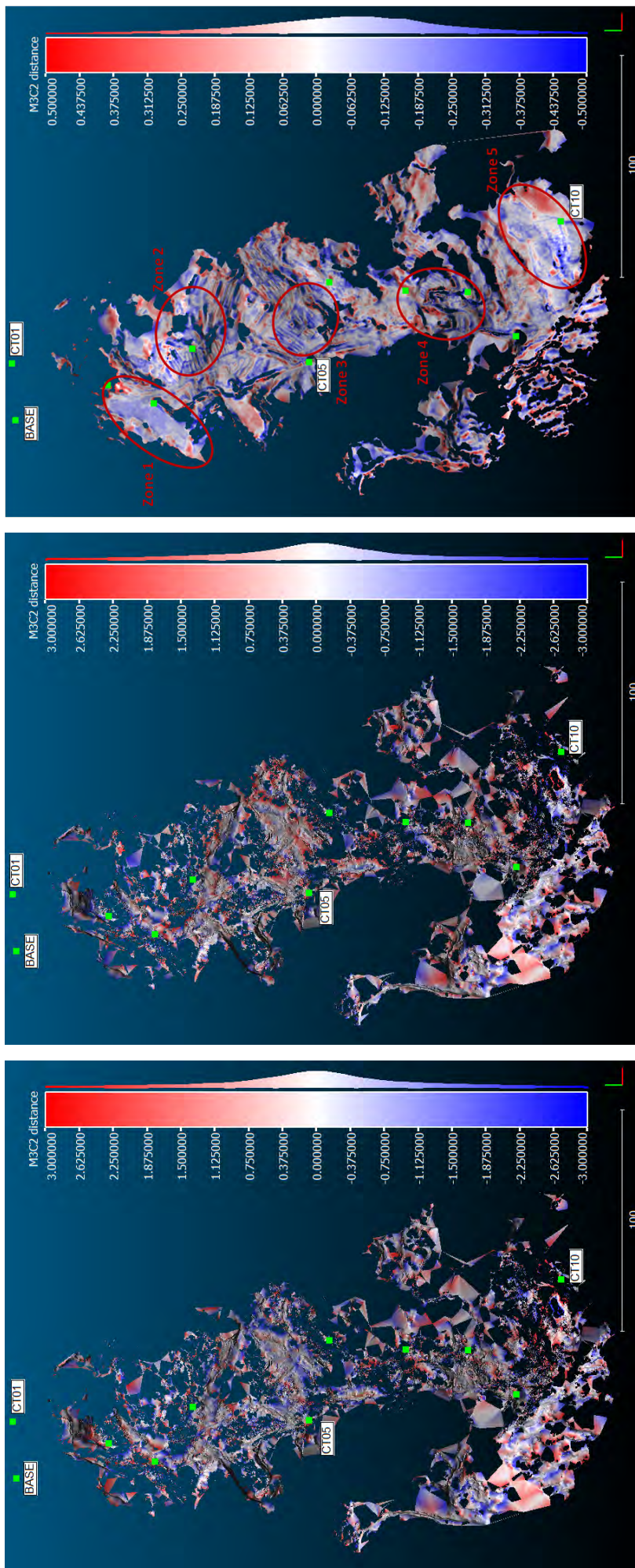
The analysis of the point clouds from the three periods is done in CloudCompare (CC). The comparison of the TLS data in vertical and horizontal direction is conducted because no identical points during the measurement periods are measured.

In Fig. 43 vertical shifts between the periods are discernible. A comparison between the first and the last measurement period of TLS is shown in Fig. 51c. Fig. 51a and 51b display horizontal movements in direction  $X$  (red axis) and  $Y$  (green axis) during the first and last period.

It is noticeable that more than 50% of the displacements emerge as subsidence (see Fig. 51c). The shifts in the horizontal plane are balanced but highly distributed and an abstraction in  $X$  and  $Y$  shows relatively high values of the displacements. Vertical movements (uplifts or subsidences), which occur mostly in this relatively flat measurement area, are the main reason why horizontal displacements are often indicated by high values and wrong directions.

Now, different zones of the measurement area are analysed in detail. Classifications of the zones are marked in Fig. 51c. Some general remarks:

- The axes in the pictures of the TLS results are coloured ( $X$  - red axis,  $Y$  - green axis,  $Z$  - blue axis).
- The unit of the values is [m].
- Displacements in  $X$  signalise movements in  $YZ$ -plane, displacements in  $Y$  indicate movements in  $XZ$ -plane and displacements in  $Z$  signalise movements in  $XY$ -plane.
- Holes in the scans mark that no TLS data is available or the displacements (especially in the horizontal movement) are out of the scale-range (see Fig. 51a and 51b).



(a) April - December: horizontal displacement in X

(b) April - December: horizontal displacement in Y

(c) April - December: vertical displacement in Z

Figure 51: Comparison of the displacements [m] in horizontal and vertical direction

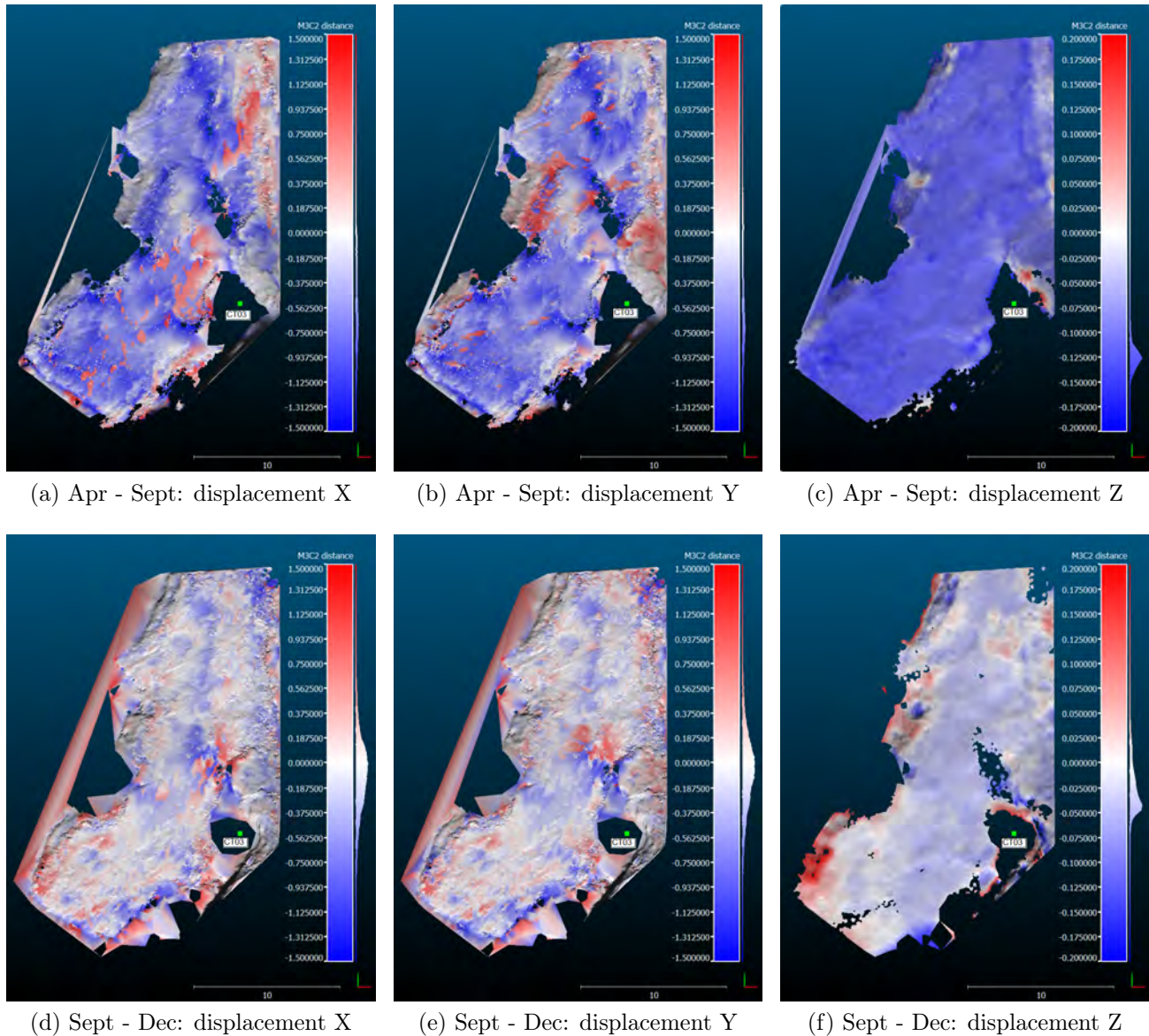
**Zone 1:**

Figure 52: Displacements zone 1

In the northern part of the measurement area around viewpoint CT03, zone 1 is located (see Fig. 51c). Fig. 52 shows the zone in detail. It is a nearly horizontal area directly below the main street which broke down after the first measurement period in April (see Fig. 27e and 28a).

During the five months between period 1 and 2 subsidences of about 12cm occurred in the whole horizontal plane. Between the second and third period 4cm subsidences are perceptible. A horizontal displacement is discernible up to a half a metre in Fig. 52a and 52b between April and September. Nearly the same results are shown for the comparison of the September and December data in Fig. 52d and 52e.

Unfortunately, a direct comparison of this TLS data with the GPS data of viewpoint CT03 is not possible. This point got lost between every measurement period. But a comparison between the adjacent GPS points (see Fig. 48 and 49) confirmed a potential subsidence around 15cm to 20cm. In reality the horizontal displacement happened with small values. The result in the TLS solutions is not applicable. A subsidence of a nearly horizontal plane has a negative impact for horizontal movements by a comparison without identical points.

## Zone 2:

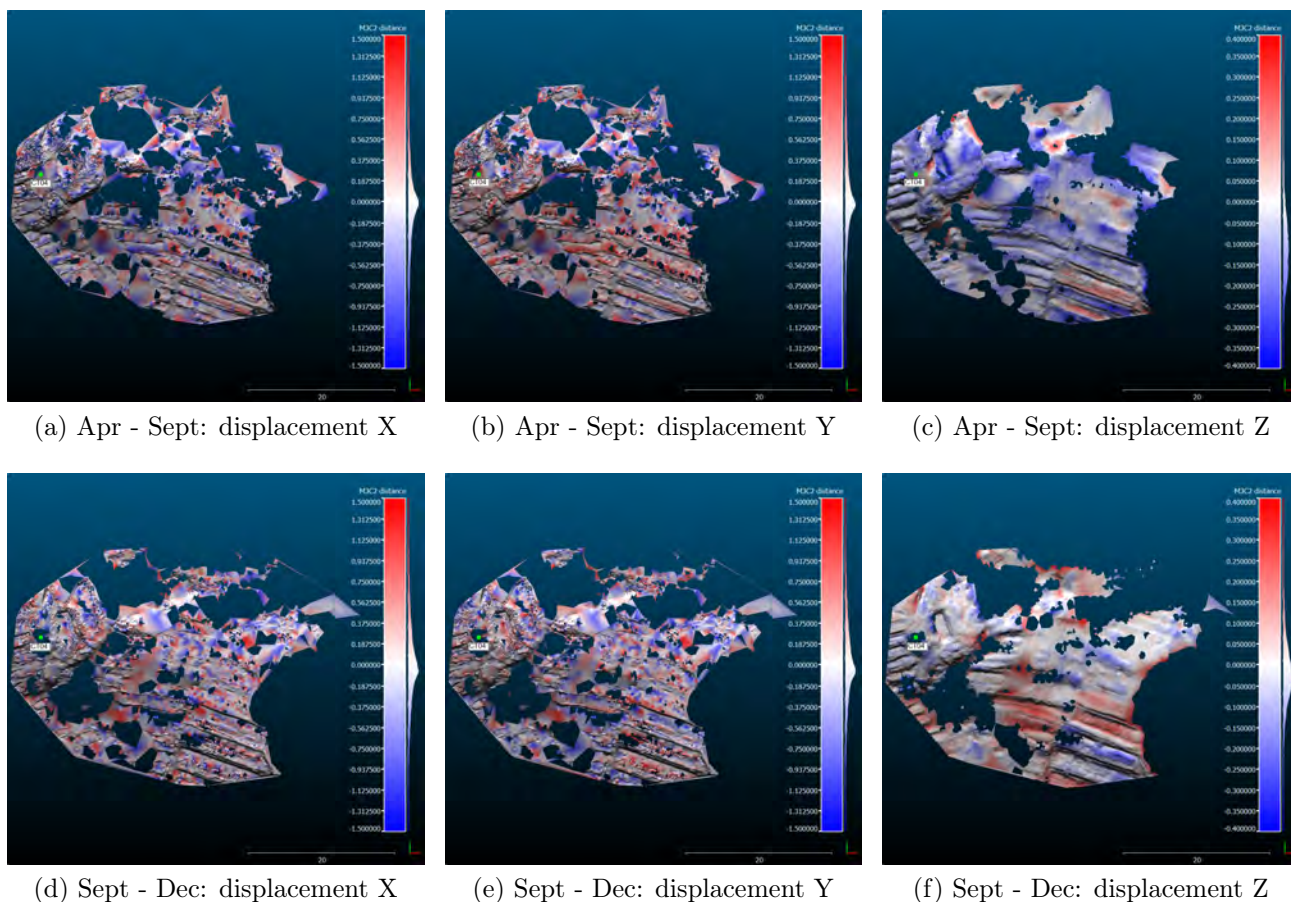


Figure 53: Displacements zone 2

At observation point CT04 and west of it there is a small crest with a slight sloping of the terrain to the north and south. This zone is depicted in Fig. 53 and Fig. 39 shows the vegetation in the south-west area of CT04. Considering the vertical shifts in Fig. 53c and 53f it is discernible that the whole zone has subsided, what particularly occurs between period 1 and 2 at a rate of around 12cm. During period 2 and 3 there are subsidences of around 5cm perceptible. In the south part of this zone slight uplifts are ascertainable between the September and December period.

In comparison with the horizontal movements it is evident that the colourisation indicates a south-west movement of the zone. Between September and December there are bigger displacements discernible than between April and September. Considering the area at the viewpoint CT04 a horizontal shift in north-east direction happened.

The subsidence of about 10 – 15cm between April and September and around 5cm between September and December, which is ascertainable in Fig. 53c and 53f, corresponds with the results of GPS (see Fig. 48). The GPS results show a horizontal displacement of CT04 but in the contrary direction of the TLS results. Similar to zone 1 the vertical movements have a negative effect to the displayed horizontal displacements. In the case of observation point CT04 the subsidence is stronger than the movement to the south-west direction (GPS solution) with the effect that the horizontal movement signals a strong displacement by means of the TLS result. The direction of this horizontal displacement depends on the slope of the terrain and the vertical displacement.

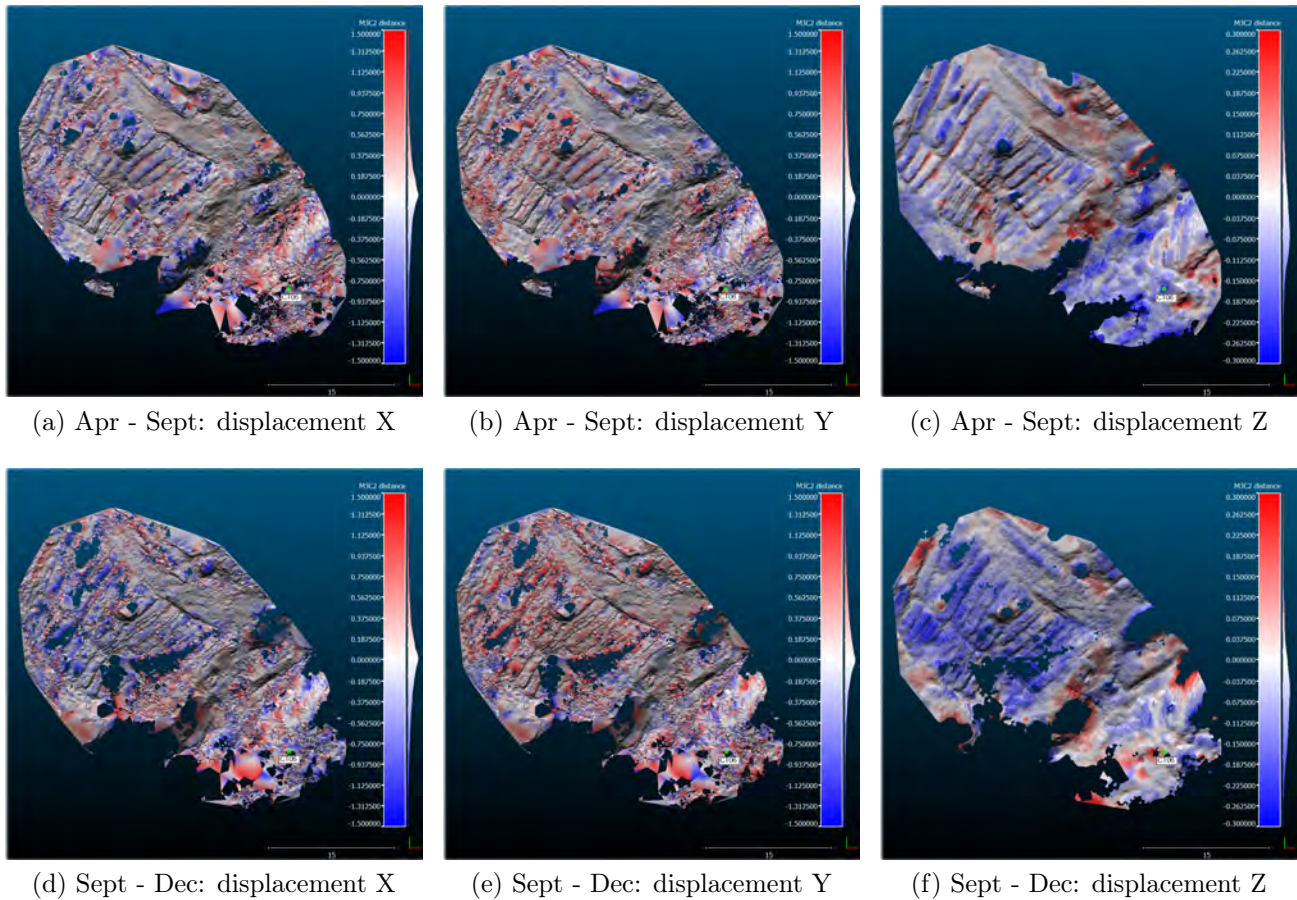
**Zone 3:**

Figure 54: Displacements zone 3

In the middle part between the viewpoints CT05 and CT06, zone 3 (see Fig. 54) is located. The wavy surface in the northern part of the zone corresponds to areas under cultivation, hence, the surface changed significantly between the periods (compare with Fig. 39).

Fig. 54c and 54f show the vertical displacements in the TLS results. In the southern part in this zone around viewpoint CT06, stronger subsidences are discernible during April and September. Conversely, the northern segment shows stronger subsidences between September and December. The southern part is a small horizontal plane without agriculture. In contrast, in the northern area the terrain rises slightly and is agriculturally used.

The displacements in the horizontal plane (TLS results) show no significant movements. In the northern part, movements are displayed in north-west direction. In the horizontal plane of the southern part a change of the displacement in south-east direction is discernible.

In this zone of the measurement area the clayey soil is included in the soil construction which reaches up to the southern part of the whole sliding area. The amount of water in the soil is high in the wet season and the clay swells up (produces uplift). In the dry time, the amount of water is lower and clay thus loses water (produces subsidence). The dry season, accompanied by agriculture, starts in March/April. Between April and September the southern part in this zone subsides due to the lower water content of the soil. In the northern segment water is needed for farming (reduces the subsidence by external supply of water). The southern area loses the water before September, in contrast the northern part loses the water after the farming season (September). The rainy period normally starts in October. This can be a reason why the behaviour of the subsidence, which is discernible in the TLS solution in zone 3, is different between the periods in the northern and southern part.



The GPS result of CT06 in Fig. 48 shows a strong uplift between April and September. The comparison with the TLS solution confirms the assumption about the outlier of the vertical displacement in the GPS result. The TLS solution in Fig. 54f exhibits subsidence of the southern part of around 15cm. A strong horizontal displacement like in the GPS results are not discernible. The terrain in the northern area is slightly sloped to the south. The measured vertical displacements in the TLS solution have a negative impact on the displayed horizontal direction similar to zone 2. In comparison to the plane movement of the GPS points CT05 and CT06 the discernible displacement directions in the TLS results point into a different direction.

#### Zone 4:

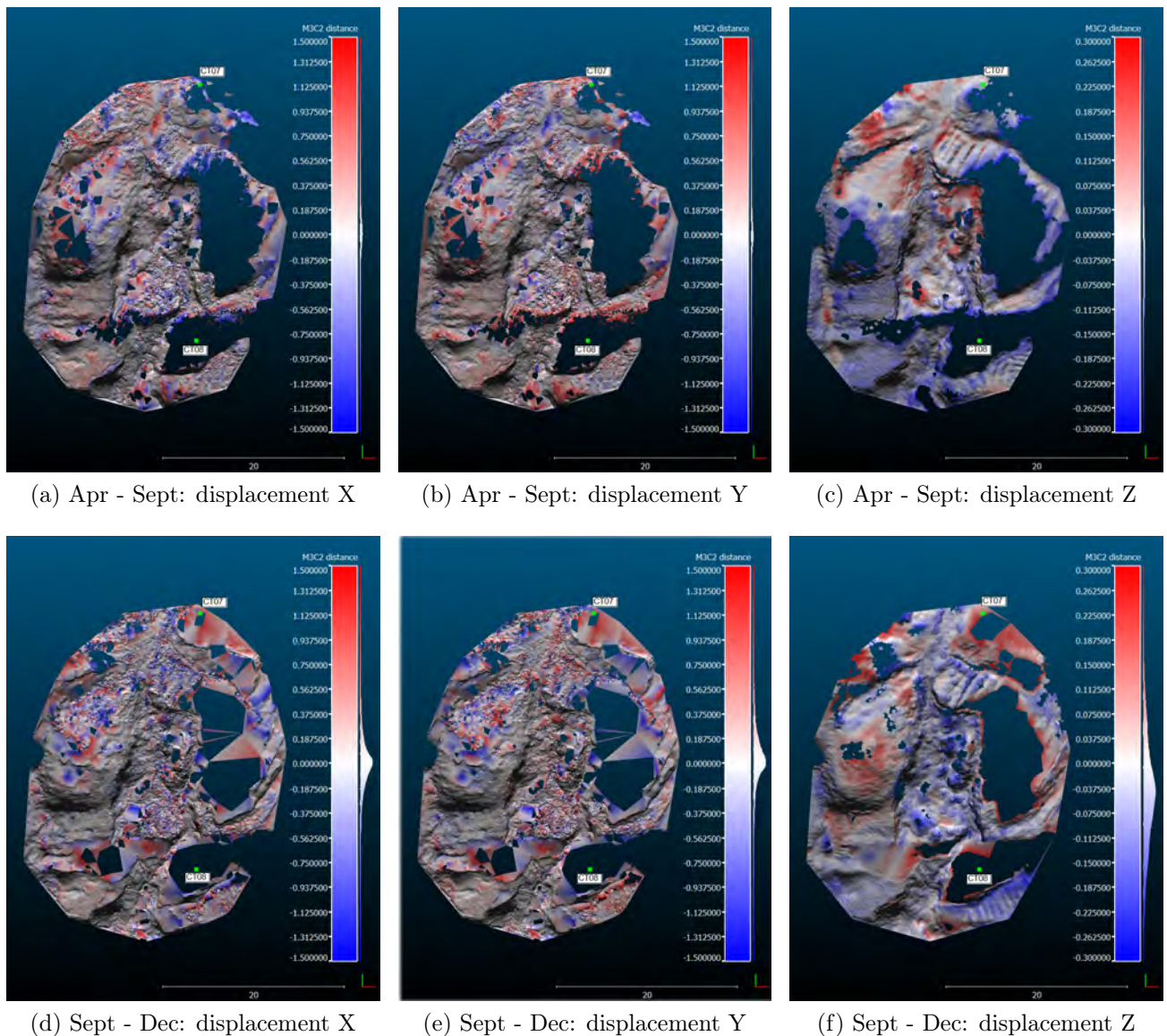


Figure 55: Displacements zone 4

Zone number 4 is located along a surface crack of the terrain between the viewpoints CT07 and CT08. Looking at viewpoint CT07, a soft subsidence of around 10cm is discernible in the TLS results (see Fig. 55c). During September and December there is uplift of about 15–20cm (see Fig. 55f). It is not possible to make a statement about CT08 since no TLS data is available at this viewpoint. CT08 is located on a small hill but no adjacent measurement point could measure the position of this point by TLS.

The comparison of horizontal movements in the zone shows no characteristic displacements. The small lusciously coloured spots in Fig. 55a and 55b also 55d and 55e out of the crack indicate displacements of around  $\pm 1\text{m}$  which is not possible. The horizontal movements in the TLS results can not be interpreted as well as the other zones.

The subsidence, which occurs in the western and southern area (see Fig. 55c), may happen by decreasing pore water pressure in the dry period. The situation is converse in the wet period (see Fig. 55f). Data comparison shows that the crack in the middle of this graph corresponds to subsidence.

As compared to the GPS results, the vertical displacement of viewpoint CT07 is similar in the GPS and the TLS results but only between April and September. For September to December it looks as if this point lifts up, however, this does not coincide with the result of GPS (see Fig. 48). The solutions of GPS show considerable horizontal displacements at viewpoints CT07 and CT08 in south direction. Compared to the TLS results in zone 4 a large displacement is noticeable at viewpoint CT07 between April and September. In the period September to December a horizontal displacement to the north can be deduced, but pointing to the opposite direction as from the GPS solution. For a comparison of CT08 no TLS data is available.

### Zone 5:

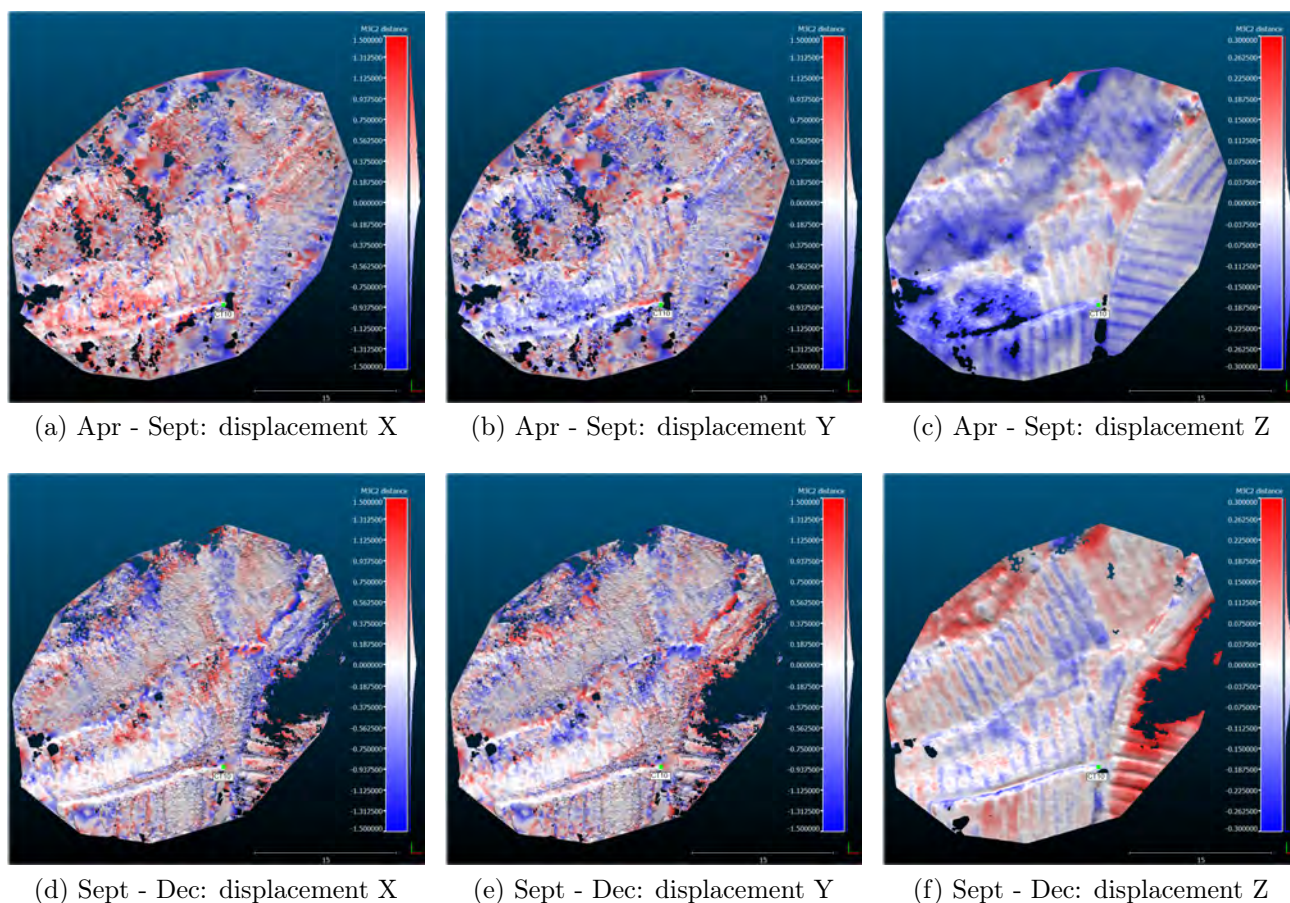


Figure 56: Displacements zone 5

The lowest zone in the south of this measurement area is zone number 5 (see Fig. 56). This part is a horizontal plane in the middle of the whole sliding area which is used for farming. The displacements in  $Z$  between April and September (see Fig. 56c) show an average subsidence of about 10cm. A comparison between the horizontal displacements reveal a movement in south-east direction. Probably this explains the subsidence in Fig. 56c. The displacements

in vertical direction between September and December look different compared with the first two measurement periods. Especially the south-east part of this zone signals strong uplifts. The horizontal movements in the second comparison are small compared to period 1 and 2. The small luscious coloured spots in the horizontal displacements (see Fig. 55d and 55e) could signalise changes of the surface due to farming or erosion. The red coloured part located in the south-east of the zone between September and December in Fig. 56f (uplifts) can be caused by an increase of the pore water pressure. The more likely explanation is another kind of agricultural use which happened in the other parts of this zone. The south-east part is more irrigated during the dry season than the surrounding areas between the measurement periods. This can be a reason for higher pore water pressure which produced uplifts between the second and third period.

The TLS results show a slight horizontal movement of viewpoint CT10 in south-east direction between September and December. Subsidence of CT10 is displayed in Fig. 56f. Both results coincide with the GPS results of the second to third period. A comparison of the GPS data between April and September is not possible because the position of the viewpoint CT10 got lost after the first measurement period in April.

#### 4.2.1 Accuracy of the results

In terms of the accuracy assessment during data processing, the analysis of the TLS results must be treated with caution (see section 3.3.3). Specifically movements in the sliding area around 70mm 3D point position error (36mm in direction  $X$ , 21mm in direction  $Y$  and 55mm in direction  $Z$ ) can be wrongly interpreted although the significance test of the observation points confirms significant movements (see section 4.1). Normally, statistical significance tests are made by the measurements, but the necessary information, especially the accuracy of the single measurements in the point clouds, got lost. The calculation of the significance test is described in section 2.6.3. To reduce mistakes like these and to increase the accuracy of the measurements some future improvements are given in section 5.2.

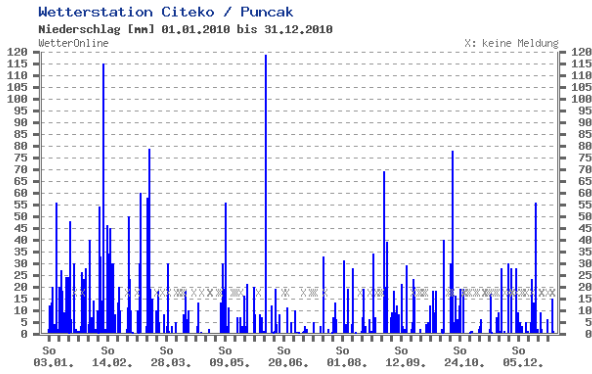
#### 4.2.2 Meteorological effects

The summary of the dissertation of Sadarviana [2006] stated that different movement behaviours between dry and wet seasons occur. These different behaviours are discernible in the TLS results in this research.

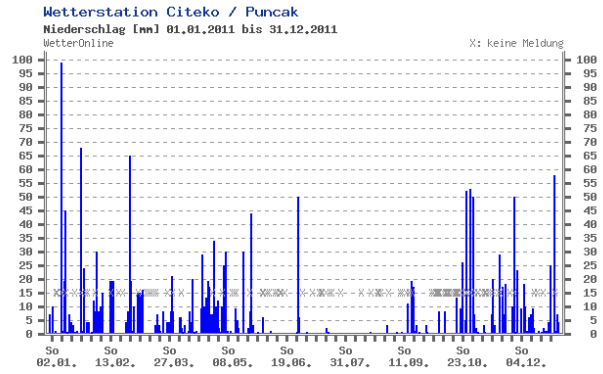
The dry time starts normally at March and lasts up to September and the rainy period runs from September to March. Rainy and dry season may not be taken too literally. In the rainy time more heavy rains occur. In the dry season the arid days predominate. Occasional rains happen also in the dry season and arid days are possible in the rainy season as well. The distribution of precipitation amounts near the measurement area in Ciloto, over recent years (2010 to 2014), is shown in Fig. 57 and 58.

It is clear that the rainfall behaviour is different every year. Years 2010, 2013 and 2014 (see Fig. 58) had fewer dry days than the years 2011 and 2012 (Fig. 57b and 57a).

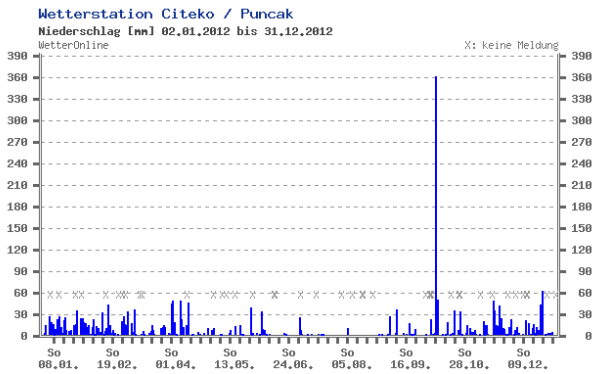
Conversations with local people during the measurements confirmed the results of the dissertation of Sadarviana [2006] and the solutions of this research. Strong movements happen at the beginning of the dry period while less displacements are registered at the beginning of the rainy period.



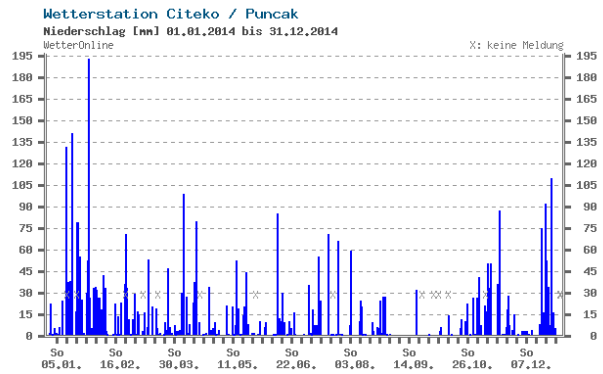
(a) Precipitation 2010



(b) Precipitation 2011



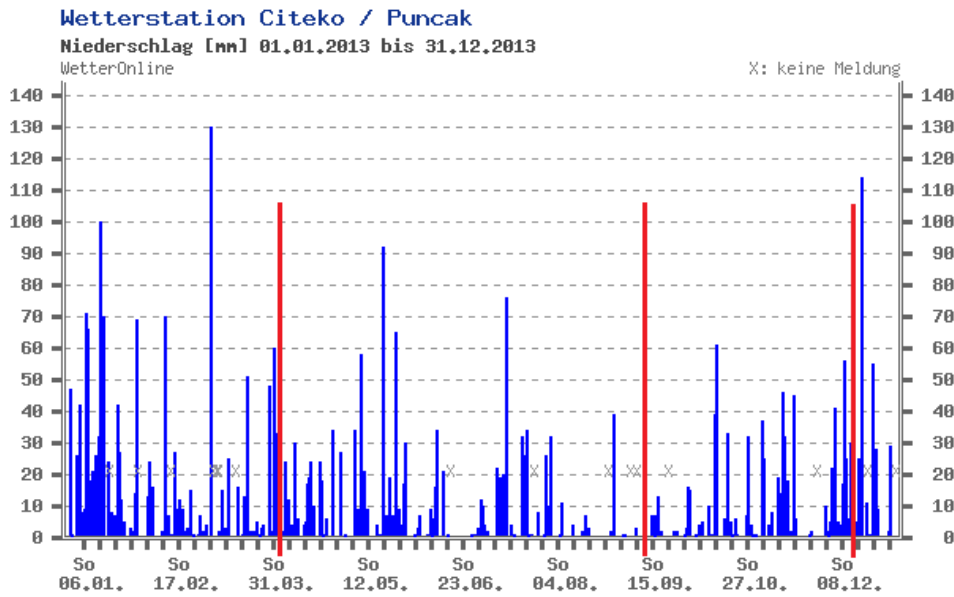
(a) Precipitation 2012



(b) Precipitation 2014

(© Wetter Online - www.wetteronline.de)

Figure 57: Precipitation in the years 2010 to 2014  
[Wetter Online, 2015, retrieved: Jan 2015]



(© Wetter Online - www.wetteronline.de)

Figure 58: Precipitation in the measurement area  
[Wetter Online, 2015, retrieved: Dec 2014]

The red lines in Fig. 58 mark the times of the three measurement periods for this research.

### 4.2.3 Geophysical effects

As can be seen in Fig. 10 the middle and southern part of the whole sliding area contain clay as a component of the soil. As already mentioned before, clay swells up in conjunction with water and produces uplift. Wet clay attenuates strong subsidences by swelling up. In areas close to the measurement points there are no flowing or standing waters which can influence the subsidences or uplifts by pore water pressure or groundwater directly. The main reason for the changing pore water pressure on the surface is water of the rain and water of farming in the measurement area for this research.

Groundwater influences the pore water pressure, too. Their effects on the sliding area are described in Sugalang [1989], Sadarviana [2006], Sadarviana et al. [2009] and Sadarviana et al. [2010] in detail.

## 5 Discussion and summary

### 5.1 Discussion

The landslide in Ciloto is categorised as a 'very slow' movement [Sadarviana, 2006, p. 72]. The slope of the terrain is relatively flat (inclination about  $5^\circ - 15^\circ$ ). The measurements are made in north to south direction starting at the road and extending through agricultural area and sometimes strongly vegetated regions.

The performed measurements passed off without any big problems. The post processing revealed some problems. In retrospect room for improvements both for the planning as well as for the execution of the measurements has to be noted. In section 5.2 some hints are given.

The insight of the dissertation of Dr. Ir. Vera Sadarviana [Sadarviana, 2006] about a complex movement behaviour confirms the results of this work. The GPS observations in this research correspond closely with the described displacement behaviour of the elaborations from 2002 to 2005. In the northern area of the whole movement vertical displacements predominate, in the middle part (conforming to the southern measurement points of this research) the horizontal shifts become greater and the vertical movements become smaller (see section 2.3).

The elaborations and analyses of the TLS measurements proved to be very difficult. Dense vegetation and agricultural cultivation influenced the depiction of the surface between the measurement periods. The manual filtering of the vegetation and non-surface applied objects (houses, plants,...) was difficult and required a lot of time. An automatic filtering was excluded a priori because the complex point clouds include too much necessary information which would be deleted.

The TLS solutions of the point cloud comparison are discussed in section 4.2 in detail. It is noticeable that horizontal movements are difficult to detect because of the nearly flat movement area and a comparison without identical points. Especially horizontal shifts in lightly tilted parts signalise a non-realistic horizontal displacement when a strong vertical movement happens at the same point, too. This phenomenon is visible and is described in different analysis zones in section 4.2 in detail. In contrast to the horizontal movements, uplifts and subsidences are well discernible in the TLS results which also correspond well with the GPS results.

All in all the measurement area is a complex movement area with some minor slips which happen independently and in different types (rotational, translational and compound). Strong vegetation, agriculture and the change of the seasons control the sliding behaviour heavily. An additional event influenced the movement during this research and aggravated the analyses, namely, the road broke down at the top of the sliding area after the first measurement period. Heavy machines and vibrations of the construction works affected the sliding area and this behaviour. This effect is obvious in the results of the vertical displacements of the first and second measurement period (see Fig. 48).

An analysis of the accuracy of the measurements and post processing tasks show that an interpretation of the point clouds is difficult. The overall accuracy derived in section 3.3.3 is based on a theoretical analysis based on the measurement accuracies which are given by the manufacturer. A significance test of the TLS results is not possible because the necessary information about the points in the point clouds got lost. The 3D point position error up to 70mm (35.8mm in direction  $X$ , 21.1mm in direction  $Y$  and 54.7mm in direction  $Z$ ) should

be treated with caution although the displacements of the observation points are significant (see Tab. 16). Potential improvements due to additional measurements can be anticipated.

## 5.2 Future improvements

The overall accuracy of the elaboration process is not optimal. This depends on many factors which are explained in the following subsections. A well defined measurement concept helps to improve the quality of the measurements.

### 5.2.1 GPS-measurements

For this research one GPS device served as the reference station (BASE) during every measurement period. The position of this station was chosen very close to the measurement area on the top of the sliding plane (see Fig. 26). In the end of the measurement campaign the reference station was too close to the measurement area because there was also a displacement for the reference station detected.

The measurement points were positioned nearly in one line from north to south. The stabilisation and the accuracy of the calculated points are good in north-south direction but not in east-west direction. It should be taken into consideration that the measurement points are distributed in both directions.

### Reference station

The reference station (BASE) has to be positioned in a stable area close to the measurement area. To circumvent the problem of a moving reference station it is advised to use more than one reference point (e.g. three reference stations in a triangle which surround the measurement area) and every reference station observes their positions during the whole measurement time. The advantages of more reference stations are:

- Better accuracies of the whole determined point cloud.
- Better coordinate stability of the viewpoints after the data post-processing.
- Control option of the other reference stations.

The longer the observation period of the reference stations, the more precise are the estimated coordinates of the stabilised points and furthermore the viewpoints. The coordinates of the reference stations are calculated with the help of IGS stations, while the coordinates of the viewpoints are estimated with respect to the reference stations (as in this research).

### Measurement points

During the observation process of the reference stations it is necessary to observe the viewpoints in the sliding area. To obtain a good accuracy in georeferencing (e.g. between GPS and TLS observations) it is recommended to measure every observation point in the measurement area by GPS and to do a direct georeferencing for the TLS measurements (see section 2.4.2 - Georeferencing).

### 5.2.2 TLS-measurements

To get a total point cloud from the measurement area, for e.g. ten measurement points, it is necessary to link the single scans to each other. There are different ways to get the full point cloud (see section 2.4.2 - Georeferencing). To relate 2 scans to each other, at minimum three target marks are necessary. If it is required to stop the measurements during the period

(because of approaching darkness or changing weather conditions) it has to be ensured that a restart of the measurements is possible.

For the nexus of the point clouds it should be ensured that measured points of the single scans do not lose their relation to the observation points and their accuracies. This is essential for the statistical significance test and the analysis of the accuracy (see section 3.3.3).

To compare point clouds from different periods to each other it is necessary to transform all point clouds into the same coordinate system. For this it is essential to take some measurement points out from a fixed point (e.g. by GPS or total station). To increase the accuracy it is recommended to settle the measurements by forced centring (all measurements of the same viewpoint use the same tripod and three batch as originally used).

A key advantage of TLS measurements is that this technology can measure surfaces of objects by a high density. A disadvantage is that no discrete points like GPS can be measured. For specific movement analysis it is recommended to choose sufficient identical points in the sliding area which can be measured by the TLS device. These kind of points can be artificially created targets (e.g. reflection marks on stabilised objects like walls, houses, trees,...) or naturally available targets like edges of houses or distinctive formed and stable stones. For a good analysis of these points it has to be ensured that the identical targets are fixed during the whole measurement campaign.

### 5.3 Summary

The focus area in this research was located on the border between a rotational (west-side) and translational (east-side) slide of the whole movement. Varying movement patterns between the different sliding types are not ascertainable in the kind of elaboration which was done in this research. Crack formations could not be derived out of the solutions. Therefore the TLS results visualise uplifts and subsidences well because the movement area is a relatively flat zone. This is also a reason why horizontal displacements are difficult to detect. Often strong horizontal shifts are displayed by an actually less vertical movement. In comparison to the observation points from GPS, the TLS solutions sometimes show contrary horizontal movements. To provide a reasonable movement analysis about TLS results it is recommended that different identical points in the movement area are used.

The analysis of the measurement accuracy based on manufacturer information and the data processing provide indifferent results. This is a reason why it is difficult to detect movements in the scan solutions. Although the statistical significance test of the discrete measurement points registered significant movements, the discernible displacements in the point clouds must be treated with caution. Ways to improve the accuracy of the measurement result are given in this work. Primarily, improvement suggestions for the practical elaboration are listed.

Three measurement periods were investigated for this research. To create a kinematic model, three periods are not sufficient. The compiled static model confirmed previously conducted measurement campaigns. In this research large vertical movements and small horizontal shifts in the sliding area were detected. These phenomena occurred also in older researches. In the middle part of the whole sliding area, which conforms the southern part of this research, the horizontal shifts increase and the vertical displacements decrease. The direction of the horizontal movement varies between east and south-west. The complex moving behaviour of the sliding area is shown in this research, too.



Shortly after the first measurement period a heavy rainfall triggered a slip on the top of the movement area and the main road broke down. Construction works started and heavy machines influenced the moving behaviour of the slip by vibrations. This is discernible by high values of the settlements of the northern measurement points, especially between the first and the second measurement period.

The search for an existing appropriate example for a mass movement like that one in Ciloto would exceed the frame of this thesis and might be part of further researches.

## References

- Abramson, Lee W.; Thomas S. Lee; Sunil Sharma; and Glenn M. Boyce (1996): *Slope Stability and Stabilization Methods*. A Wiley-Interscience Publication - John Wiley & Sons, Inc.
- AIUB, Astronomical Institute of the University of Bern (2013): <http://www.bernese.unibe.ch/>.
- Bayerisches Landesamt für Umwelt (2013): [www.lfu.bayern.de/geologie/index.htm](http://www.lfu.bayern.de/geologie/index.htm).
- BeiDou (2013): [en.beidou.gov.cn/](http://en.beidou.gov.cn/).
- Dach, Rolf; Urs Hugentobler; Pierre Fridez; and Michael Meindl (2007): Bernese GPS Software - Version 5.0. AIUB, Astronomical Institute of the University of Bern.
- Eling, Dirk (2009): *Terrestrisches Laserscanning für die Bauwerksüberwachung*. Ph.D. thesis, Gottfried Wilhelm Leibnitz Universität Hannover.
- European GNSS-Agency (2013): [www.gsa.europa.eu](http://www.gsa.europa.eu). European GNSS Agency.
- Federal Space-Agency (2013): [www.glonass-iac.ru/en/](http://www.glonass-iac.ru/en/).
- Freie Universität Berlin (2013): [www.cms.fu-berlin.de/geo/fb/e-learning/pg-net/themenbereiche/geomorphologie/massenbewegungen/](http://www.cms.fu-berlin.de/geo/fb/e-learning/pg-net/themenbereiche/geomorphologie/massenbewegungen/).
- GeoDZ (2013): [www.geodz.com/](http://www.geodz.com/).
- Girardeau-Montaut, Daniel (August 2012): CloudCompare Version 2.1.
- Google Inc. (2013): [www.maps.google.at](http://www.maps.google.at).
- Gruber, Franz Josef and Rainer Joeckel (2011): *Formelsammlung für das Vermessungswesen*. VIEWEG+TEUBNER.
- Heunecke; Kuhlmann; Welsch; Eichhorn; and Neuner (2013): *Handbuch Ingenieurgeodäsie - Auswertung geodätischer Überwachungsmessungen*. Wichmann.
- Joeckel, Rainer; Manfred Stober; and Wolfgang Huep (2008): *Elektronische Entfernung- und Richtungsmessung und ihre Integration in aktuelle Positionierungsverfahren*. Herbert Wichmann Verlag.
- Kahmen, Heribert (2006): *Vermessungskunde - Angewandte Geodäsie*. Walter de Gruyter.
- Kaplan, Elliott D. and Christopher J. Hegarty (2006): *Understanding GPS - Principles and Applications*. Artech House.
- Kraus, Karl (2004): *Photogrammetrie - Band 1*. Walter de Gruyter.
- Kuntsche, Konrad (2000): *Geotechnik: Erkunden - Untersuchen - Berechnen - Messen*. Vieweg.
- Leica ScanStation C10 (2011): [www.leica-geosystems.com/en/Leica-ScanStation-C10\\_-79411.htm](http://www.leica-geosystems.com/en/Leica-ScanStation-C10_-79411.htm).
- Li, Lihua (2012): *Separability of deformations and measurements noises of GPS time series with modified Kalman filter for landslide monitoring in real-time*. Master's thesis, Universität Bonn.

- Niemeier, Wolfgang (2008): *Statistische Auswertemethoden - Ausgleichungsrechnung*, vol. 2. Auflage. Walter de Gruyter.
- PAUX Technologies GmbH (2013): [www.paux.com/uri/topic/22716472/klassifikation-der-massenbewegungen](http://www.paux.com/uri/topic/22716472/klassifikation-der-massenbewegungen).
- Rapp, Martin (2011): *Monitoring von Massenbewegungen*. Master's thesis, Technische Universität Wien.
- Sadarviana, Vera (2006): *PEMANFAATAN METODE GEODETIK UNTUK MENGESTIMASI KARAKTERISTIK, TIPE DAN BIDANG GELINCIR PADA ZONA LONGSOR*. Ph.D. thesis, Institut Teknologi Bandung.
- Sadarviana, Vera; Hasanuddin Z. Abidin; Djoko Santoso; and Joenil Kahar (2009): Characteristic, Type and Slip Surface Estimation at Landslide Zone by Geodetic Method.
- Sadarviana, Vera; Hasanuddin Z. Abidin; Djoko Santoso; and Joenil Kahar (2010): Ground Water Level Influence to Slope Displacement at Landslide Zone by Geodetic Method.
- Shan, Jie and Charles K. Toth (2009): *Topographic Laser Ranging and Scanning - Principles and Processing*. CRC Press, Taylor & Francis Group.
- Sistemilaser (2013): <http://www.glonass.it/eng/>.
- Sugalang (1989): *Landslide in Ciloto Area West Java Indonesia*. Master's thesis, Tekniska Högskolan I Luleå - Luleå University of Technology.
- Topcon GR-3 (05 2007): [www.geodisgroup.at/geo-de/gr-3-dreifach-empfaenger](http://www.geodisgroup.at/geo-de/gr-3-dreifach-empfaenger).
- Torge, Wolfgang (2003): *Geodäsie*. Walter de Gruyter.
- Universität Freiburg (2013): [www.uni-freiburg.de](http://www.uni-freiburg.de).
- U.S.-Government (2013): [www.gps.gov](http://www.gps.gov).
- Wetter Online (2015): [www.wetteronline.de](http://www.wetteronline.de).
- Wieser, Andreas (2014): Überwachung von Massenbewegungen im alpinen Raum & Resampling terrestrischer Radarscanneraufnahmen von verschiedenen Standpunkten im Rahmen eines Böschungsmonitoring. In: *Ingenieurvermessung 14 - Beiträge zum 17. Internationalen Ingenieurvermessungskurs Zürich*.
- Wissenswertes (2013): [www.wissenswertes.at/](http://www.wissenswertes.at/).
- Witte, Berthold and Peter Sparla (2011): *Vermessungskunde und Grundlagen der Statistik für das Bauwesen*. Herbert Wichmann Verlag.